applied physics

The physics of nanosurface systems

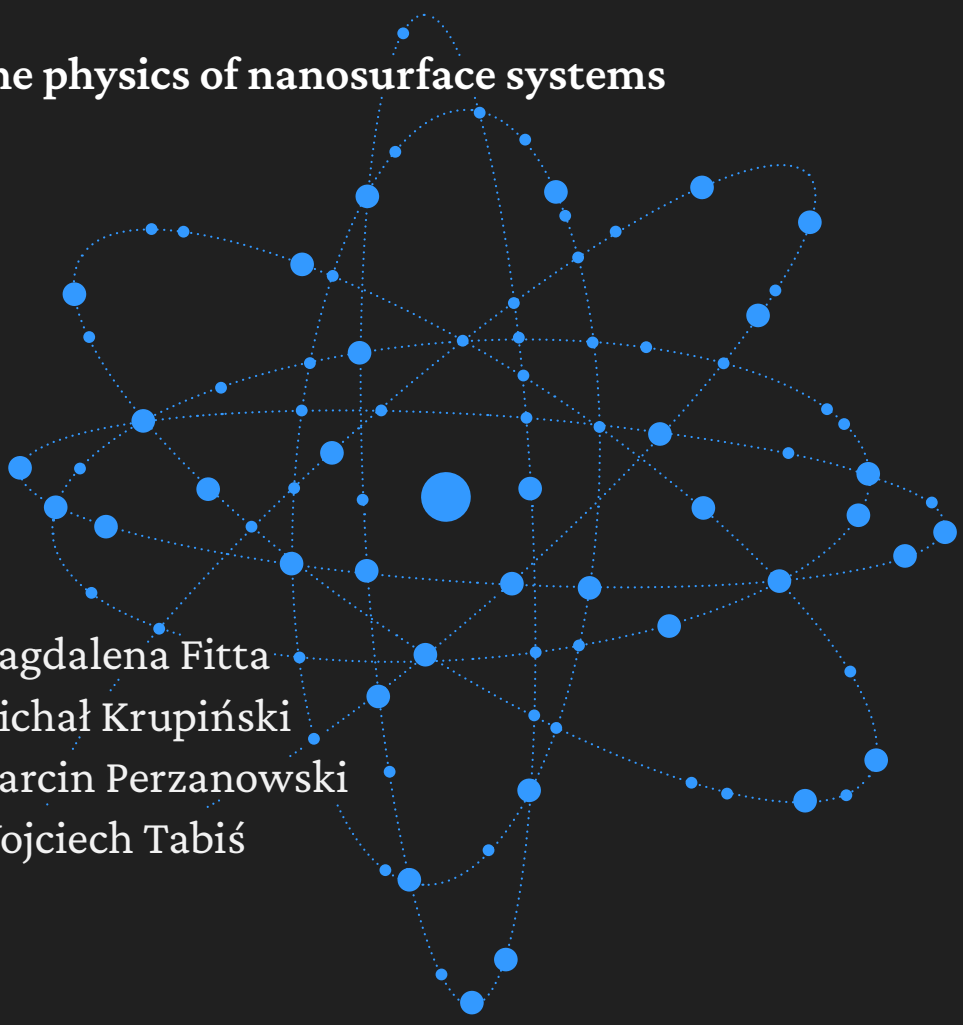

Magdalena Fitta
Michał Krupiński
Marcin Perzanowski
Wojciech Tabiś

Kraków 2023

Cracow University of Technology

applied physics

The physics of nanosurface systems

Magdalena Fitta
Michał Krupiński
Marcin Perzanowski
Wojciech Tabiś

Kraków 2023

This text was published as a part of the project 'Excellence programming – PK XXI 2.0
Cracow University of Technology development program for the years 2018–22'.
Funding from EU: 18,048,774.96 PLN

eISBN 978-83-67188-44-9
Online edition

4,5 publisher's sheets

Wydawnictwo PK, ul. Skarżyńskiego 1, 31-866 Kraków; 12 628 37 25, fax 12 628 37 60
wydawnictwo@pk.edu.pl
www.wydawnictwo.pk.edu.pl
Correspondence address: ul. Warszawska 24, 31-155 Kraków

CONTENTS

PREFACE

This book covers the important and timely topics of nanosurfaces. It is addressed mainly to undergraduate students studying the problems of nanoscience as part of a physics or engineering degree. Our aim was to combine a wide range of topics related to fabricating and characterising the samples that display astonishing properties originating from the surface and nano-size effects.

Nanophysics includes physical laws applicable from the 100-nm scale to the subatomic scale, down to approximately 0.1 nm. Many of the physical properties of very small objects (~1 nm) are very different from macroscopic objects. Thus, the engineering and study of the physical properties of such materials require dedicated techniques and equipment. The criterion of choice of the topics presented in this book is based on the multidisciplinary expertise of the authors, who are pursuing research on surface physics and nanoscience.

We hope that the reader can find stimulating, even profitable, new ideas in this (rather slim) book. For details, the curious reader can follow the most recent references that are provided in the text.

1. INTRODUCTION

1.1. THE WORLD OF NANOTECHNOLOGY

'What I want to talk about is the problem of manipulating and controlling things on a small scale.' With these words, Richard Feynman welcomed the participants of the American Physical Society meeting on 29th December 1956. At that time no-one expected this lecture to become the first to deal with the issues of nanotechnology—the field of science at the time was completely unimaginable. Today, Feynman is considered to be the creator of nanoscience and nanotechnology, being the first person to indicate that manipulation on the molecular scale is possible and should be a goal of future science and technology [1].

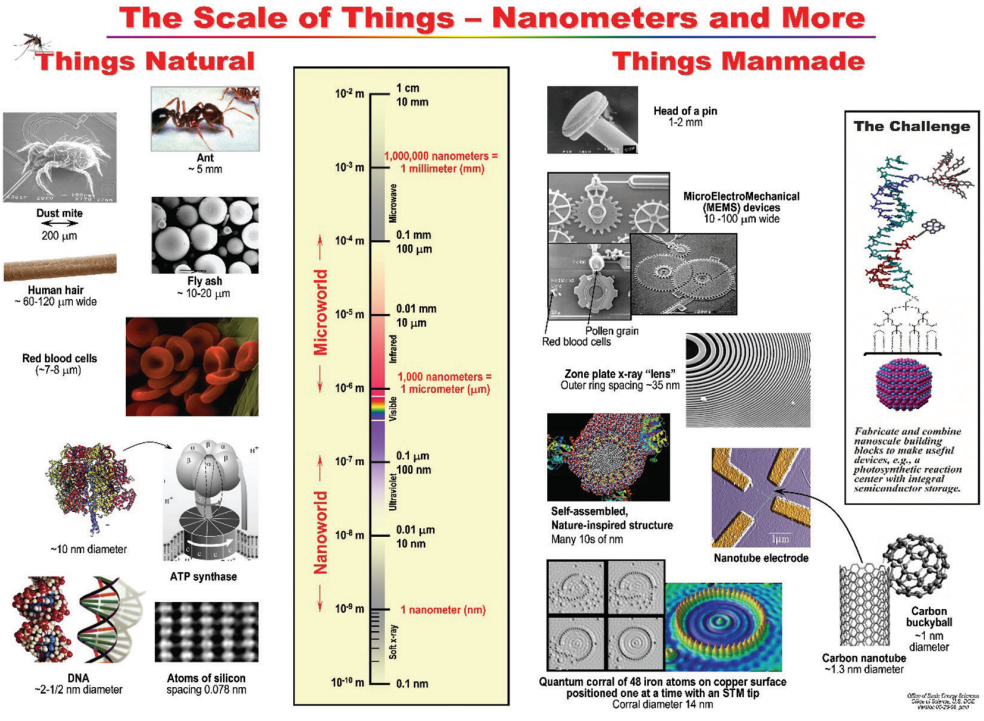

Figure 1-1. A comparative perspective of microscale and nanoscale objects (from the US Department of Energy, [47]

Low-dimensional systems reveal new and often unexpected properties. There is also a certain sensation here: the results of experiments very often cannot be fully understand by scientists, due to lack of specific knowledge on the nanoscale phenomena. Although, it is very difficult to predict the future, the work being carried out in the field of nanoscience are expected to make a breakthrough in information gathering, data recording, and other applications in spintronics [2].

Nanotechnology can be defined as the manipulation of matter on an atomic, molecular, or supramolecular scale. The nanostructures are objects between 1 nanometre and 100 nanometres in size. To better understand how small that is, we can consider Figure 1-1, titled 'The Scale of Things', which provides a comparison of objects of various sizes. The chart starts with objects that can be seen by the unaided eye, such as a human hair. On the opposite side of the scale, we can find an object a few nanometres in size: an ATP molecule or a carbon nanotube. This image also shows that manipulating a nano-sized object is a great challenge for modern science and technology, because advanced and powerful measurement techniques need to be used for the study of the physical properties of such small structures.

1.2. NANOSTRUCTURES

There are two approaches to nanomaterial fabrication: top-down and bottom-up. In the first case, the structure's size can be reduced by physical techniques such as milling or lithography. Bottom-up nanotechnology uses the chemical properties of single atoms or molecules and nanostructures are created as a result of self-assembly. A comparison of these two approaches is presented in Figure 1-2.

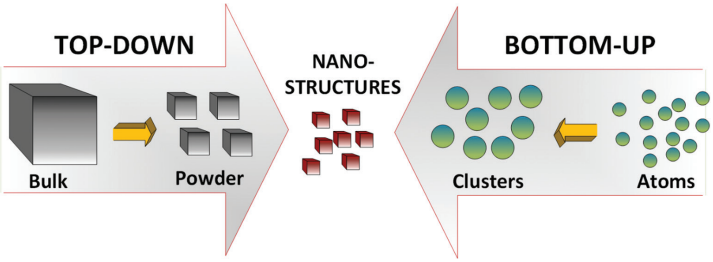

Figure 1-2. Schematic representation of the bottom-up and top-down processes of synthesising nanomaterials (own elaboration)

The properties of low-dimensional materials differ from those of the bulk material mainly because quantum-sized effects come into play. Another reason is the extremely large surface area per unit volume at the nanoscale.

The differences between the bulk material and the nanostructures are seen in the density of the energy states. The density of states (DOS) of a system describes the

number of states that are available in this system. The density of states is represented as a function of g(E), where DOS is equal to g(E)dE—the number of states per unit volume in the energy range (E, E+dE). In a three-dimensional material, the movement of electrons and holes is not spatially confined. The DOS for bulk materials can be expressed as a parabolic function. As the dimensionality of nanostructures decreases, the form of the state density function changes (Figure 1-3).

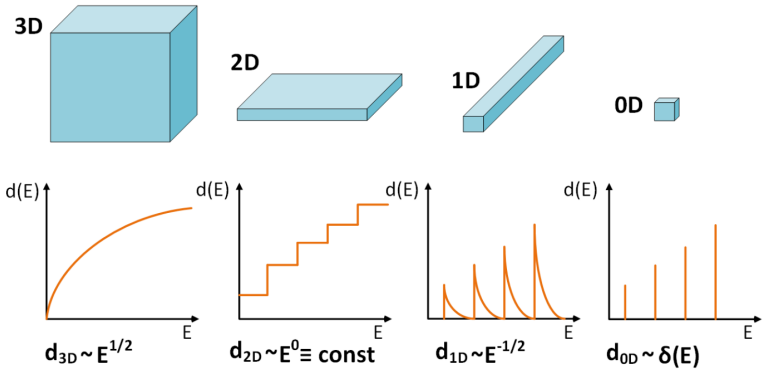

Figure 1-3. Systems with 3, 2, 1, and 0 degrees of freedom for electron propagation and the related electronic density of states (own elaboration)

Nanostructures are usually classified according to the number of reduced dimensions they have. The low-dimensional systems can be assigned into three categories:

- Zero-dimensional (0D), where the parameters of length, height, and width are fixed at a single point, for instance at a dot. Electrons in 0D nanostructures are trapped in a dimensionless space and the distribution of the DOS ceases to be continuous, consisting of a number of energy levels corresponding to the next quantum numbers and increasingly higher energies. Clusters, quantum dots, and nanoparticles are examples of 0D systems.
- One-dimensional (1D), where only one of the size parameters exists and electrons can move along the *x* axis. In 1D materials, such as nanowires, the DOS depends on energy as $E^{-1/2}$.
- Two-dimensional (2D), where the parameters of length and width exist. A real counterpart of this system is a thin film (a few atomic layers thick) evaporated on a solid substrate. Electrons in 2D systems behave as if they were in the 'potential box', with one side much smaller than the other two. This results in the fact that the density of states for each value of a quantum number, which indicates that the allowed motion energies along an axis perpendicular to the film surface is constant.

The derivation of the density of states in 2D, 1D, and 0D models are listed in Appendix 1.

Table 1

Types of nanostructures

	Type of nanostructure	Size
0D	Clusters, quantum dots	1–10 nm (diameter)
	Nanoparticles	1–100 nm (diameter)
1D	Nanowires	1–100 nm (diameter)
2D	Arrays of nanoparticles	Several nm2 to μm2 (area)
	Thin films	1–100 nm (thickness)

2. METHODS OF PREPARATION FOR NANOSURFACE SYSTEMS

2.1. PHYSICAL METHODS

2.1.1. PHYSICAL VAPOUR DEPOSITION

Physical vapour deposition (PVD) is a group of techniques involving the deposition of thin films and coatings from a gas phase using a variety of physical processes to create a vapour of the material to be deposited. These processes need a pressure lower than atmospheric pressure, so the techniques require vacuum chambers and sometimes even ultra-high vacuum systems. A common feature of these approaches is the crystallisation of layers on a substrate, whose temperature is always lower than the temperature of the vapour source. The atoms of the deposited material form a layer by adhesion, bonding with the substrate atoms.

PVD can be used to deposit almost any type of inorganic and even some organic materials onto a diverse group of substrates and surfaces. It can yield layers with thicknesses ranging from single-atom monolayers to several micrometres or even thicker. Regardless of the type of PVD, the process consists of three stages:

1) obtaining a vapour of the deposited material
2) transporting the atoms or the molecules from the source to the substrate
3) condensing the material, resulting in an atom-by-atom growth of the layer

Currently, several varieties and modifications of PVD methods are known. The most important of them are listed below:

- resistance heating evaporation
- electron beam evaporation
- sputtering
- magnetron sputtering
- plasma-assisted PVD
- pulsed laser deposition (PLD)

In the case of resistance heating evaporation, the deposited material is placed in effusion cells, which maintain a sufficiently high temperature for evaporation. To avoid any contamination of the film, the cells should not react chemically or create alloys with the evaporated material. At high temperatures they should also provide negligible vapour pressure. In order to meet these requirements, they are built either

from ceramic crucibles made of aluminium oxide, carbon, quartz, or boron nitride or from metals such as molybdenum, tungsten, or tantalum. The most effective way to heat the ceramic crucibles is with resistive Joule heating. For this purpose, coils made of tungsten, tantalum, or molybdenum are wound around the crucibles and powered with a strong electrical current. In the case of metallic evaporators, they are shaped to form boats, spirals, or baskets and direct heating can be achieved by passing a strong current directly through them.

A more advanced way of heating materials is electron guns, and the deposition technique utilising such equipment is known as electron beam evaporation, or e-beam PVD. It is used for refractory metals and for materials that easily react with the crucibles at high temperatures. An electron beam is produced by the cathode, focussed by a magnetic or electrical field, and directed onto the material to be evaporated. The main advantage of the e-beam PVD is the possibility of precisely focussing the electron beam and directly heating the material inside the crucible, while the crucible is cooled with water. As a result, the interaction of the vaporised material with the crucible is minimised. The disadvantage of this method is the need to use high-power, high-voltage power supplies. Typical parameters of electron guns are an acceleration voltage of 2–20 kV, an electron beam power of 2–10 kW, and an electron beam current of up to 0.5 A.

Sputtering techniques involve knocking the particles out of a cathode, which is covered by a bulk material, called the target. This is a result of bombarding the target with noble gas ions with 0.1–1 keV of energy. The ions are emitted during a glow discharge caused by a direct or high-frequency current between the grounded anode and the cathode. The ionic current density determines the speed of the deposition process, and its value depends on the electrode voltage and the pressure in the chamber. Another type of sputtering (called magnetron sputtering) utilises a specifically shaped magnetic field under the target, which curves and significantly extends the electron path. This increases the ionic current density and increases the speed of the deposition by a factor of 10–1,000.

In the PLD method, the pulsed laser beam hits the surface of the solid or liquid target. Strong absorption of high-energy radiation leads to rapid evaporation (ablation) of the target surface and a rapidly expanding plasma is formed. This plasma can reach a substrate, condense on it, and form a layer. In comparison with the previously described methods, PLD has many advantages. Firstly, it allows almost any solid or liquid material to be deposited. Also, due to the pulsing of the laser, the growth rate and thickness of the layers can be precisely controlled. Moreover, the target evaporates only in the place that is exposed to the laser beam, allowing good control over the evaporation. However, there are also disadvantages. Due to the small size of the vapour source, the thickness of the deposited material varies depending on the location on the substrate. Typically, homogeneity can be maintained only within an area up to 1 cm^2. The evaporated material may also contain particles of different

diameters, reaching up to 1 μm. This leads to massive heterogeneity and can have a substantial effect on the properties of the deposited layers.

Due to the different properties of materials (melting temperatures, vapour pressure, chemical properties, growth type on the substrate, etc.), there is no single optimal method of thin film deposition. For each material, the deposition parameters and approach should be selected individually, taking into account the thickness, roughness, morphology, purity, and crystallite size of the desired final layer. A list of tips and techniques suitable for deposition of the most popular materials is available, for example, on the website of Kurt Lesker:
https://www.lesker.com/newweb/deposition_materials/materialdepositionchart.cfm?pgid = 0

2.1.2. NANOPATTERNING TECHNIQUES

Nanopatterning is a key process in modern science and technology, through which nanostructures can be created in a controlled way. From a fundamental point of view, it enables the study of phenomena which are unobservable in bulk materials and which only appear at the nanoscale. In terms of applications, it delivers modified materials with new and unusual properties. After several decades of advancements in nanotechnology, a wide range of techniques has been developed to create objects at the nanoscale. They show significant differences in performance, price, repeatability, required equipment, and the materials that can be patterned. Despite the substantial differences between them, all techniques can be divided into two groups: bottom-up and top-down approaches. This categorisation is based on the question of whether a given method builds structures from smaller elements (bottom-up) or whether it uses the partition of larger systems into smaller elements (top-down).

In the top-down approach, bulk materials are processed, split, or divided to obtain submicron sizes. It usually provides good control over the resultant structure, but is time-consuming and usually very expensive. Ion and electron lithography may serve as examples. On the other hand, the bottom-up approach includes the manipulation of atoms, molecules, or nanoparticles and the combination of them into larger structures. Such manipulation is possible using devices such as a Scanning Tunnelling Microscope (STM) or by self-assembly, which takes advantage of the natural tendency of some materials to create organised structures. A classic example of self-assembly is alkanotiols arranged on a gold (111) surface or polysiloxanes on silicon and glass. Sometimes it is not possible to classify a nanopatterning technique as one of the above-mentioned approaches, since it combines top-down and bottom-up features. One such example is nanosphere lithography, which is discussed in the following sections.

An exhaustive discussion of all nanopatterning methods is beyond the scope of this handbook. Here, only an outline of three techniques belonging to the

'unconventional methods' of nanopatterning is provided. This group of techniques was developed during the last two decades and is characterised by simplicity, as they usually do not require advanced equipment. These techniques are tailored for specific needs and materials and are not currently commercially available or used in mass production. They are in a niche which is inaccessible to conventional methods (such as optical, ion, and electron lithography), which creates a lot of opportunities for innovation and development.

2.1.3. DIRECT LASER INTERFERENCE PATTERNING

Direct laser interference patterning (DLIP) is a method for surface modification which enables periodic patterns to be directly, permanently, and efficiently obtained on various types of materials, such as metals, semiconductors, ceramics, or polymers. It allows very precise nanometre-sized structures to be produced uniformly and over large areas. Compared with the more common lithography methods, its main advantage comes from directly processing the material without using intermediate masks or photoresists. Additionally, it requires only a single technological procedure and a relatively large area can be patterned in one process.

DLIP systems consist of a high-powered pulsed laser source, an optical system to divide the laser beam, and a sample positioning stage. The pattern is produced by two, three, four, or more beams, which superpose on the sample surface. In some areas, light waves interfere destructively and do not change the material's morphology, whilst elsewhere they sum up to a substantial amplitude and ablate the material. The pattern is created by direct, periodically local heating of the surface through the local photothermal interaction between the light and the metal. Photons are absorbed by electrons, which dissipate the energy into the thermal lattice vibrations. In the case of metals, the process occurs within a layer approximately 10^{-8} m thick, corresponding to the penetration depth of light. The geometry and period of the pattern depend on the wavelength and the angles between the beams.

Due to the short duration of thermal exposure by a pulse laser, the phases and morphology of the deposited films can be modified under precise control. In the case of thin layer patterning, which requires a quick input of energy, the processes of melting and solidifying occur within a very short time. This allows for the creation of a pattern with a well-defined long-range order with periods from the sub-micrometre scale up to micrometres and offers a remarkable potential to tailor mechanical and other properties by functionalising the nanostructure's surface.

The simplest setup for DLIP, which yields strips or nanowires, is shown in Figure 2-1. In such a configuration, two coherent sources—S1 and S2—emit laser beams directed at angle γ to the sample surface. For each point on the irradiated surface, the difference of optical paths (Δ) equals the sum of the lengths of vectors Δ_1 and Δ_2:

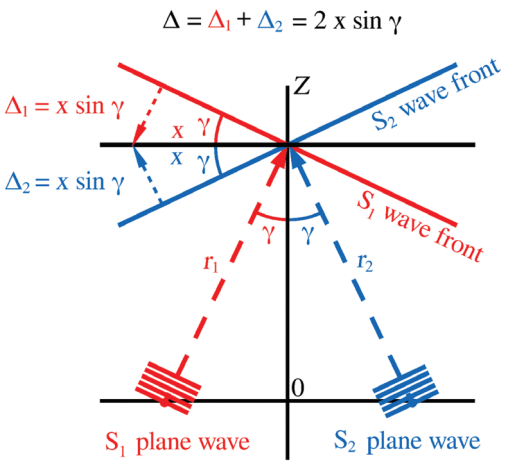

Figure 2-1. A DLIP setup with two plane waves emitted by sources S1 and S2 [34]

The interference condition is given by:

$$2x \sin\gamma = n\lambda, \tag{2-1}$$

where n is the order of interference maximum, and λ is the light wavelength. The period Δx of the interference pattern (the distance between the interference maxima) is then given by:

$$\Delta x = \frac{\lambda}{2\sin\gamma}. \tag{2-2}$$

The above formula shows that the period of interference pattern created on the surface of a sample is limited by the wavelength of the light being used; its lower limit is λ/2 (for γ = 90°). Additional tuning of the pattern's period is possible by changing the angle γ.

More complex patterns can be obtained by using a larger number of laser beams. In each case the period of the resulting pattern is determined by the wavelength of radiation λ. The results of 2-, 3,- and 4-beam interference simulations (for λ = 1064 nm) are shown in Figure 2-2. For 2-beam interference (Figure 2-2a), the pattern consists of parallel periodic long stripes. The period of the stripes can be modified by changing the radiation wavelength and the geometry of the setup. Figure 2-2b and c represent the interference of three beams in symmetric and asymmetric configurations, respectively, in relation to the z axis. It can be observed that the changes from a symmetric position to asymmetric geometry causes the pattern to transform from round to elongated spots. Increasing the number of interfering beams and changing the optical setup geometry results in a great variety of periodic structures. An example of such 4-beam interference is presented in Figure 2-2d–f. Figure 2-2d and e illustrate the interference pattern corresponding to the symmetric configuration of the light

beams. The spots are large if the beams are very close to each other, whilst spreading them apart yields a denser pattern. Figure 2-3f illustrates the interference obtained for a non-symmetric configuration of four beams.

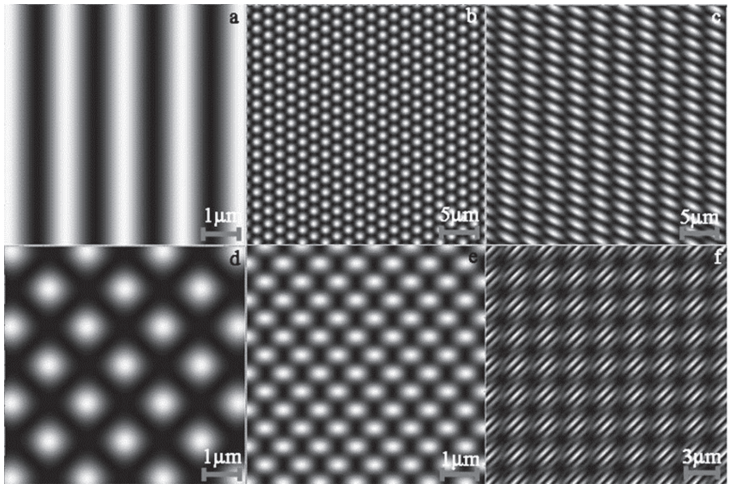

Figure 2-2. Interference patterns calculated for the geometry depicted for (a) λ = 1024 nm and two laser beams S1 = S2 = 2.5 cm; for (b) three laser beams S1 = S2 = 2.5 cm, S3 = 6 cm; (c) S1 = S2 = 2.5 cm, S3 = 6 cm with the sample declined at π/3 with respect to the xy plane; and for (d) four laser beams S1 = S2 = S3 = S4 = 4 cm; (e) S1 = S2 = S3 = S4 = 50 cm; and (f) S1 = S3 = 6 cm, S2 = S4 = 60 cm. In all cases the distance between the sample and the source plane was z = 0.06 m [34]

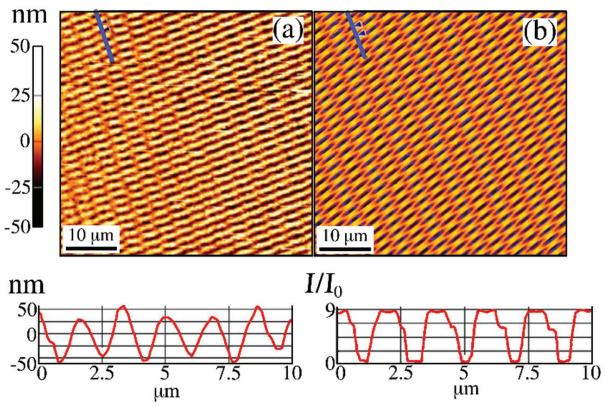

Figure 2-3. AFM image of the interface patterns generated by the laser beam (a) and a numeric simulation calculated with the experiment conditions (b). The height profiles below the images were taken along the blue lines. The periodicity of the resulting nanostructures calculated from the height profile is 1.4 μm [34]

Figure 2-3 shows the results of 3-beam patterning performed for a [Co (1 nm)/Cu (2 nm)]×3 multilayer compared with a numerical simulation of the interference pattern. One can see that the experimental and simulated images are similar. In

the picture, the flat islands correspond to destructive interference and the narrow channels correspond to constructive interference fringes. The size of the interference pattern on the sample was approx. 1 cm^2 with a periodicity of 1.4 μm. The height profile in Figure 2-3 shows the variety in surface relief along the dashed blue lines.

2.1.4. NANOSPHERE LITHOGRAPHY

Nanosphere lithography (NSL), also called natural lithography, is a nanopatterning method which combines top-down and bottom-up approaches and uses spontaneous self-assembly of nanoparticles [3]the complexity of the process combined with high equipment costs makes the conventional lithographic techniques unfavorable for many researchers. Through years, nanosphere lithography (NSL. Typically, the preparation of a sample in this technique consists of two basic stages:

1. creation and deposition of a layer (matrix) of nanoparticles on a durable substrate
2. nanopatterning of thin films using the matrix

There are four basic methods for producing a matrix of nanoparticles. Historically, the first is the drop method described by Micheletto et al. [4]. In this approach, a drop of nanoparticle suspension is placed on inclined substrate. By controlling the temperature and humidity of the environment, the liquid phase is slowly evaporated, leaving a layer of nanoparticles on the substrate. This method means that ordering only takes place on very small surfaces (up to several hundred square micrometres). An additional disadvantage with this approach is the high probability of accidentally obtaining multilayers consisting of several overlapping layers of nanoparticles.

The second method is dip coating. In this approach, the substrate is initially immersed in the suspension of nanoparticles and then slowly pulled out. This method is effective in covering large areas, but the layer of nanoparticles contains a large number of defects. The key parameter responsible for the final result is the speed of the substrate extraction. Pulling it out too quickly causes gaps and discontinuities in the film. Conversely, too slow a movement of the substrate results in a heterogeneous structure of overlapping layers. Other important parameters of the process are air humidity and temperature, which affect the evaporation rate of the liquid phase.

A nanoparticle matrix can also be created by spin coating. The suspension is spread centrifugally on a substrate by fast rotary motion (100–8,000 rpm). This guarantees a homogeneous distribution of the nanoparticles over the entire surface of the substrate. When the layer of suspension is thin enough, the nanoparticles start to order. This is quite a popular approach that allows large matrices to be produced quickly, although evaporating the liquid too rapidly or selecting an incorrect rotation speed in relation to the viscosity of the suspension can lead to a disordered layer. Another disadvantage is the difficulty in obtaining long-range ordering on a large scale.

These drawbacks do not occur for the self-assembly method conducted at the interface of two liquids, most commonly water and air. After selecting the appropriate

process parameters (e.g. surface tension, temperature, pH, and ambient humidity), the nanoparticles remain on the liquid surface and crystallise into an ordered matrix. This method does not require expensive and specialised equipment but provides ordering on large areas (in the order of cm^2) with good reproducibility. An example of a matrix obtained by this method is shown in Figure 2-4, where monolayers of polystyrene particles of three different diameters are presented.

After the matrix has been formed, in the second stage of patterning a thin layer of material is deposited onto the nanoparticles. After the matrix is removed, a layer corresponding to regions not covered by nanoparticles remains on the substrate. In the simplest case, a network of triangular islands is created (see Figure 2-5e–g). Before deposition, the nanoparticles can also be diminished (e.g. by plasma etching), which results in a separated array of nanoparticles. In this case a deposited layer will form a matrix of holes (antidotes) as shown in Figure 2-5e–g. If the step of removing the matrix is omitted, the resulting structure maps the topography of the nanoparticles.

The final effect of nanopatterning depends on several factors:

- the size, shape, and chemical composition of the nanoparticles used to produce the matrix
- the size distribution of the nanoparticles (monodisperse or multimodal)
- the course of the crystallisation process and the order parameter of the matrix
- the substrate morphology
- the number of monolayers in the matrix
- any complementary processes used during the patterning (e.g. heating, plasma etching, etc.)

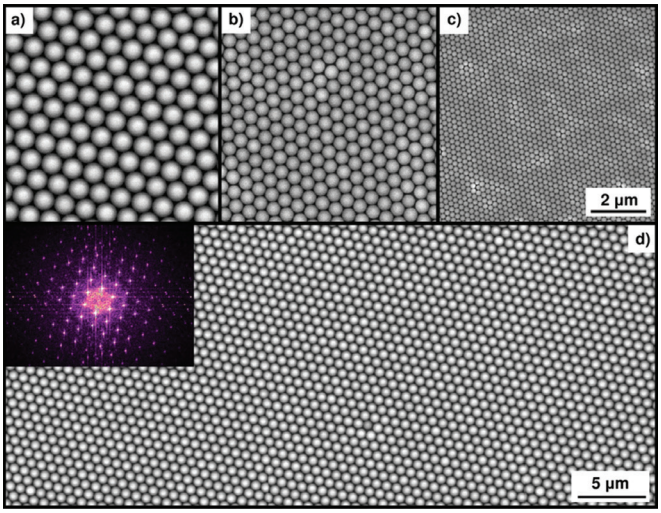

Figure 2-4. SEM images of PS nanosphere monolayers with periods of (a) 784 nm, (b) 508 nm, and (c) 202 nm self-assembled on Fe60Al40 film samples. (d) Low-magnification SEM image of the nanosphere mask with a period of 784 nm, showing long-range ordering. The inset shows a 2D Fourier transform confirming the hexagonal long-range order [48]

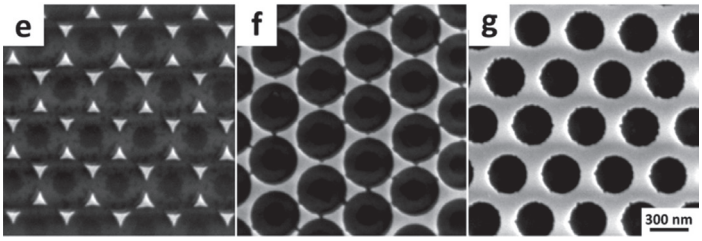

Figure 2-5. SEM images of arrays with a period of 438 nm. The coverage of sample surfaces with magnetic material amounts to (e) 7%, (f) 16%, and (g) 55% [49]

There are different variations and modifications of the nanosphere lithography. In particular, it can be supplemented by spontaneous solid state dewetting (SSD), which leads to the creation of ordered nanoparticle arrays. SSD is induced by thermal processing such as annealing or laser and ion beam irradiation. The temperature starts the surface diffusion of atoms, which usually begins at the edge of the film; due to the large gradient of edge curvature atoms move from the edge to the middle of the film, leading to the retraction and thickening of the edges and the creation of holes. This leads to the separation of the thin film into nanoparticles, whose position is determined by the morphology of the substrate. This effect can be accelerated by using a patterned substrate with a large curvature of the surface, such as self-assembled arrays of nanoparticles. An example result of such a process is shown in Figure 2-6, where arrays of FePdCu nanoparticles were obtained on a matrix built of SiO_2 nanoparticles with a diameter of 100 nm.

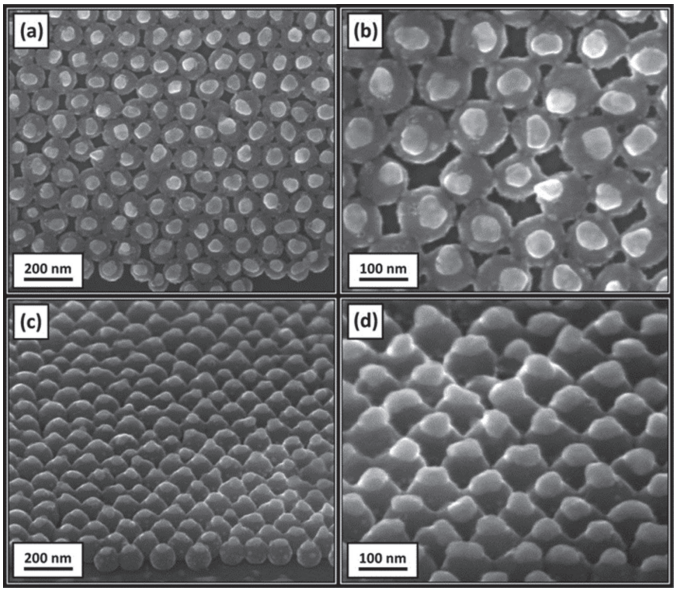

Figure 2-6. Arrays of 100-nm nanospheres covered by an FePdCu alloy with 5 at.% of the Cu admixture. Photos (a) and (b) were collected with an incidence angle of 0° while (c) and (d) had an incidence angle of 45°. Alloy islands appear bright due to the charging effects [50]

2.1.5. ANODISATION

Anodisation is an electrochemical process which is used as a simple method for fabricating self-ordered nanoporous materials. In this process, the metal surface is oxidised in a selective way, which leads to the creation of elongated pores with adjustable diameters from below 10 nm to 100 nm or more. Such a process can be performed only for selected metals, such as Hf, Zr, Nb, Ta, and Ti, but most often it is carried out for aluminium, which provides the best control of the surface morphology. In this case the resulting nanoporous layer is referred to as Anodic Aluminium Oxide (AAO).

The production of AAO membranes uses electrolytes with a pH less than 5, for example, sulphuric acid (VI), oxalic acid, or phosphoric acid (V). The process is carried out in a dedicated chamber, as shown in Figure 2-7. The housing of the anodisation chamber is made of a material that does not interact chemically with the acidic electrolyte (e.g. Teflon). The temperature control at the metal/electrolyte interface is provided by a Peltier element, which requires a separate power supply. The entire system is cooled with water. The cathode and the anode are supplied with direct current. Electrolyte mixing provides a free flow of ions at the electrolyte/oxide boundary, which leads to stable oxide growth and improves the order parameter of the membrane [5].

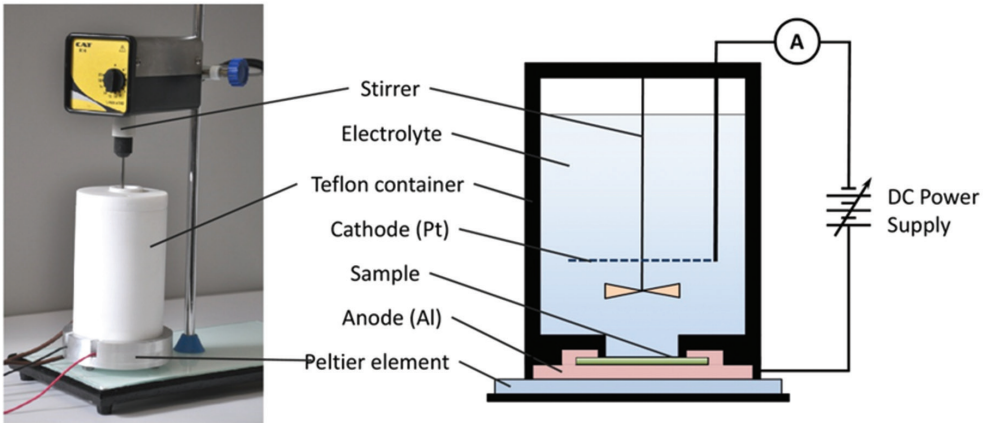

Figure 2-7. Photo and schematic cross-section of the experimental setup for anodisation of thin aluminium films [51]

The main factors affecting the pore diameter and the distance between them are as follows:

- the type of acid
- the pH and concentration of the electrolyte
- the voltage applied to the anode
- the temperature

At the beginning of the anodisation process, the surface of the aluminium is covered with a continuous, thin layer of aluminium oxide. Next, Al^{3+} ions migrate from the metal through the metal–oxide phase boundary to the oxide layer. Simultaneously, O^{2-} ions forming from water at the oxide–electrolyte interface migrate to the oxide layer. During this phase, about 70% of the aluminium ions form a barrier layer, while the remaining Al^{3+} ions dissolve in the electrolyte. In the next steps, further oxide formation renews the barrier layer and the oxide transforms into a hemispherical bowl of constant thickness, which forms the basis of the pore.

During the formation of the porous oxide layer, the Al dissolution reaction is carried out on the anode as described below:

$$2\ Al \rightarrow 2\ Al^{3+} + 6\ e^{-}$$

At the same time, hydrogen production occurs at the cathode:

$$6\ H^{+} + 6\ e^{-} \rightarrow 3\ H_2$$

At the metal–oxide interface, aluminium oxidation occurs:

$$2\ Al + 3\ O^{2-} \rightarrow Al_2O_3 + 6\ e^{-}$$

At the oxide–electrolyte interface, Al^{3+} cations react with water molecules:

$$2\ Al^{3+} + 3\ H_2O \rightarrow Al_2O_3 + 6\ H^{+}$$

Finally, the anodisation equation can be written as follows:

$$2\ Al + 3\ H_2O \rightarrow Al_2O_3 + 3\ H_2$$

An electrical field accelerates the ions which form the oxide layer on the oxide–metal interface. The field is the factor that controls the pore diameter through the applied voltage. At the same time, the oxide dissolves at the oxide–electrolyte interface. The balance between these two processes ensures the stability of the oxide growth. The oxide covers the entire base of the pores and grows perpendicularly to the metal surface. The neighbouring pores prevent growth in other directions, which leads to self-regulation of the structure. The thickness of the pore walls is also self-adjusted so that the distance between the pores is homogenous across the substrate. The time of the anodisation and the purity of the metal are the main factors which affect the above processes and determine the order parameter of the structure.

In order to obtain AAO surfaces with a higher order parameter, Masuda and Satoh [6] introduced the process of two-step anodisation. In the first step, the substrate is prepared and washed in alcohol in order to remove any organic contamination. Next, the natural layer of aluminium oxide is removed by the process of chemical polishing. Fresh, uncovered aluminium yields a highly ordered result due to fewer defects. The material prepared in this way is first subjected to an anodisation process, where the standard porous alumina is formed. The oxide is then dissolved in an

acidic mixture. This can be performed with phosphoric acid mixed with chromic acid anhydride at 80°C for 15 min. The presence of chromium (VI) oxide prevents the reaction of aluminium with phosphoric acid, thus protecting the Al substrate from etching. In this process the periodically shaped metal surface is exposed. The ordered bowls located at the oxide–metal interface will serve as starting points for the second anodisation, which will bring long-range ordering of parallel pores of the same diameter.

Schematically, the production of AAO with a high degree of order requires the following steps:

4) preparation of the aluminium surface
5) first anodisation
6) removal of the top layer of aluminium oxide
7) second anodisation

Nanoporous aluminium oxide can serve as a matrix for further deposition of thin films, as with the process discussed in the chapter concerning nanosphere lithography.

2.2. CHEMICAL METHODS

2.2.1. THE LANGMUIR–BLODGETT TECHNIQUE

Langmuir–Blodgett (LB) films are monolayers or multilayers of surface-active organic compounds deposited onto a solid substrate from the surface of a liquid. The LB layers are fabricated by a device called a Langmuir–Blodgett trough, shown in Figure 2-8. It is a shallow tub filled with a given subphase (usually water), on the surface of which a film of adsorbed molecules is formed. The LB trough is used to compress the molecules into monolayers and to measure surface phenomena due to this compression.

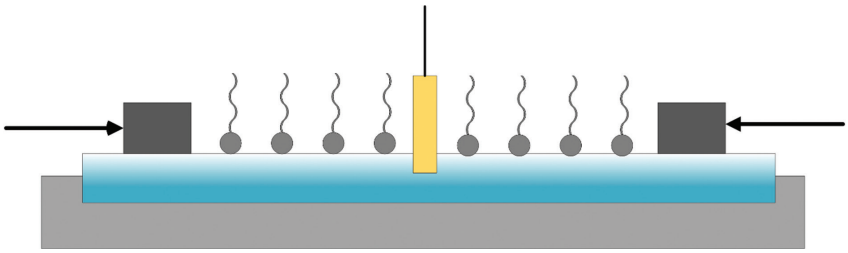

Figure 2-8. Diagram of a Langmuir trough (own elaboration)

Surfactants play a key role in the process of LB film preparation. These are a group of chemical compounds with both hydrophilic and hydrophobic properties, thanks to which the surfactant molecules arrange themselves. The hydrophobic part of

a surfactant usually consists of a hydrocarbon chain, which can be branched, linear, or aromatic. Hydrophilic components of surfactants are most often polar groups such as –OH, $–COO^-$, $–CN^-$, $–SO_4^{2-}$, and $–SO_3^-$. The hydrophobic tails prefer contact with air over contact with water. Similarly, head–water interaction is more favourable than air–water interaction due to the hydrophilic nature of the heads. The overall effect is a reduction in the surface tension of water.

The most commonly used film-forming compounds are the fatty acids octadecyloaminium (ODA) and dimethylodioctadecylammonium bromide (DODAB). For the carrier phase in the Langmuir–Blogett technique, a liquid with high surface tension is usually chosen, for example water, which has a surface tension value at 25°C of $\sigma = 72.8$ N/m^2.

The parameters that characterise the properties of an amphiphilic compound are surface pressure–area isotherms (π–A isotherm), which describe the dependence of the surface pressure of the monolayer covering the subphase on the surface area available for compound molecules. Figure 2-9 presents the π–A isotherm measured for the surfactant DODAB.

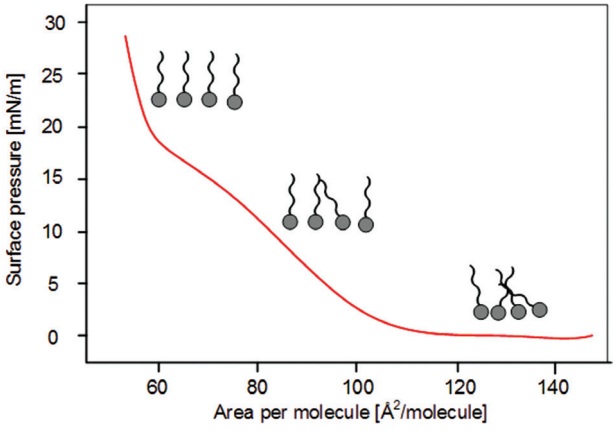

Figure 2-9. Pressure–area isotherms of Langmuir–Blodgett films of DODAB (own elaboration)

The monomolecular layers arranged on an air–water interface may occur in various physical states. When the surface tension is low, the state of the molecular monolayer resembles a gaseous phase. At higher temperatures or higher surface concentrations, the state of the monolayer is liquid. The solid state occurs when the molecules in the monolayer are fully packed to form a compact structure. Applying higher pressure at this point brings about the destruction of the monolayer and causes polylayer structures to form towards the air phase.

Molecular monolayers arranged on an air–water interface can be transferred onto solid supports. During the deposition process, the solid substrate is immersed in or

emerges from the liquid. The surface created by the tightly packed layer is controlled by the bars' movement. At this time, the monolayer molecules strongly interact with the surface of the substrate, which allows it to transfer. When dipped in the liquid solution, a hydrophilic glass substrate becomes wet with water. During its emersion the head groups can be easily attached to the surface of the glass. Finally, the transfer of the monolayer onto the glass substrate takes place. Re-immersion of this glass plate in the liquid solution brings about the transfer of a second layer with tail–tail orientation. The immersion/emersion process can be repeated several times to obtain ordered multilayers of molecules. Depending on the nature of the substrate material, different types of LB films can be formed. The schematic film deposition by this method is presented in Figure 2-10. The LB films are classified as X-type, Y-type, or Z-type; Y-type films are the most common.

The amount and quality of monolayer deposition on a solid substrate is determined by the parameter τ, called the transfer coefficient:

$$\tau = \frac{A_l}{A_s}, \tag{2-3}$$

where A_l is the surface of the monolayer on the carrier liquid and A_S is the surface of the substrate covered by the monolayer. For ideal deposition, the coefficient τ should be equal to 1. When the value of τ is close to zero, it means that the layer has not been deposited.

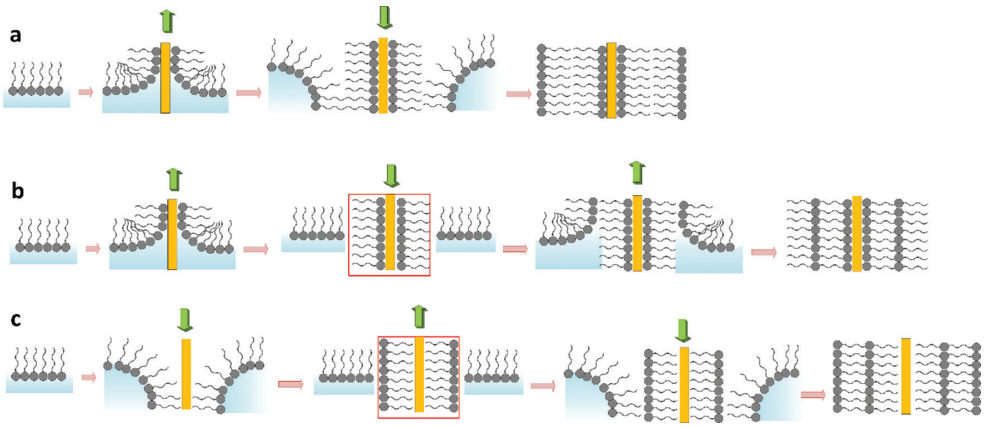

Figure 2-10. The process of Langmuir–Blodgett film deposition: (a) Y-type, (b) X-type, and (c) Z-type (own elaboration)

The Langmuir–Blodgett technique can be successfully applied in the fabrication of thin films of molecular compounds such as $M_3^{II}[Cr^{III}(CN)_6]_2$. The crystallisation process of the metal hexacyanoferrate can be carried out under a surfactant monolayer at the air–water interface in an LB trough. A compressed monolayer of a positively

charged surfactant (e.g. DODAB) can be used as a template for the formation of bimetallic cyanides by introducing equimolar solutions of $K_3Cr(CN)_6$ + MCl_2 into the subphase. An example of cubic crystals of nickel hexacyanochromate grown under an octadecylamine monolayer is presented in Figures 2-11 (TEM images) and 2-12 (AFM image).

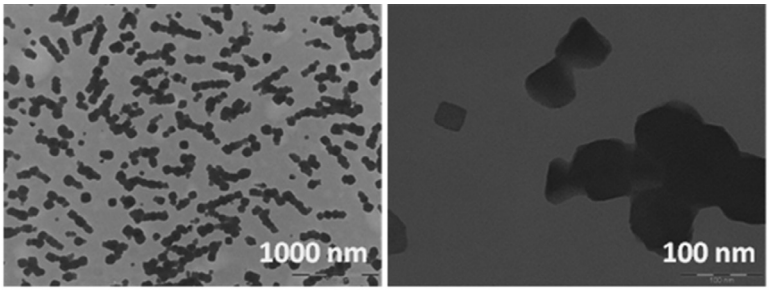

Figure 2-11. Transmission electron micrograph of a $Ni_3^{II}[Cr^{III}(CN)_6]_2$ film grown under an ODA monolayer for 15 h and transferred onto a copper grid (own elaboration)

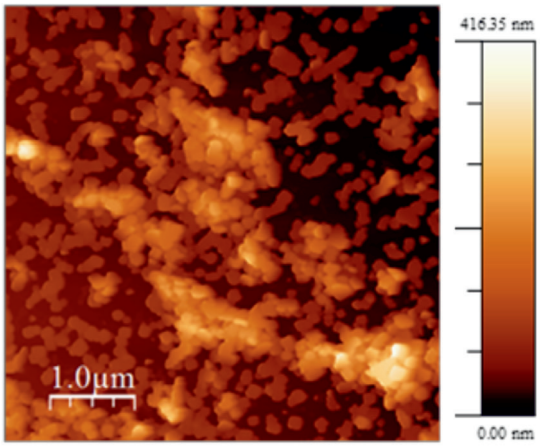

Figure 2-12. Atomic force microscopy topographic images (5 μm × 5 μm) of 5 monolayers of a $Ni_3^{II}[Cr^{III}(CN)_6]_2$ film grown under an ODA monolayer for 15 h and transferred onto a quartz substrate

2.2.2. ELECTROCHEMICAL DEPOSITION

Electrochemistry is a branch of physical chemistry that deals with the electrical aspects of chemical reactions, as well as the electrical properties of chemical compounds. A typical measuring system used in electrochemical experiments consists of a potentiostat, a measuring cell, and three electrodes (a working electrode, a reference electrode, and a counter electrode). The working electrode is a conducting substrate on which the layer grows. A thin film of indium tin oxide (ITO; 90% In_2O_3

and 10% SnO_2) deposited onto glass or PET foil is used as a working electrode. Its main advantage is its transparency, which allows the layer of the sample formed on its surface during the experiment to be measured spectroscopically without being removing from the surface of the electrode. The selection of the reference electrode depends on the type of solution being tested: for aqueous solutions, a silver/silver chloride (Ag/AgCl) electrode is often used, whereas for non-aqueous solutions, a silver/silver-ion (Ag/Ag^+) electrode is common. The counter electrode is usually a platinum wire or platinum plate. The surface of the counter electrode plays a very important role in the experiment: if a large amount of solution (30 cm^3) is used for electrodeposition, the working electrode has to be a plate with an area of approx. 1 cm^2. For smaller amount of solution, a platinum wire is sufficient.

During electrochemical experiments, electrodes are inserted into the measuring cell, filled with the solution, and then connected to the potentiostat. The solution must be enriched with electrolytes (e.g. KCl or NaCl) to ensure ionic conductivity. The potentiostat is a device that allows the voltage between the reference and the working electrode to be controlled.

The most important electrochemical methods are cyclic voltammetry and chronoculometry/ chronoamperometry. Cyclic voltammetry is a method used in the study of complex compounds to determine the standard redox potential, to estimate the number of electrons transferred, and to determine the reversibility of the redox process.

In cyclic voltammetry, the potential is measured between the working electrode and the reference electrode, while the current is measured between the working electrode and the counter electrode. A plot of the potential changes over time is presented in Figure 2-13. This potential ramps linearly over time in cyclical phases between the minimal (E_p) and maximal (E_k) values.

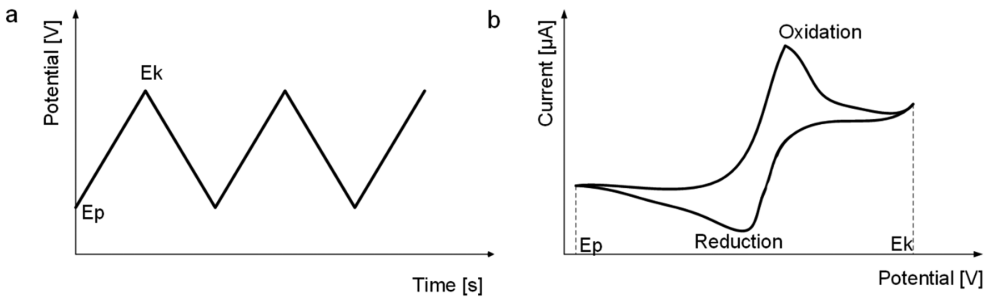

Figure 2-13. (a) Cyclic voltamperometry excitation signal; (b) Voltammogram of a single electron oxidation-reduction (own elaboration)

If the solution contains an electrochemically active substance, at some potential it undergoes the process of oxidation or reduction. This results in an increase in the measured current. Moreover, an increase in the measured current is observed

due to the linear increase in potential, since electrolysis of the examined substance becomes easier. During a cyclic voltamperometry experiment, the solution is not mixed; therefore, after a certain time, the diffusion layer of the electrode will not have any more of the active substance, and a decrease in the measured current will be observed. Typical cyclic voltammograms show two peaks related to cathodic and anodic current for a reversible reaction. In the reversible processes, the current intensity at the peak can be expressed by the relationship called the Randles–Ševčík equation:

$$i_p = 0.4463nFAc\sqrt{\frac{nFD\nu}{RT}}, \tag{2-4}$$

where n is the number of electrons, F is the Faraday constant (F = 96485 C/mol), R is the ideal gas constant (R = 8.3145 J/molK), T is the temperature, A is the area of the working electrode, D is the diffusion coefficient of the electroactive substance, c is the concentration of the electroactive substance in the measured solution, and ν is the potential scan rate.

The second, equally widely used method of electrodeposition is chronoamperometry. In this technique the potential of the working electrode is stepped and the resulting current from faradaic processes occurs at the electrode. The current is monitored as a function of time and can be described by the modified Cottrell equation:

$$I(t) = nFAD^{(1/2)}\frac{C^0}{\pi^{1/2}t^{1/2}}, \tag{2-5}$$

where n is the number of electrons, F is the Faraday constant, A is the area of the working electrode, D is the diffusion coefficient of the reagent, C^0 is the reagent's concentration, and t is the time.

The electrochemical methods described above are widely used in the preparation of thin films and nanorods of metals, metal oxides, and molecular magnets. The advantages of these methods are the short synthesis time and the precise control of the thickness of the electrochemically deposited film, which is closely related to the amount of charge flow during the electrodeposition process.

Electrodeposition can be used for the fabrication of thin films of molecular magnets, mainly Prussian blue analogues. A diagram of the film's growth is presented in Figure 2-14. The application of the appropriate potential to the system results in the reduction of the M^{3+} ion to the M^{2+} in the vicinity of the working electrode. Afterwards, the reduced M^{2+} ions combine with the $[Cr^{III}(CN)_6]^{3-}$ complex and a layer is formed on the surface of the electrode [7], [8].

The morphology of the electrodeposited film of iron hexacyanochromate is presented in Figure 2-15.

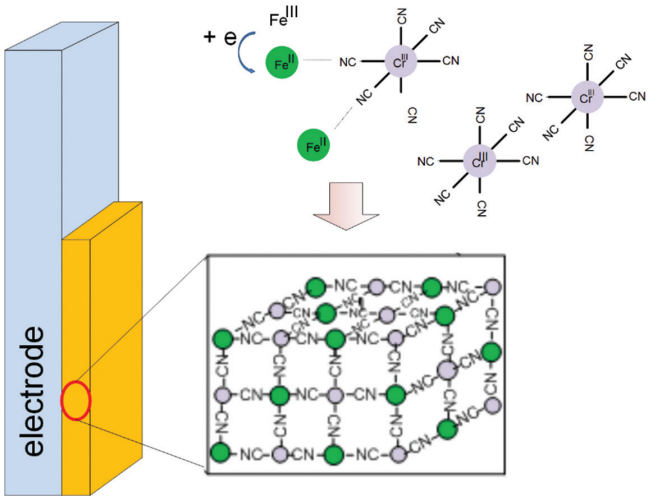

Figure 2-14. The process of electrodeposition of a $Fe_3^{II}[Cr^{III}(CN)_6]_2$ thin film (own elaboration)

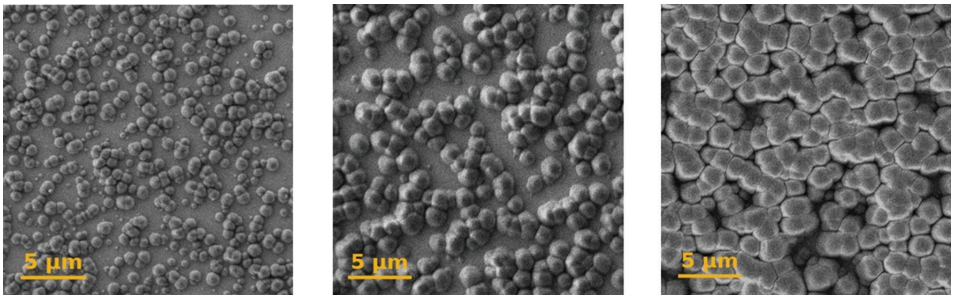

Figure 2-15. SEM images of $Fe_3^{II}[Cr^{III}(CN)_6]_2$ thin films deposited on a PET/ITO substrate with the reduction time of (a) 50 s, (b) 100 s, and (c) 200 s (own elaboration)

2.2.3. LAYER-BY-LAYER DEPOSITION

The technique of layer-by-layer deposition, also called the electrostatic self-assembly method, consists of alternating adsorption of molecular layers of oppositely charged polymers, nanoparticles, or other molecules [9], [10]. Attracting the opposite sign's charges is the driving force of the layer formation. In comparison to the classic Langmuir–Blodgett method, the advantage of this method is that adsorption takes place in the solution, so it does not depend on the shape and topology of the substrate. As a result, homogeneous layers which cover the substrate completely are obtained.

The process of the layer deposition can be explained based on Figure 2-16, which presents a glass substrate immersed successively into four solutions [11]. The first and third steps represent the adsorption of anions and cations, whereas steps 2 and

4 show the substrate being rinsed in water. Such a four-step sequence produces the simplest architectures $(A/B)_n$. In order to obtain a more complicated system, the adsorption sequence must be modified by adding more solutions.

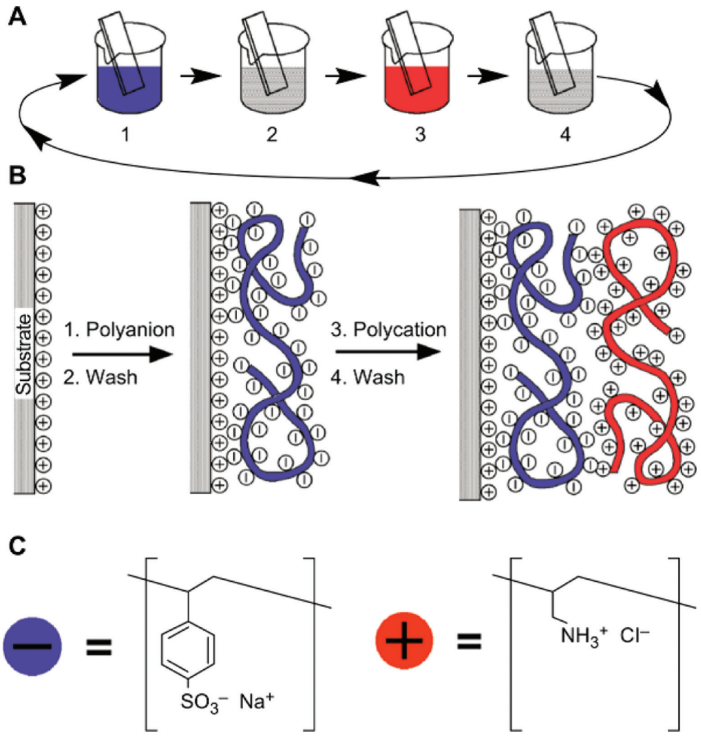

Figure 2-16. The process of film deposition in layer-by-layer deposition [11]

The above-mentioned method can be adapted for creating layers of hexacyanometalates of transition metals. In these types of layers, a properly prepared substrate plays a very important role. To ensure a high adsorption of ions on the surface of the substrate (e.g. glass), it should be covered with a thin layer of a positively charged substance, such as a polymer or cationopolymer. Then, two solutions with concentrations of several mmol/dm^3 should be prepared: the first containing the salt of an appropriate metal (e.g. $FeCl_2$ or $CrCl_2$), the second containing ions $[M^{III}(CN)_6]^{3-}$ (M = Fe or Cr) from solution $K_3[M^{III}(CN)_6]$. The use of the sequence shown in Figure 2-17 leads to adsorption of the hexacyanometalate complex on the surface of the substrate in the first step, and in the next step the metal cations are incorporated into the forming network from the second solution. The SEM microphotographs recorded for these films are presented in Figure 2-18.

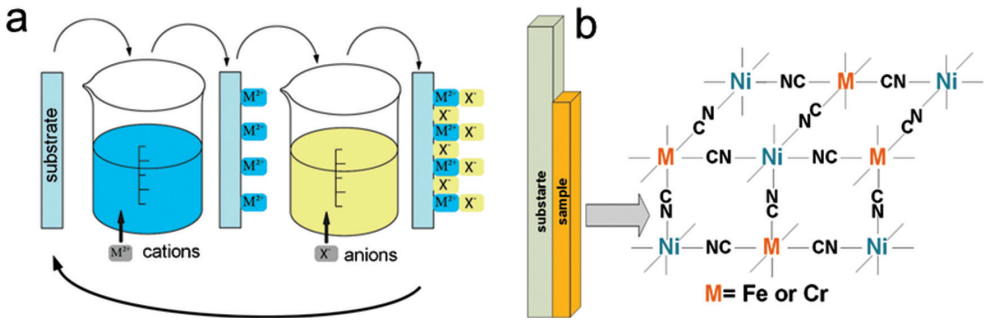

Figure 2-17. (a) The sequential adsorption procedure for fabricating Prussian blue analogue thin films; (b) The crystalline structure of Prussian blue analogues (own elaboration)

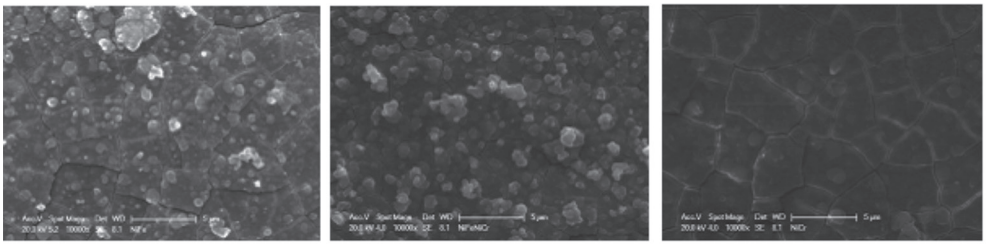

Figure 2-18. SEM images of $Ni_{1.5}[Fe(CN)_6]_x[Cr(CN)_6]\times nH_2O$ (x = 0, 0.55, and 1) thin films (own elaboration)

3. INTRODUCTION TO SURFACE PHYSICS

The surface of a solid is a special type of interface: a small number of atomic layers (usually 2–3) that surround the solid and are in contact with the surrounding world, i.e. the atmosphere. The properties at the surface differ from those in bulk materials because quantum-sized effects come into play and because there are extremely large surface areas per unit volume at the nanoscale. Although the properties of bulk materials are understood very well, the properties of nanoscale systems still have not been fully explored.

Nanopatterned objects and surfaces have completely different properties than micro- and bulk materials. The main reason for these differences is usually the higher specific surface area. As the volume of an object becomes smaller, the ratio of the surface area to the bulk form becomes larger, so atoms on the surface contribute more to the behaviour of the object than those in the bulk material.

Let's consider a cubic nanoparticle with an edge length of 10 nm. For simplicity, let's assume that the atoms within it form a simple cubic network, and each of them has a diameter of 0.2 nm. That means that 50 atoms form one edge of the particle. It is easy to calculate that 125,000 atoms comprise the entire particle. Now, let's calculate how many atoms form the surface. The reader can easily see that there are 14,408 of them, which means that they constitute about 11.5% of all atoms. The share of the surface is therefore significant, much larger than for bulk materials, where it can usually be neglected. If a similar calculation is made for a cubic particle that is 2 × 2 × 2 nm, the proportion of surface atoms increases to 48.8%, and for a particle with dimensions of 1 × 1 × 1 nm, this further increases up to 78.4%. This demonstrates that the smaller the particle size or the smaller the elements, the larger the proportion of surface atoms. The share of surface atoms also depends on the shape of the particle. Similar calculations for spherical particles with diameters of 10 nm, 2 nm, and 1 nm show that the atoms on their surfaces will constitute 22.1%, 78.4%, and 99.2% of all the atoms in the particle, respectively.

However, regardless of the shape of the particles, it is always true to say that nanostructures have a very large specific surface area. This increases the number of unsaturated coordination sites, defects, and stresses in the crystal lattice. The atoms on the surface change the coordination environment, which influences the electrical structure and determines the change in the physical and chemical properties of the

nanoobjects. As a result, nanomaterials show unique properties manifested in the following areas:

- magnetic properties
- conductivity
- hydrophilicity
- biocompatibility
- chemical and mechanical resistance
- durability
- plasticity
- hardness
- adsorption capacities

It is not possible to discuss all these properties in this short handbook, so here we focus mainly on the magnetic properties as a representative area that can demonstrate the most important features of the physics of nanosurface systems.

3.1. EQUILIBRIUM THERMODYNAMICS

The internal energy U represents the total energy of the system, which is the sum of kinetic energy and potential on both the microscopic and macroscopic scales. In equilibrium, a single-component bulk system can be completely characterised by internal energy, which is a function of entropy (S), volume (V), and the number of moles (N) in the system.

$$U = U(S,V,N), \tag{3-1}$$

$$dU = \left(\frac{\partial U}{\partial S}\right)_{V,N} dS + \left(\frac{\partial U}{\partial V}\right)_{S,N} dV + \left(\frac{\partial U}{\partial N}\right)_{S,V} dN, \tag{3-2}$$

$$dU = TdS - pdV + \mu dNdU = TdS - pdV + \mu dN. \tag{3-3}$$

These equations define the temperature $T = \left(\frac{dU}{dS}\right)_{V,N}$, pressure $p = \left(\frac{dU}{dV}\right)_{S,N}$, chemical potential $\mu = \left(\frac{dU}{dN}\right)_{S,V}$ of the bulk material.

The internal energy of the system is an extensive quantity, which means that it depends on the amount of substance in a given system:

$$U(\kappa S, \kappa V, \kappa N) = \kappa U(S,V,N), \tag{3-4}$$

where κ is a factor by which the system is enlarged. Differentiating with respect to κ yields

$$U(S,V,N)=\left(\frac{\partial U}{\partial(\kappa S)}\right)_{V,N}\frac{\partial(\kappa S)}{\partial\kappa}+\left(\frac{\partial U}{\partial(\kappa V)}\right)_{S,N}\frac{\partial(\kappa V)}{\partial\kappa}+\left(\frac{\partial U}{\partial(\kappa N)}\right)_{S,V}\frac{\partial(\kappa N)}{\partial\kappa}, \quad (3\text{-}5)$$

which simplifies to

$$U(S,V,N)=\left(\frac{\partial U}{\partial(\kappa S)}\right)_{V,N}S+\left(\frac{\partial U}{\partial(\kappa V)}\right)_{S,N}V+\left(\frac{\partial U}{\partial(\kappa N)}\right)_{S,V}N. \quad (3\text{-}6)$$

Recalling that the value of κ is arbitrary, we now choose κ = 1, resulting in

$$U(S,V,N)=\left(\frac{\partial U}{\partial S}\right)_{V,N}S+\left(\frac{\partial U}{\partial V}\right)_{S,N}V+\left(\frac{\partial U}{\partial N}\right)_{S,V}N; \quad (3\text{-}7)$$

recognising that the partial derivatives in this equation are now just the definitions of the extensive variables T, p, and μ, Equation 3-7 can be rewritten as

$$U=TS-pV+\mu N. \quad (3\text{-}8)$$

Equation 3-8 is known as a Euler equation, one that relates to seven thermodynamic variables. By differentiating Equation 3-8, we obtain

$$dU=TdS+SdT-pdV-Vdp+d\mu N+\mu dN. \quad (3\text{-}9)$$

Combining Equations 3-3 and 3-8, we obtain the Gibbs–Duhem equation:

$$SdT-Vdp+Nd\mu=0. \quad (3\text{-}10)$$

3.2. SURFACE TENSION Γ

One of the fundamental parameters in surface physics is surface tension (γ). The creation of the surface affects the interatomic bonds, which leads to an increase in the average energy of atoms that are close to the surface. Surface tension is defined as the energy required to create a surface with area A, at temperature T, volume V, and constant chemical potential μ:

$$\gamma=\left(\frac{\partial F}{\partial A}\right)_{V,T,\mu}, \quad (3\text{-}11)$$

where F is the Helmholtz free energy, which is related to the internal energy U:

$$F=U-TS. \quad (3\text{-}12)$$

Therefore, the internal energy can be expressed as:

$$U=TS-pV+\mu N+\gamma A. \quad (3\text{-}13)$$

The surface tension also designates the excess free energy per unit area of the surface, the surface free energy. An equivalent definition of surface tension is force per unit of length.

The surface tension depends on the crystallographic face of the crystals. In equilibrium, the shape of the crystals is controlled by various surface tensions of the different crystallographic faces.

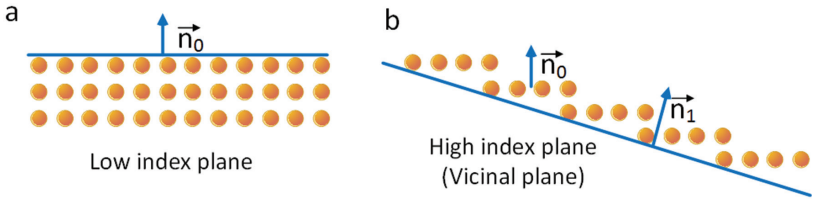

Figure 3-1. Drawings of a low-index surface and a high-index surface (own elaboration)

For vicinal surfaces (surfaces slightly misaligned with respect to a specific direction, Figure 3-1b), the small angle between the directions n_0 and n_1 is $\theta \cong \frac{1}{n}$. The surface tension along direction n_1 is affected by the surface tension of n_0 face, $\gamma(n_0)$, and by each of the individual stems. The total surface tension of the surface n_1 is described as

$$\gamma(\theta) = \gamma(n_0) + \frac{\beta|\theta|}{d}, \tag{3-14}$$

where β is the energy per step and θ is the angle between n_0 and n_1.

The anisotropy of the surface tension is represented via the γ-plot constructed by drawing a vector from the origin in direction n_1 (defined by its polar angle θ) with a length equal to the surface tension, $\gamma(n_1)$, of the surface plane perpendicular to n_1.

$\gamma(\theta)$ is minimal in the direction n_0 corresponding to the densest surface. The differentiation of Equation 3-14 shows that $d\gamma/d\theta$ has a discontinuity at $\theta = 0$, and the γ-plot shows cusps- singular point on the curve (Figure 3-2). For larger values of angle θ, the density of steps will increase and the proper calculation of surface tension must include the interaction between steps. In this situation, the sharpness of the cusp rapidly decreases.

For isotropic γ, the equilibrium shape is a sphere, while for anisotropic γ a polyhedral shape is observed. The exact crystal shape can be obtained by Wulff construction. Figure 3-3 presents examples of the Wulff's shape constructed for weakly and strongly anisotropic γ.

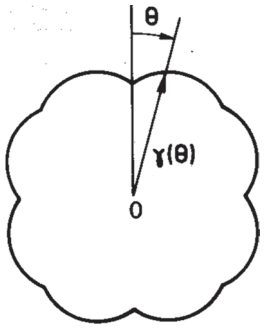

Figure 3-2. An example of a γ-plot

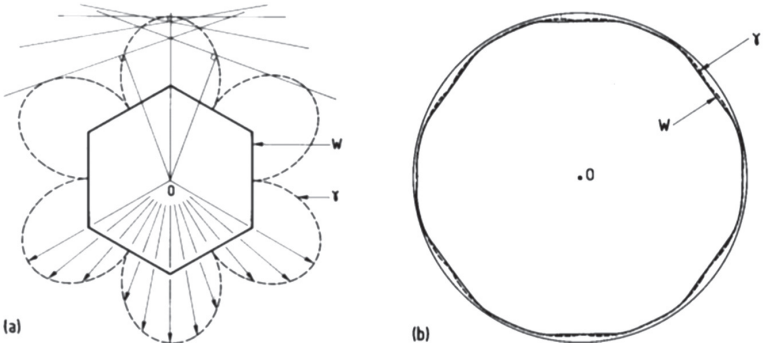

Figure 3-3. Construction of Wulff's shape for (a) a strongly anisotropic γ and (b) a weakly anisotropic γ [52]

3.3. DEFECTS

Crystallographic defects are imperfections of a crystal's structure consisting of a point or layered break in the regularity of its atoms' arrangement. In crystals, the positions of atoms or molecules occur on repeating fixed distances and these regular patterns are interrupted by crystallographic defects. Crystallographic defects are extremely difficult to eliminate whatever imperfections are introduced into the crystal during its growth, processing, or use.

Crystal structure defects can be classified by their dimension:

- 0D defects, also called point defects, affect isolated sites in the crystal structure. Some examples would be vacancies or impurity atoms, which disturb the crystal pattern at a single point.
- 1D defects are lines along which the crystal pattern is broken, e.g. dislocations.
- 2D defects are external surfaces or grain boundaries, for example, along which distinct crystallites are joined together.
- 3D defects change the crystal pattern over a finite volume. They include inclusions of second-phase particles or precipitates.

As is the case with ideal crystals, ideal surfaces with complete translational symmetry cannot exist because of entropy. Figure 3-4 illustrates the most common defects occurring on a real surface. 0D or point defects involve the following:

- adatoms – atoms adsorbed on a crystal surface
- kinks – point defects on 1D steps
- vacancies – the lattice sites which would be occupied in a perfect crystal, but are vacant
- anti-site defects – these occur in an ordered alloy or compound when atoms of different types exchange positions. This is neither a vacancy nor an interstitial nor an impurity. For example, in GaAs an As atom occupies a Ga site (AsGa) or vice versa (GaAs).

The singular terraces separated by steps are typical for vicinal surfaces.

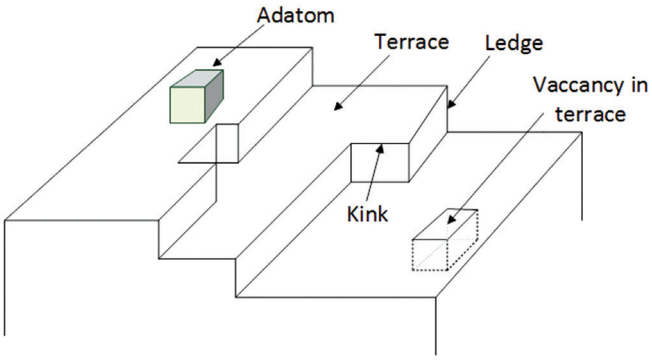

Figure 3-4. Types of surface defects (own elaboration)

3.4. MAGNETISM AT THE NANOSCALE

3.4.1. BASIC ISSUES AND DEFINITIONS

The basic parameters which characterise the magnetic properties of substances are magnetisation M and magnetic susceptibility χ. Magnetisation expresses the density of permanent or induced magnetic dipole moments in a magnetic material and can be defined as

$$M = \frac{\Delta m}{\Delta V}, \tag{3-15}$$

where m is the magnetic dipole moment and V is the volume. Magnetisation and magnetic susceptibility are connected by magnetic field strength:

$$M = \chi H. \tag{3-16}$$

Magnetic susceptibility is one of the parameters describing a magnetic system; it is a measure of how magnetised a material will become if a magnetic field is applied. In general, χ is a tensor, but for polycrystalline samples it can be treated as scalar.

Static susceptibility (also known as direct current susceptibility) is defined as the ratio of magnetisation M to a constantly applied magnetising field with intensity H_{DC}:

$$M\chi_{DC} = \frac{M}{H_{DC}}. \tag{3-17}$$

The macroscopic magnetic properties of the substance are the result of the magnetic moments in its constituent atoms and molecules. Long-range interaction between magnetic moments can lead to various types of magnetic ordering: paramagnetic, ferromagnetic, and antiferromagnetic (Figure 3-5).

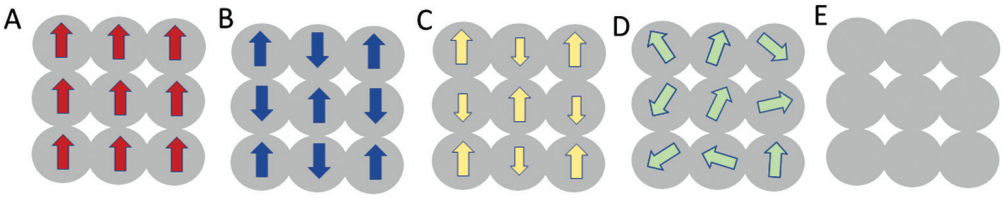

Figure 3-5. Illustrations of spin interactions for several common magnetic behaviours: (A) ferromagnetic, (B) antiferromagnetic, (C) ferrimagnetic, (D) paramagnetic, and (E) diamagnetic (own elaboration)

Paramagnets are substances that show randomly-orientated magnetic moments and a magnetisation equal to zero when no external magnetic field is applied. The application of a non-zero external magnetic field causes the magnetic moments to orientate along the direction of the applied magnetic field, leading to a non-zero value of magnetisation. The process of magnetic moment arrangement is disturbed by thermal fluctuations. The magnetisation of paramagnetic materials decreases with the increase of temperature and increases with increasing external field intensity.

Ferro-, antiferro-, and ferrimagnetism are phenomena in which a long-range interaction between unpaired electrons of paramagnetic atoms occurs. These interactions are possible due to overlapping electron orbitals and can lead to the different configuration of magnetic moments. The characteristic feature of ferromagnets is a parallel orientation of magnetic moments, resulting in a non-zero value of magnetisation even without an external magnetic field. Below the critical temperature T_c, ferromagnetic materials are comprised of small areas (1–10 μm) in which the arrangement of magnetic moments occurs. These areas are called magnetic domains. Without the presence of an external magnetic field, the orientation of magnetic moments within the particular domains do not have to be consistent, but under the influence of a magnetic field, the domains begin to align (Figure 3-6).

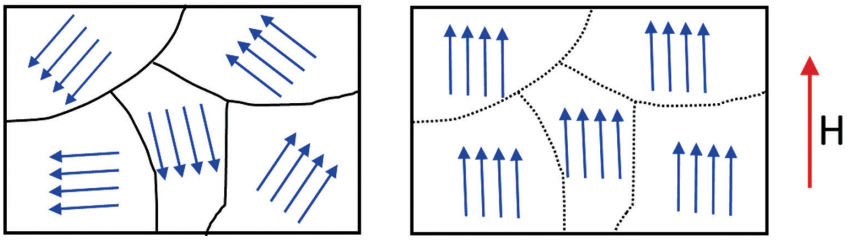

Figure 3-6. Magnetic domains of ferromagnetic materials in the absence (left) and presence (right) of a strong magnetic field applied upwards (own elaboration)

One of the characteristic macroscopic features of magnetism is magnetic hysteresis. This is observed for magnetic materials showing non-zero spontaneous magnetic moments: ferro- and ferrimagnets below the critical temperature. Magnetic hysteresis is defined by two characteristic points: M_{rem}, remanence—which specifies the value of magnetisation M at $H = 0$ and H_c, coercive field, the value of the field for which $M = 0$.

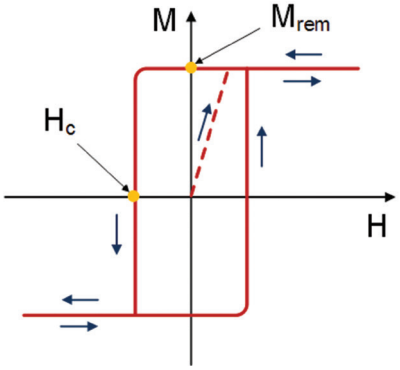

Figure 3-7. Hysteresis loop and the virgin curve (dashed line) – blue arrows indicate the sequence in which the external magnetic field is applied (own elaboration)

The coercive field value is a parameter used for classifying magnetic materials. A substance with a high H_c value (>500 Oe) are called 'hard' magnets, while materials with a low H_c are called 'soft' magnets. Figure 3-7 shows a typical hysteresis loop measured for a ferromagnetic compound.

In antiferromagnetic materials, the magnetic moments are antiparallel-orientated, so the resultant value of magnetisation is equal to zero. A special case of antiferromagnetism is ferrimagnetism. In ferrimagnetic materials, magnetic moments are antiparallel-orientated, but their values are different, which yields a non-zero value of the resultant magnetic moment.

3.4.2. MAGNETIC ANISOTROPY

Magnetic anisotropy occurs when a material exhibits distinct magnetic properties along different directions. For example, some ferromagnetic materials have distinguished axes, along which the process of magnetisation reversal takes place more easily than in other directions. These directions are called the easy magnetisation axes. When an external magnetic field is applied along these directions, M_S saturation magnetisation is reached at a lower field value and the M_R/M_S ratio is approximately 1, while the hysteresis loop is rectangular.

The existence of magnetic anisotropy is illustrated in Figure 3-8, where the dependence of the components of magnetisation on the applied magnetic field are shown for Fe, Co, and Ni crystals. It can be seen that the easy axis for Fe lies along crystallographic direction [100], whereas that for Co and Ni point to directions [001] and [111], respectively.

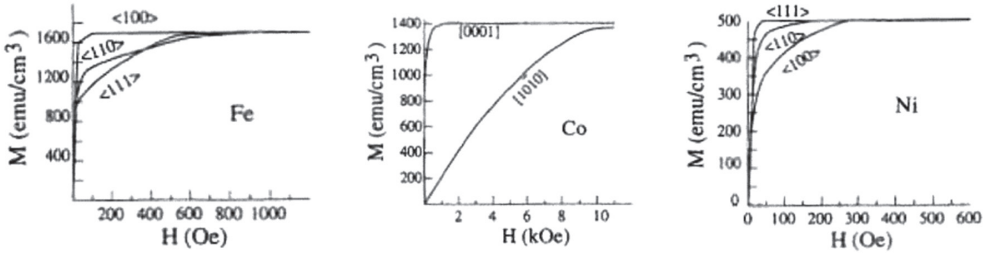

Figure 3-8. Sections of the hysteresis loop for Fe, Co, and Ni monocrystals measured for magnetic field directed along various crystallographic directions [12, 54]

Two significant sources of magnetic anisotropy are the spin–orbit interaction and the magnetic dipole interaction. Spin–orbit coupling binds spins and orbital moments, which at the atomic scale are linked to the local crystallographic structure. The energy of the system thus reaches a minimum when the spins are orientated in a specific crystallographic direction. This is the first mechanism which explains the impact of spin–orbit on the energy of magnetocrystalline anisotropy. The second is the appearance of stress in the ferromagnetic material, which can additionally modify the magnetocrystalline anisotropy and influence the magnetisation's easy axes. This contribution is called magnetoelastic anisotropy. The third mechanism is associated with the external boundaries of the sample affecting the magnetic dipole interaction, which means that its contribution depends on the shape of the sample. Therefore, it is often called shape anisotropy. For ultra-thin layers, it forces the direction of magnetisation parallel to the surface.

The breaking of translational symmetry on the surface is the source of the surface's contribution to magnetic anisotropy. In the case of multilayered systems consisting of magnetic and non-magnetic layers, a contribution from the interfaces appears because the symmetry for the spin–orbit interaction on the constituent layer surface is broken.

In thin magnetic layers the energy of anisotropy per unit of volume can be described phenomenologically as:

$$E_A = K_{eff} \sin^2 \theta, \tag{3-18}$$

where θ is the angle between the magnetisation vector and is normal to the surface. The K_{eff} anisotropy constant can be represented as the sum of the effective volume anisotropy K_V (magnetocrystalline, magnetoelastic, and shape) and the effective constant anisotropy of the K_S interface by the relation:

$$K_{eff} = K_V + \frac{2K_S}{d}, \tag{3-19}$$

where d is the thickness of the layer. The constant K_V contains the contributions from shape anisotropy, magnetocrystalline anisotropy, and magnetoelastic anisotropy. The factor of 2 in the equation appears due to the two identical interfaces for each layer.

The above equation is often used to determine the constants K_V and K_S. To do this, both sides of the equation should be multiplied by d. Then, $d \times K_{eff}$ as a function of t should be plotted. Figure 3-9 shows an example plot of this type for Co/Pd multilayers. The positive K_{eff} value corresponds to the easy direction of magnetisation perpendicular to the surface. From the slope of the graph, the value of K_V can be determined, and the intersection with the Y-axis corresponds to the doubled K_S constant. As can be seen from the graph, below a certain thickness of the magnetic layer (in this case about 13 Å), the contribution from the anisotropy of the interface prevails over the contribution from K_V, which leads to perpendicular anisotropy for thin films.

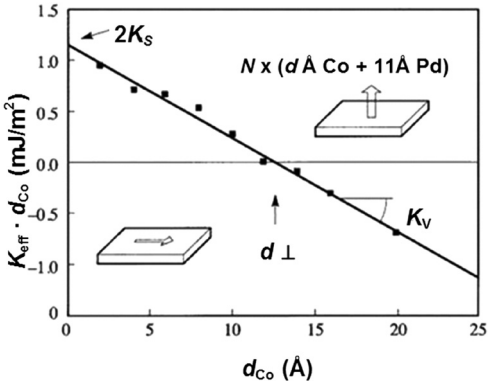

Figure 3-9. The dependence of the effective anisotropy coefficient on the thickness of a Co layer [13]

3.4.3. EXCHANGE BIAS

The phenomenon of exchange bias (*EB*) was first observed in 1956 by Meiklejohn and Bean [14]. During their measurements of the hysteresis loop for cobalt nanoparticles covered by cobalt oxide and cooled in a strong magnetic field, a shift in the *H*-axis occurred. The essential physics underlying this phenomenon is the exchange interaction between the ferromagnetic core and the antiferromagnetic shell of nanoparticles.

The origin of the *EB* is the coupling between ferromagnetic (*FM*) and antiferromagnetic (*AF*) spins at the interface. The fingerprint of the presence of the *EB* effect is asymmetric hysteresis. When the sample is cooled in the presence of a magnetic field to a certain characteristic temperature, called the blocking temperature, the hysteresis loop is asymmetrical with respect to the point $H = 0$ and is shifted by the following factor:

$$H_{EB} = \frac{H_c^+ + H_c^-}{2} \tag{3-20}$$

H_{EB} is known as the exchange bias field. The shift of the hysteresis loop and the increase in coercivity are observed only at temperatures lower than the Néel temperature, T_N (T_N is a critical temperature for the antiferromagnetic layer). The hysteresis loop measured at $T > T_N$ is symmetric, proving that *EB* is a result of local exchange coupling between the ferromagnet and the antiferromagnet across the interface (see Figure 3-10).

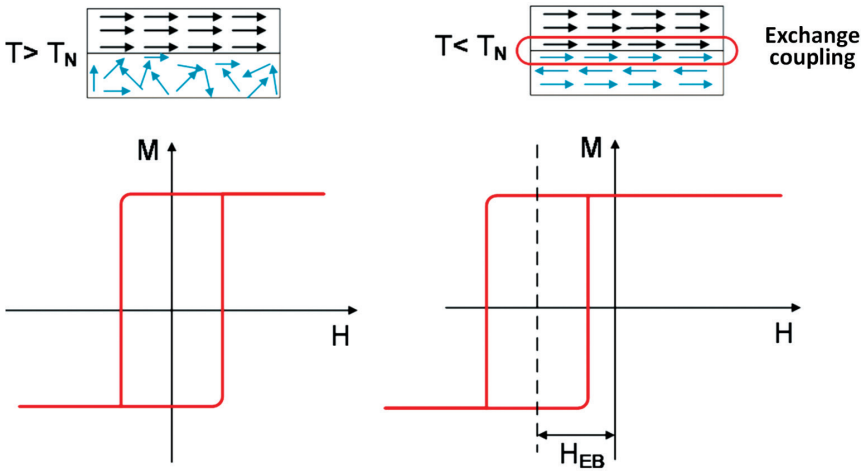

Figure 3-10. The effect of exchange coupling on the hysteresis loop of a ferromagnetic (*FM*) layer deposited on an antiferromagnetic (*AF*) layer. Above the Néel temperature (T_N), all spins of *AF* are disordered; below T_N they become ordered and the exchange coupling between *FM* and *AF* spins leads to the shift of the hysteresis loop (own elaboration)

The *EB* effect is a hot topic in research today, mainly because of its significant importance in spintronic devices. The *AF*/*FM* interaction used to control the reversal of *FM* multilayers are fundamental in hard disk construction. An example system showing the *EB* effect is the $[CoO/Co/Pd]_{10}$ multilayer presented in Figure 3-11.

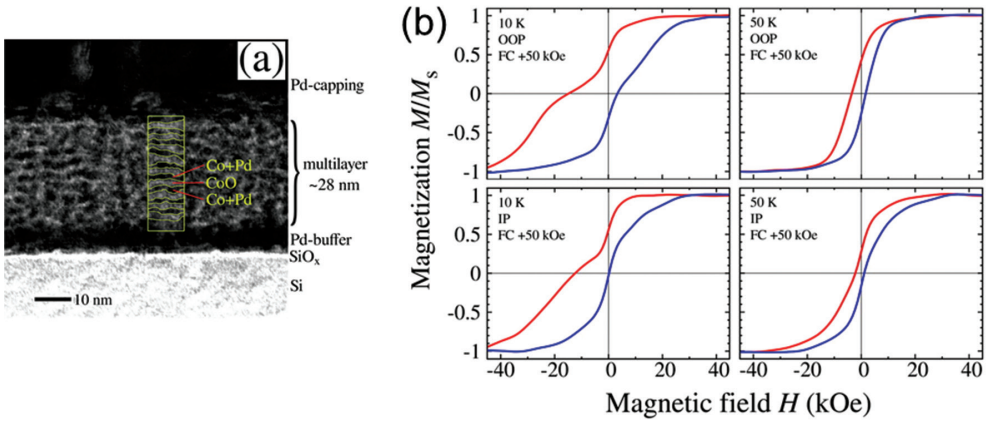

Figure 3-11. (a) TEM cross section of the $[CoO/Co/Pd]_{10}$ system. A representative region where the periodic stacking of the constituent layers is present is indicated in yellow; (b) magnetic hysteresis loops for [CoO/Co/Pd]10 multilayers measured at 10 and 50 K after cooling in +50 kOe for OOP and IP geometries [15]

3.4.4. GIANT MAGNETORESISTANCE, SPINTRONICS, AND SPIN VALVES

Spintronics is a novel area in research and technology that, unlike traditional electronics, uses the electron spin as an information carrier. The early research in the field of magnetic thin-film structures can be regarded as the beginning of spintronics. Since the early 1980s, intensive research has been carried out in many scientific laboratories to create artificial layered systems with new magnetic and electrical properties. Such systems are obtained either by vapour deposition techniques or by sputtering methods. The first success was obtaining structures composed of two iron layers separated by a layer of chromium. The most significant works were carried out by the groups of Prof. Peter Grünberg and Prof. Albert Fert—the Nobel Prize laureates in 2006.

The first important feature observed in Fe/Cr/Fe thin films was the antiferromagnetic arrangement of magnetic moment within the Fe layers. The presence of this arrangement is a consequence of the exchange interaction between the Fe layers through the chromium layer. Today, it is known that this interaction is a universal phenomenon which occurs in all metallic layered systems where two ferromagnetic layers are separated by a non-magnetic spacer. The nature of this interaction is very similar to the RKKY interaction occurring between two magnetic admixtures in a metal, (e.g. Co in Au). This interaction can be represented by the following Hamiltonian:

$$H = \frac{J\boldsymbol{M}_1 \cdot \boldsymbol{M}_2}{M_1 M_2}. \tag{3-21}$$

where M_1 and M_2 are the magnetic moments of ferromagnetic layers and J is an exchange constant. The value of J strongly depends on the nonmagnetic spacer thickness and much less on the thickness of the magnetic layers. The sign of the exchange coupling oscillates together with the thickness of the non-magnetic spacer, which means that by adjusting the spacer thickness the interlayer coupling can be set as ferromagnetic ($J > 0$), antiferromagnetic ($J < 0$), or zero. An example of oscillating exchange coupling in a CoFe/Ru/CoFe trilayer is presented in Figure 3-12, where depending on the thickness of nonmagnetic Ru layer, different values of the exchange constant can be observed.

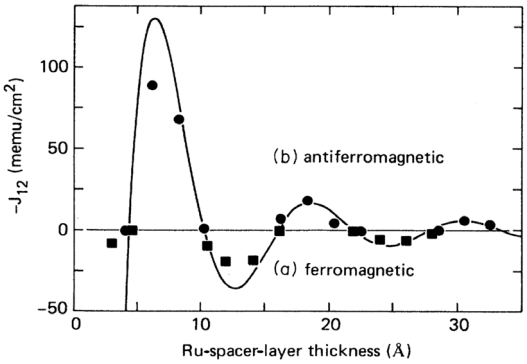

Figure 3-12. Oscillating exchange coupling in a CoFe/Ru/CoFe trilayer [16]

Now we know that the crucial role in this interaction is played by the electron gas of the non-magnetic spacer, which is polarised by the magnetic moments of the ferromagnetic layers. The oscillation frequency is a function of the electron gas's properties, defining the thickness of the spacer.

The most important discovery in magnetic multilayers is giant magnetoresistance (GMR). This phenomenon consists of a sudden decrease in electrical resistance when the orientation of the magnetic moments of the magnetic layers is changed from an anti-parallel to a parallel arrangement. GRM was observed for the first time in Fe/Cr multilayers and the dependence of the resistivity measured for this system as a function of applied magnetic field is presented in Figure 3-13.

The existence of GMR can be explained by considering the band structure: in the case of 3D metals, there is a different density of electron states with spin up (↑) and electrons with spin down (↓) at the Fermi level. The density of states with spin ↑ is usually smaller than for electrons with antiparallel spin. Apart from electron scattering with spin change, the scattering of electrons with spin ↑ and ↓ can be treated independently, which results in different probabilities of their dispersion. Figure 3-14 shows a schematic explanation of GMR.

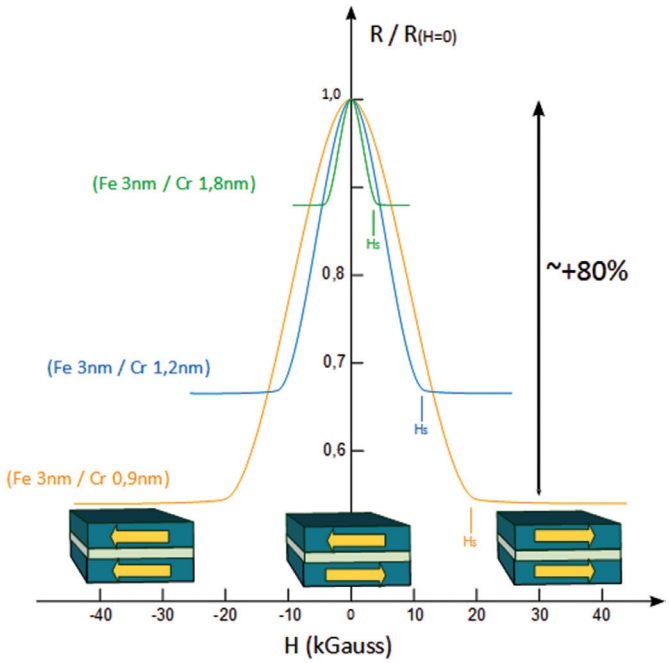

Figure 3-13. The magnetic field-dependent resistivity of three Fe/Cr superlattices at 4.2 K. The current and applied magnetic field are along the same axis [110] in CIP configuration [17]

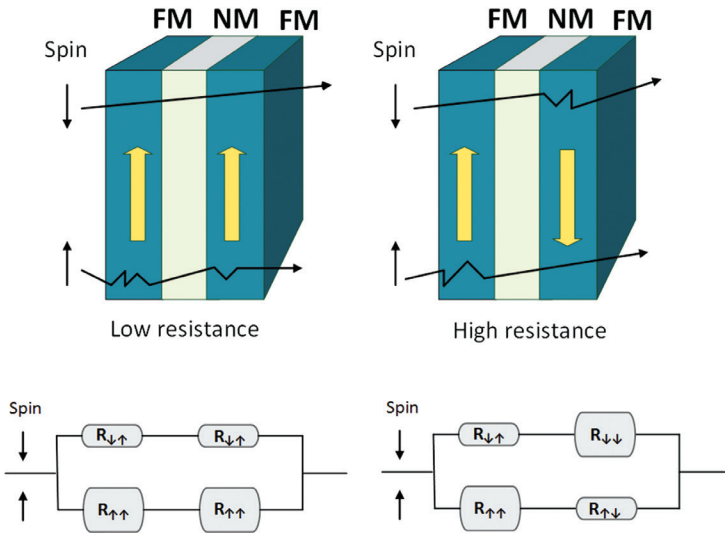

Figure 3-14. A schematic representation of GMR: a parallel arrangement of the magnetic moments in ferromagnetic (FM) layers separated by a nonmagnetic (NM) layer weakly scatters the conduction electrons, which corresponds to low magnetoresistance, while an anti-parallel orientation of the magnetic moments of the two ferromagnetic layers results in an increase (>5%) in electrical resistance (own elaboration)

Progress in the research on metallic multilayers has led to the creation of systems in which the orientation of magnetic moments in ferromagnetic layers can be changed by an external magnetic field and/or an electrical current passing through the system. A change in the orientation of the magnetisation of magnetic layers affects the transport properties of the multilayer—a GMR phenomenon may occur, causing a change in electrical resistance. Therefore, the system works like a traditional 'valve' for passing electrons. Basically, a spin valve is a system consisting of two ferromagnetic layers separated by a nonmagnetic spacer, where the first one (F1) is free and the second one (F2) is pinned (see Figure 3-15a). The F2 layer can be pinned by covering it with an antiferromagnetic thin film. Subsequently, the re-magnetisation process of F2 requires a high value of external magnetic field, which should exceed its coercive field. The phenomenon is related to the appearance of the exchange interaction between the ferro- and antiferromagnetic films. The hysteresis loop measured for the spin valve exhibits asymmetry with respect to the zero axis of magnetic field strength.

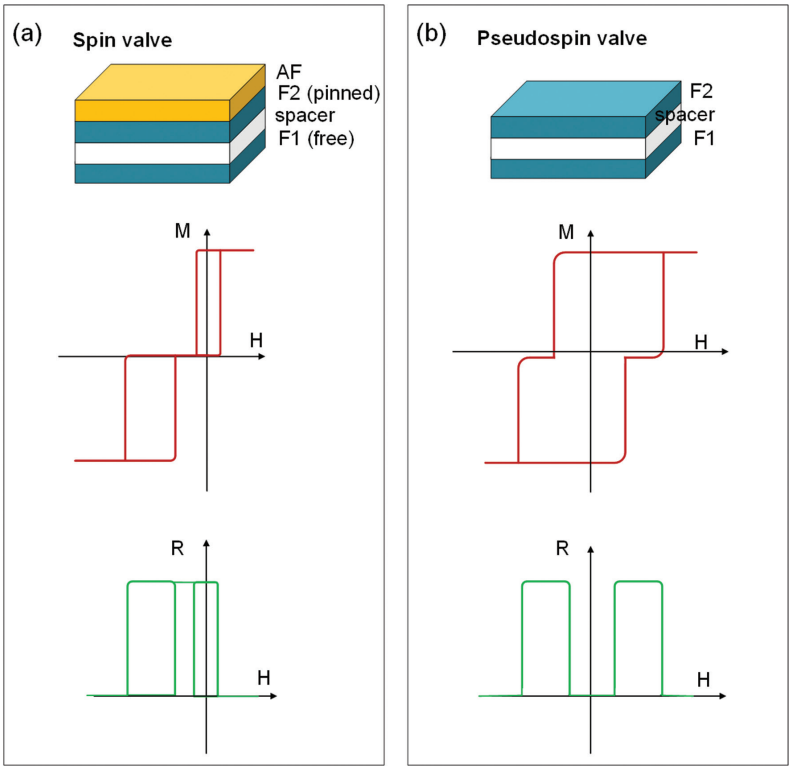

Figure 3-15. (a) A spin valve, where the coupling between the ferromagnetic layer (F2) and antiferromagnetic layer (AF) induces the exchange bias, reflected in the shift in the magnetoresistance response; (b) a pseudospin valve, where a difference in the coercivity of ferromagnetic layers F1 and F2 leads to symmetric magnetoresistance curve (own elaboration)

Another type of magnetic multilayer structure is 'pseudospin valves', constructed on two free ferromagnetic layers separated by a non-magnetic spacer, where one of the ferromagnetic layers is characterised by a large coercive field and the other by a small one (see Figure 3-15b). Such an arrangement results in an even loop of re-magnetisation and a symmetrical loop of magnetoresistance.

Spin valves are used in the read/write heads of hard drives. Figure 3-16 shows the multilayer system of a spin valve. The area responsible for the GMR is outlined in red.

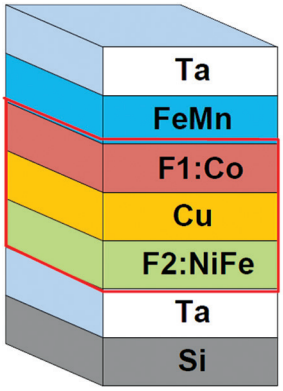

Figure 3-16. An example spin valve structure consisting of a substrate (Si), a surfactant layer to improve the growth of the other layers (Ta), a ferromagnet (F2), a non-magnetic spacer (Cu), another ferromagnet (F1), an antiferromagnet (FeMn), and a covering layer (Ta). The red outline indicates the area where GMR occurs (own elaboration)

3.4.5. TUNNEL MAGNETIC JUNCTION

Another milestone in the development of spintronics was the discovery of tunnel magnetic resistance (TMR), an effect that occurs in a magnetic tunnel junction (MTJ). The construction of an MTJ is similar to that of spin valves: it consists of two ferromagnetic layers separated by a barrier layer. The basic difference between spin valves and MTJs is the type of interlayer spacer: in an MTJ the nonmagnetic metallic interlayer is replaced by a thin film (~1 nm) of an insulator. A typical MTJ is shown in Figure 3-17.

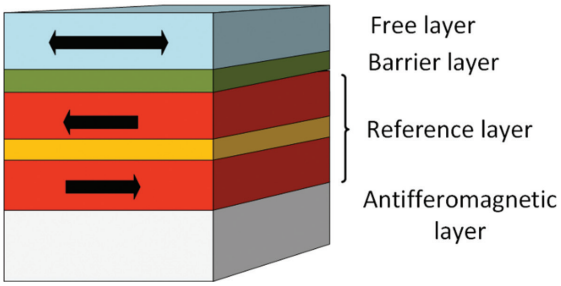

Figure 3-17. Basic structure of a magnetic tunnel junction (MTJ) (own elaboration)

The heart of an MTJ is the reference layer, consisting of two ferromagnetic films separated by a barrier layer. The magnetic moment of the reference layer should be fixed, so it is deposited on an antiferromagnetic bottom layer. The reference layer is covered by the barrier layer, which provides an energy barrier for the electrons on the two sides of it. A ferromagnetic layer, also called 'free layer', is placed on top of the MTJ. The magnetisation direction in this layer can either rotate or switch during the operation.

As in the case of a GMR effect, the resistance of an MTJ is different for parallel and antiparallel magnetic configurations of the electrodes. Due to the spin-dependent density of states of the ferromagnetic layers, different tunnelling probability of the two spin channels can be observed. Low resistance occurs when the magnetic moments of the ferromagnetic layers are orientated in parallel. Such a configuration is related to high tunnelling probability. An antiparallel alignment of the magnetic moments results in a low tunnelling probability, causing the high resistance observed in the system. The tunnel magnetoresistance ratio (TMR) is defined as a normalised difference of these two resistances and can be expressed by the formula:

$$TMR = \frac{R_{\uparrow\downarrow} - R_{\uparrow\uparrow}}{R_{\uparrow\uparrow}} = \frac{2P^2}{1-P^2}. \tag{3-22}$$

where and are the electrical resistance in the anti-parallel and parallel states, respectively, and P is the spin polarisation. TMR represents the separation of the binary states of this memory element. A schematic illustration of tunnelling through a magnetic tunnel junction is shown in Figure 3-18.

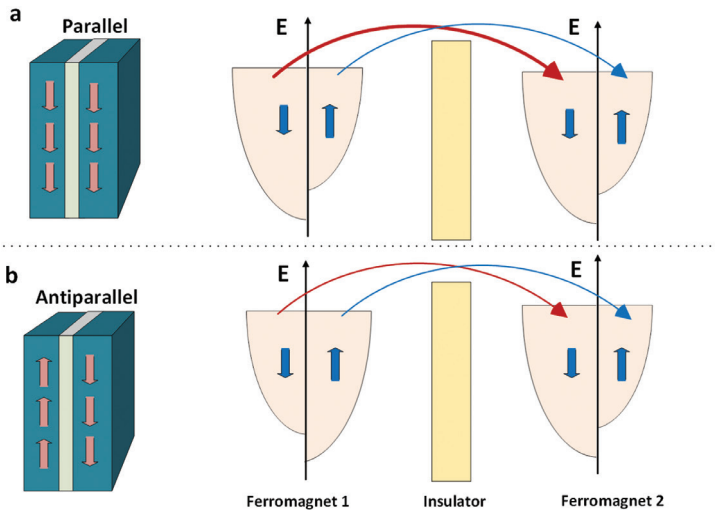

Figure 3-18. Tunnelling through a magnetic tunnel junction in (a) parallel and (b) anti-parallel magnetisation configurations. In the parallel configuration, electrons of a given spin tunnel from a density of states in the left electrode to an identical density of states in the right, while electrons in the anti-parallel configuration tunnel from one density of states in the left electrode to another in the right (own elaboration)

The TMR effect was reported by Jullière in 1975 in an Fe/Ge-O/Co system with a TMR ratio of 14% at 4.2 K [18]. Nowadays, this phenomenon is extensively studied and applied in HDD read heads and magnetic memory devices. A detailed description of these applications is provided in Chapter 5.

3.4.6. NEW TRENDS IN SPINTRONICS: ORGANIC AND MOLECULAR SPIN VALVES

Organic spintronics is an emerging field of research that deals with the study of spin injection, transport, and manipulation in multilayered systems, where organic superconductors act as nonmagnetic spacers [19]. The last few decades have seen considerable activity in the development of organic electronic devices, such as organic light emitting diodes (OLEDs) and organic photovoltaics (OPVs).

Organic semiconductors are π-conjugated molecular materials composed of light elements such as C, H, O, and N. The most important feature of organic semiconductors is long spin-relaxation times: these times range from 10^{-6} to 10^{-3} s and definitely exceed the magnitude of spin-relaxation times in most inorganic materials (10^{-9}–10^{-12} s). This makes organic semiconductors promising candidates for coherent spin manipulation logic devices. An example organic spin valve is shown in Figure 3-19. $La_{0.67}Sr_{0.33}MnO_3$ (LSMO) and cobalt were used as the magnetic electrodes [20]. LSMO is a semi-metallic ferromagnet showing a very high spin polarisation. The organic semiconductor Alq3 (with a thickness of 120–200 nm) was used as the non-magnetic spacer. The most important feature of this system is the GMR of 40%. The GMR effect decreases with increasing temperature and increasing thickness of the spacer. Decreased resistance is also observed when the configuration of the magnetic moments of the ferromagnetic layers changes from a parallel to an anti-parallel configuration. It is an opposite effect of what is observed in traditional metallic systems, e.g. Fe/Cr/Fe. This phenomenon is called negative magnetoresistance, and there is no theory that can successfully explain it. A similar effect was observed in LSMO/$SrTiO_3$/Co and LSMO/$Ce_{0.69}La_{0.31}O_{0.1845}$/Co systems. Probably for the 'reversal' of the GMR effect correspond negatively to the polarised electrons of the third orbit of cobalt, where the density of majority spin states at the level of Fermi energy is lower than the density of minority spin states.

In molecular spin valves, the resistance changes due to the different directions of the magnetic moments of the electrodes and the molecule [21]. The model molecular spin valve contains a diamagnetic molecule placed between magnetic electrodes. The first experiment with this type of system was carried out with fullerene C_{60} connected to nickel electrodes (Figure 3-20). This system exhibits a very high negative magnetoresistance. Another possibility for molecular spin valve construction is the use of a carbon nanotube attached to semi-metallic electrodes, converting spin information into an electrical signal.

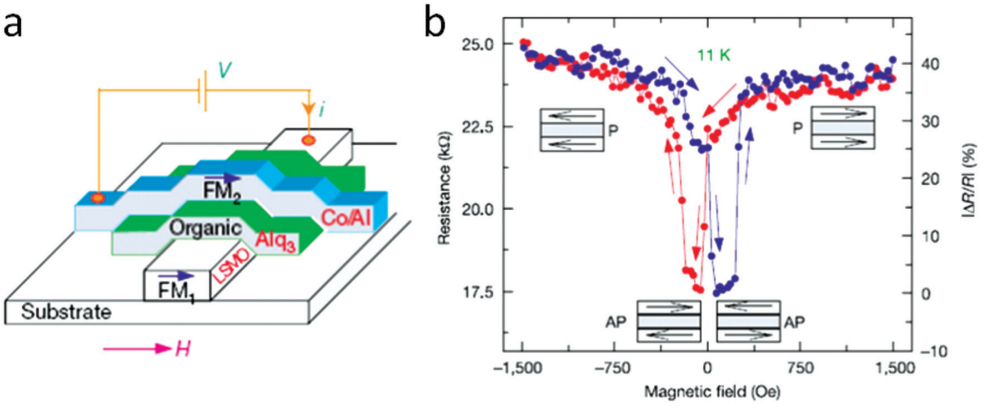

Figure 3-19. (a) A diagram of a vertical LSMO/Alq33/Co organic spin valve; (b) the magnetoresistance curve measured in an LSMO/Alq33 (130 nm)/Co junction at 11 K [20]

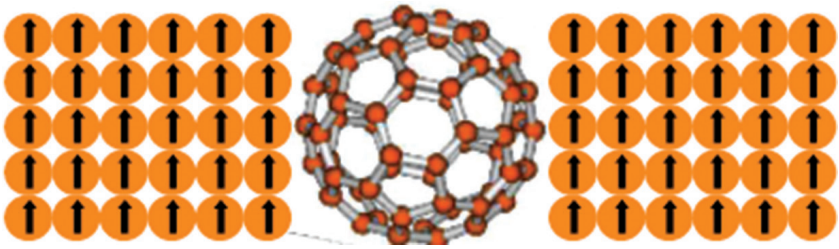

Figure 3-20. The simplest molecular spin valve, containing a fullerene molecule attached to metallic ferromagnetic electrodes [23]

A spin valve based on molecular nanoparticles would have a more complex structure. The simplest solution seems to be using molecules with two magnetic centres that could be placed between two non-magnetic elements (Figure 3-20). This solution resembles the prototype of a traditional spin valve.

Another possibility is to use a magnetic nanoparticle such as $Mn_{12}O_{12}(MeCO_2)_{16}(H_2O)_4$, called Mn12 [22]. Here, due to the non-zero magnetic moment of the molecule, one magnetic electrode and a diamagnetic drain should be used for the construction of a spin valve. The principle of operation of such a system differs from the previous examples. In Figure 3-21, the yellow arrow indicates the direction of magnetisation of the nanoparticle. With the parallel configuration of the magnetisation of the electrodes and molecules, the majority spin up electrons (green arrow) can pass freely through the molecule without dissipation. On the other hand, the minority spin down electrons actually 'drown back' and cannot get through the barrier of the molecule. With anti-parallel magnetisation of the electrode and the nanoparticles, the spin-up electrons are basically blocked by the molecule, while the spin-down electrons can pass freely. This means that in the first case, the resistance is much lower than in the second case.

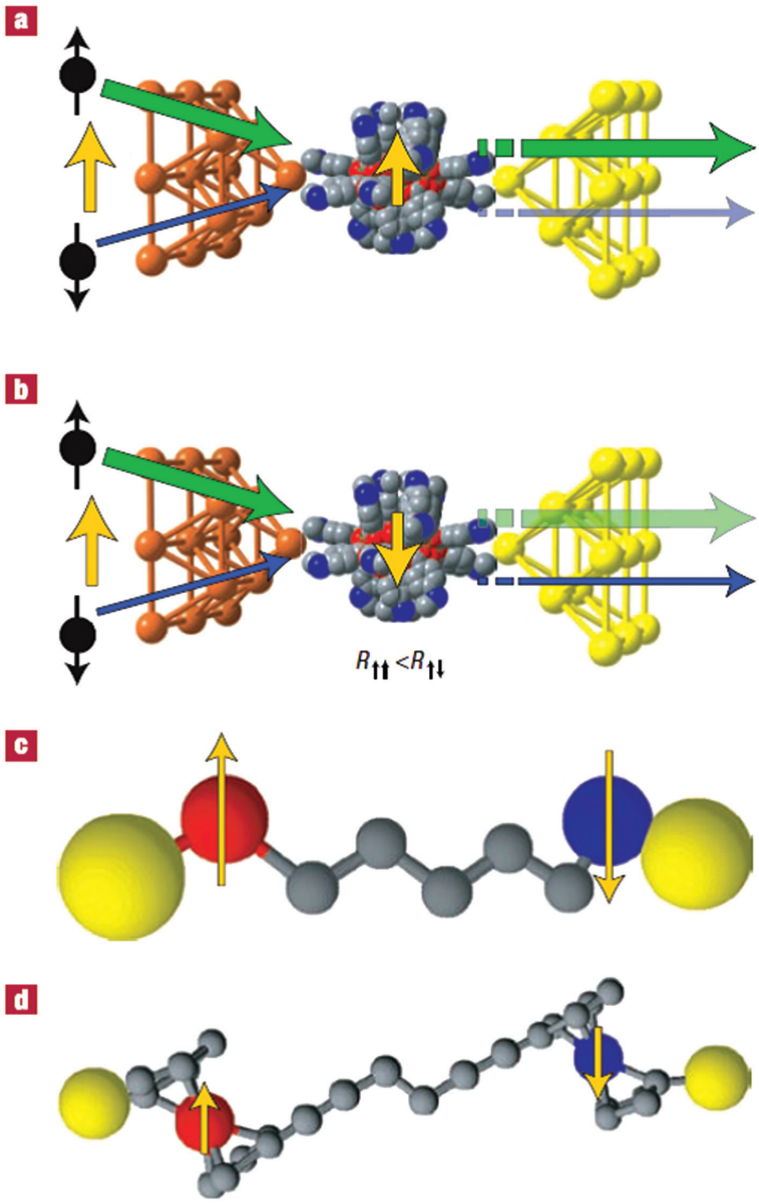

Figure 3-21. A spin valve based on a single molecule magnet and the principle of its operation. The direction of magnetisation is represented by yellow arrows. (a) A parallel configuration of the magnetic source electrode (orange) and the magnetic moments of the molecule results in spin up majority electrons (thick green arrow) to flow freely through the molecule, while minority carriers with spin down (thin blue arrow) are strongly dispersed; (b) An anti-parallel arrangement of the magnetic moments of the source and the molecule causes an increase in the resistance of the system. In this case, the majority of the spin up carriers are blocked by the molecule, while the minority carriers can flow freely; (c) a theoretical spin-valve configuration with non-magnetic metal electrodes; (d) a spin valve composed of a $[(C_5H_5)Co(C_5H_4\text{-}CCCH_2CH_2CC\text{-}C5H_4)Fe(C_5H_5)]$ molecular magnet and gold electrodes [23]

3.4.7. SUPERPARAMAGNETISM

When the magnitude of ferromagnetic material shrinks, surface energies (such as the domain wall energies) become progressively more costly in comparison with the volume energies (such as the demagnetising energy); there is a critical volume below which the creation of a domain structure is not preferred. The critical size of particle d_s can be defined as:

$$d_s = \frac{2\sqrt{J}}{M_s}, \tag{3-23}$$

where J is the exchange constant and M_s is the magnetic moment per unit volume. Typical values of d_s are 10–100 nm. Superparamagnetism is a size effect of ferromagnetism. Figure 3-22 shows the influence of magnetic particle size on its magnetic properties. The coercivity changes with the particle size–when it is small enough, the value of the coercive field becomes zero.

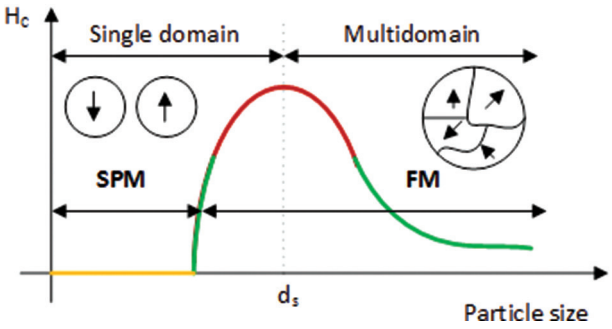

Figure 3-22. A schematic representation of the change of coercivity with the size of magnetic nanoparticles

At a sufficiently high temperature, the particles with size $d < d_s$ behave as a paramagnet. When the nanoparticles are small enough, the energy barriers for magnetisation reversal, which are proportional to grain volume ($\Delta E = KV$, where K is the anisotropy coefficient and V is the volume) are relatively low compared to thermal energy (k_BT, where k_B is the Boltzman constant and T is the temperature). With sufficient thermal energy, their magnetisation can flip direction randomly over short periods of time. The typical time between two flips is called the Néel relaxation time (τ_N), and is given by the Néel-Arrhenius equation:

$$\tau_N = \tau_0 \exp\left(\frac{KV}{k_BT}\right), \tag{3-24}$$

where τ_0 is the attempt time—a characteristic length of time of the material. It usually ranges from 10^{-9} to 10^{-12} s. In the absence of an external magnetic field, when the time used to measure the magnetisation of the nanoparticles (τ_m) is much longer than the Néel relaxation time ($\tau_m << \tau_N$), the magnetisation appears to be averaged to zero; they are then said to be in a superparamagnetic state. With the application of an external magnetic field, the nanoparticles are magnetised like paramagnets, but with much greater susceptibility.

One of the most important parameters describing superparamagnetic material is the blocking temperature (T_B), defined as:

$$\tau_N = \tau_0 \exp\left(\frac{KV}{k_B T}\right). \tag{3-25}$$

Blocking temperature is the temperature between the blocked and superparamagnetic states, or the temperature at which $\tau_m = \tau_N$. As shown in Figure 3-23, at temperatures below T_B—in the blocked state—the magnetic moment of each particle is well defined. Above the blocking temperature, the magnetisation constantly flips directions, resulting in an observed net moment of zero.

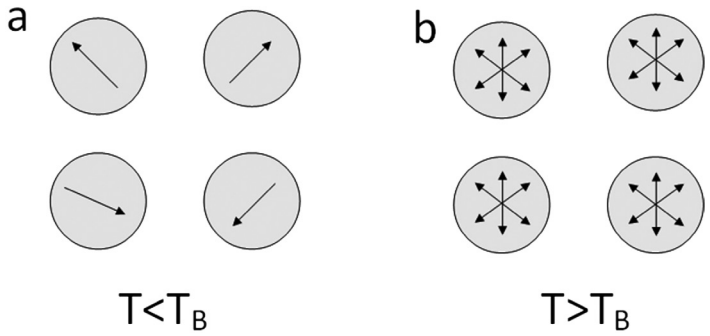

Figure 3-23. (a) When the temperature of the system is lower than the blocking temperature (T_B), the magnetic moment of each particle the magnetic moments of nanoparticles are blocked; (b) When the temperature of the system is higher than the blocking temperature, a superparamagnetic state is observed. In this state, the magnetisation constantly flips directions, resulting in an observed net moment of zero

The characteristic features of superparamagnetic material are:

– a lack of the hysteresis loop—the process of sample magnetisation and demagnetisation is reversible
– the shape of the magnetisation curve measured at various temperatures presented as a function of H/T does not change.

Figure 3-24 presents a comparison of M(H) dependencies observed for a ferromagnet, paramagnet, and superparamagnet below blocking temperature.

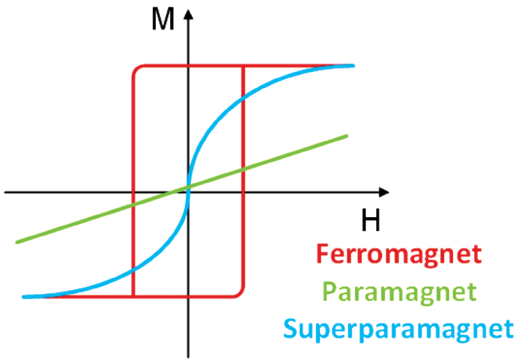

Figure 3-24. The magnetisation curves (plots of magnetisation M vs an applied field H) for paramagnetic, ferromagnetic, and superparamagnetic materials (when $T > T_B$; T_B is the blocking temperature) (own elaboration)

Taking into account the large magnetic moment of single domain particles, the dipole magnetic interaction can play a role in an interaction between nanoobjects. When the distance between particular particles is long enough, dipole–dipole interaction is weak and can only contribute to an increase of the energy barrier for spin reorientation. The situation is more complex when the distances between particles are very small (the particle concentration is high) and dipole–dipole interaction is significant, because at low temperatures a cooperative phase transition can occur. In a collection of chaotically orientated nanoparticles, the dipole– dipole interaction is frustrated and the system is similar to the spin glass. An example of superparamagnetic material is Fe_3O_4 nanoparticles about 5 nm in size. A characterisation of their magnetisation is shown in Figure 3-25.

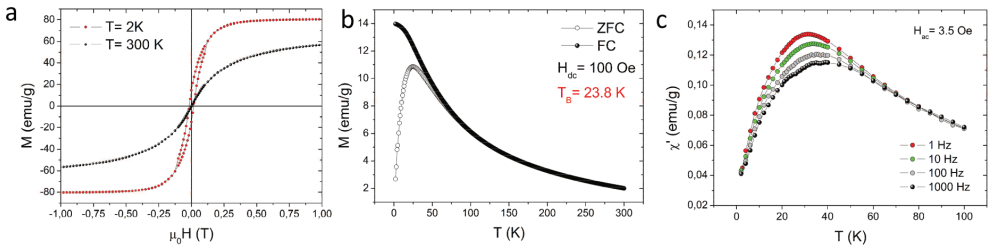

Figure 3-25. The magnetic properties of superparamagnetic nanoparticles of Fe_3O_4 (5 nm diameter): (a) hysteresis loops measured at 2 K and 300 K; (b) Zero-field-cooled (ZFC) and field-cooled (FC) magnetisation, where the blocking temperature is related to the maximum of the ZFC curve; and (c) the temperature dependence of the real component of AC susceptibility measured for various frequencies of an oscillating field (own elaboration)

Since many of the recording materials are particulate, the phenomenon of superparamagnetism is very important from a technological point of view. Magnetically recorded information is expected to be stored for years, so the minimum particle size is limited.

3.4.8. GEOMETRICALLY FRUSTRATED SYSTEMS: ARTIFICIAL SPIN ICE

Frustration—the presence of competing interactions—is a source of disorder, which can lead to new and interesting physical phenomena. The simplest example of a frustrated system is shown in Figure 3-26, which presents three magnetic moments interacting antiferromagnetically at the corners of a triangle. The minimum energy is achieved when each spin is aligned opposite to its neighbours. In the situation, when the first two spins align in an antiparallel orientation, the third one is frustrated because its two possible orientations, up and down, yield the same energy. The geometrical frustration of spins in a magnetic material gives rise to exotic low-temperature states such as 'spin ice'. In 'spin ice' the frustration of local magnetic moments is analogous to the frustration of hydrogen ion positions in frozen water.

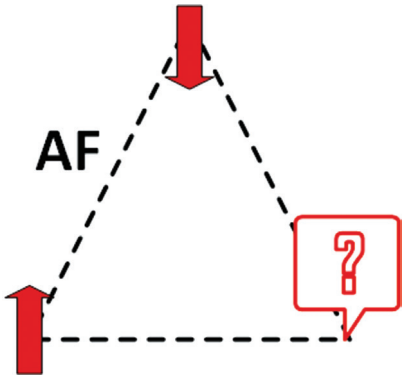

Figure 3-26. The simplest example of geometrical frustration—spins of neighbouring atoms tend to point in opposite directions, which creates ambiguity for the spin in the bottom-right corner as it cannot point in the opposite direction of both its nearest neighbours (own elaboration)

Another example of geometrically frustrated magnetic systems is spin ice [24]. Here, the frustration is observed in a ferromagnetically coupled system and results from very strong local magnetic anisotropy caused by the crystal field forcing the magnetic moments to point either in or out of a tetrahedron. The frustration in spin ice is a result of long-range magnetostatic dipole–dipole interaction, and not nearest-neighbour exchange coupling (Figure 3-27).

The first example of an artificial spin ice system was created in 2006 [25]. It is a geometrically frustrated magnet based on an array of lithographically fabricated single-domain ferromagnetic islands. The magnetic moment of each nano-island behaves as a macrospin orientated along its principal axis, giving a binary degree of freedom. The interactions of these islands results in an appearance of collective behaviour which depends on their geometrical arrangement. It is possible to design exotic states in their low-energy physics. The islands are arranged such that the dipole

interactions create a two-dimensional analogue to spin ice. The local accommodation of frustration can be studied based on MFM images of the magnetic moments of particular elements in this correlated system (Figure 3-28).

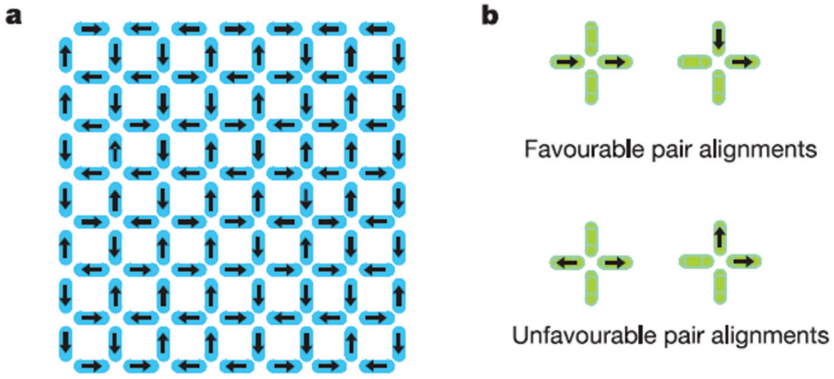

Figure 3-27. (a) Illustration of square artificial spin ice, where each nano-island is a single-domain ferromagnet. Arrows indicate the orientation of its island's magnetic moment in their vertex ground state; (b) energetically favourable and unfavourable dipole interactions between the pairs of magnetic moments [25]

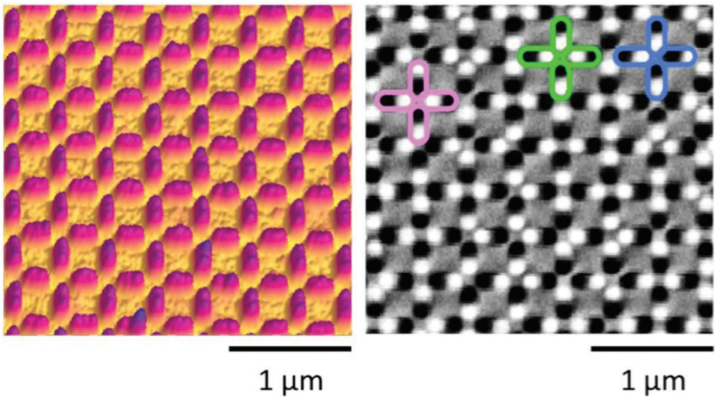

Figure 3-28. Artificial spin ice in (a) an AFM image of a typical permalloy array with a lattice spacing of 400 nm and (b) an MFM image taken from the same array. The various types of vertices are highlighted by coloured outlines [25]

4. EXPERIMENTAL TECHNIQUES

4.1. SCANNING PROBE MICROSCOPES

4.1.1. SCANNING TUNNELLING MICROSCOPE (STM)

A scanning tunnelling microscope (STM) allows the surface image of conductive materials to be observed at a resolution of a single atom. The basic components of an STM are the scanning tip, piezoelectrically controlled height and x, y scanner, coarse sample-to-tip control, and a vibration isolation system (Figure 4-1).

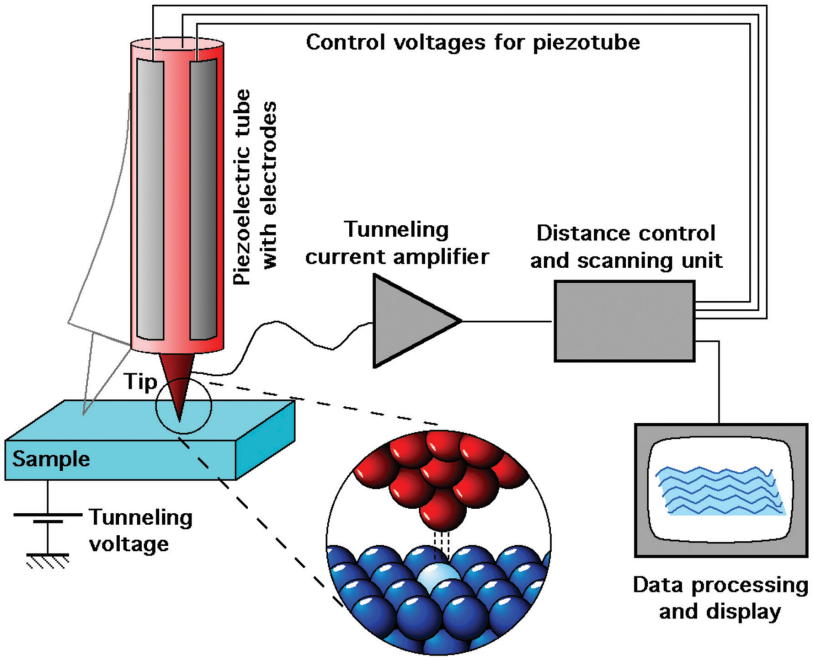

Figure 4-1. An illustration of a STM [26]

STMs are based on the concept of quantum tunnelling. Local measurement of the electron states of a sample's surface is accomplished through the use of electron tunnelling. The scanning tip, usually made of tungsten or platinum-iridium, is placed

above the surface of the conductive sample and moves in a controlled way. When the distance between the probe and the sample surface is 1 nm, electron tunnelling begins (Figure 4-2). A difference in potential is created between the tip and the sample due to an applied voltage bias. The tunnelling current is an exponential function of distance. Based on quantum mechanics, the tunnelling current (I_t) can be expressed as:

$$I_t = e^{-k_B d} \tag{4-1}$$

where d is the distance between the tip and the surface of the sample and k_B is Boltzmann's constant.

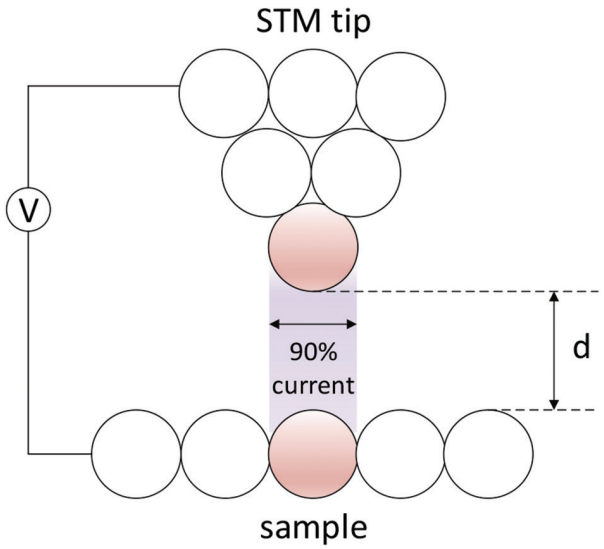

Figure 4-2. A basic overview of the STM tip–sample interaction. When the distance between the tip and the sample is reduced to a few atoms, the application of a voltage V brings about a current between the tip and the sample (own elaboration)

This measurement technique presents some challenges. The image quality may be affected by hysteresis or an aging scanner. Local changes in the conductivity of the sample may affect the accuracy of the surface image. The main disadvantage of STMs is their considerable sensitivity to external vibrations, which in modern microscopes is limited by the use of vibration dampening systems. They allow the surface and atomic structure of samples with good conductive properties to be studied. An analysis of a non-conductive material is only possible after covering the sample with a conductive layer. STMs allow us to determine the local density of electrons. They also help in understanding the phenomena occurring on the surface of a sample (adhesion or friction) and many biological phenomena. If the voltage of the tunnelling current is increased above the nominal value used for scanning, it is possible to extract individual atoms from the surface.

There are two main operation modes of an STM:

- Constant-current mode, where the tip moves across the surface of the sample while voltage and current are kept constant. The constant value of the tunnelling current is achieved by adjusting the height of the scanner at each measurement point; therefore, constant current means a constant distance between the tip and the scanned surface. Using constant-current mode, it is possible to measure irregular surfaces with the precision of a few hundredths of an angstrom, though the measurement is very time-consuming.
- Constant-height mode, where the tip moves in a horizontal plane above the sample and the tunnelling current varies depending on the topography and local surface electronic properties of the sample. The topographical image is created by measuring the tunnelling current at each point on the sample surface. This operation mode is mainly applied for relatively smooth surfaces and its advantage is the short measurement time.

A comparison of constant-height or constant-current mode is presented in Figure 4-3.

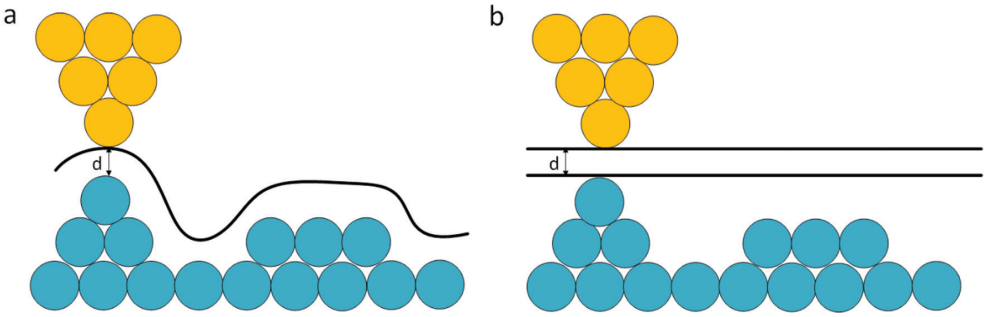

Figure 4-3. A schematic representation of a scanning tunnelling microscope operating in (a) constant current mode and (b) constant height mode (own elaboration)

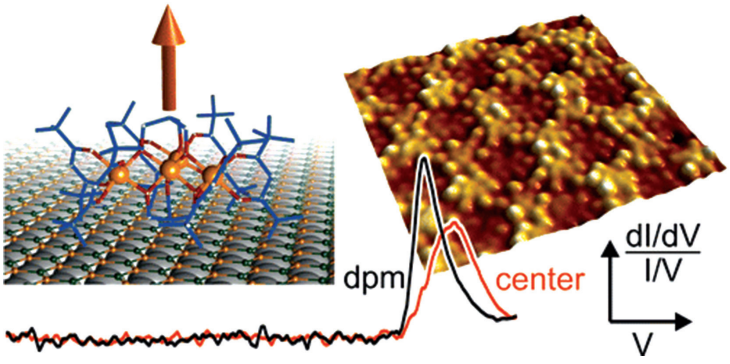

Figure 4-4. A representation of an Fe4 single-molecule magnet deposited on a solid support [27]

The STM technique is very helpful in the investigation of self-assembly monolayers, e.g. well-defined monolayers or spatially isolated single molecule magnets (SMMs) deposited on a solid substrate. In Figure 4-4 one can see self-organised arrays of Fe4 SMMs on hexagonal boron nitride (h-BN) on Rh(111) as a template [27]. A high-resolution, low-temperature STM was used to confirm successful Fe4 molecule adsorption on the substrate. Furthermore, experimental STM images of an individual Fe4 molecule were compared to the results obtained from density functional theory (DFT) calculations, which showed excellent agreement with the data (Figure 4-5).

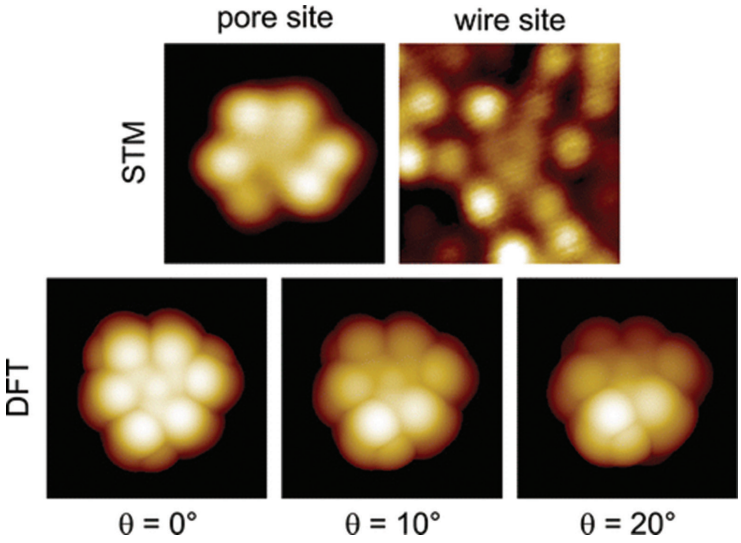

Figure 4-5. The top row presents the experimental STM images of an individual Fe4H single molecule magnet on a pore site and of an Fe4H single molecule magnet embedded in an island on a wire site. The bottom row shows simulated (DFT) STM images of Fe4H determined from the density of states [27]

4.1.2. SPIN-POLARISED SCANNING TUNNELLING MICROSCOPE (SP-STM)

A spin-polarised scanning tunnelling microscope (SP-STM) is a specialised application of an STM. In addition to providing information about the atomic topography, an SP-STM provides detailed information about the magnetic phenomena on an atomic scale. To distinguish between electrons with different spin alignments in magnetic solids, the probe tip needs to be coated with a thin film of magnetic material. An SP-STM image is created based on the difference in tunnelling conductance for parallel or antiparallel alignment of the spins between the tip and the substrate. A schematic illustration of the imaging of a 2D magnetic material with an SP-STM is presented in Figure 4-6.

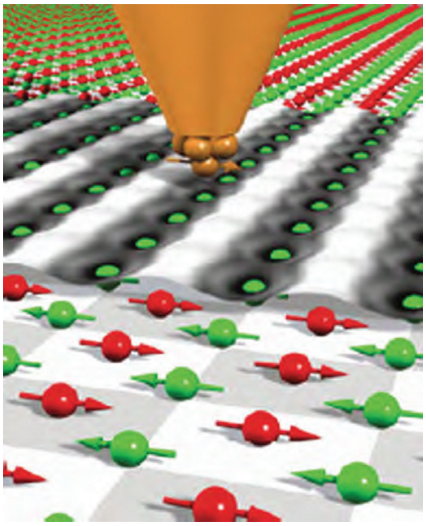

Figure 4-6. The imaging of a 2D antiferromagnet with a magnetically coated probe tip with a well-defined spin state. The changes the tunnelling current are associated to the relative orientation of the spins in the tip and the sample, which makes the observation of the antiferromagnetic structure possible at the atomic level [28]

4.1.3. ATOMIC FORCE MICROSCOPE (AFM)

An Atomic Force Microscope (AFM) is the most powerful microscopy technology for studying samples at the nanoscale. An AFM microscope can obtain a surface image with a resolution of a single atom. A schematic of the device is shown in Figure 4-7.

The main component of an AFM microscope is a tip fixed at the end of a cantilever 100–200 μm in length. The AFM tip interacts with the substrate through a raster scanning motion. The movement of the tip is monitored with a laser beam reflected off the cantilever. This reflected laser beam is tracked by a position-sensitive photo-detector that registers the vertical and lateral motion of the probe.

In an AFM, short- or long-range forces can be used to visualise the surface of a sample, so the measurement modes are distinguished by the type of force:

- Contact mode, in which the AFM tip plays the role of a profilometer examining the topography of the surface. The pressure of the tip on the surface is between 10^{-7} N to 10^{-11} N; therefore, the contact area between the tip and the surface of the sample is extremely small. In this mode, short-range interatomic interactions are used. There are direct interactions between the electron spheres of the atoms of the tip and the atoms of the sample, and the repulsive forces acting on the tip bring about the deflection of the cantilever.
- Non-contact mode, in which the tip hovers 10–100 Å above the sample's surface, so the long-range forces acting between the tip and the sample are of primary importance. In this mode, we do not measure the static deflection of

the lever, but the lever is set to vibrate at a frequency close to its resonance. The reaction to the force acting on the lever is a change in the amplitude and frequency of the vibrations, which carries the information that is converted later into an image.

- Tapping mode, in which the cantilever is driven to oscillate up and down near its resonance frequency. In this mode, when the tip comes close to the surface the long-range forces acting on the cantilever result in a change of the amplitude of the cantilever's oscillation and the tip touches the sample. An AFM image obtained in tapping mode represents the force of the intermittent contact of the tip with the sample's surface.

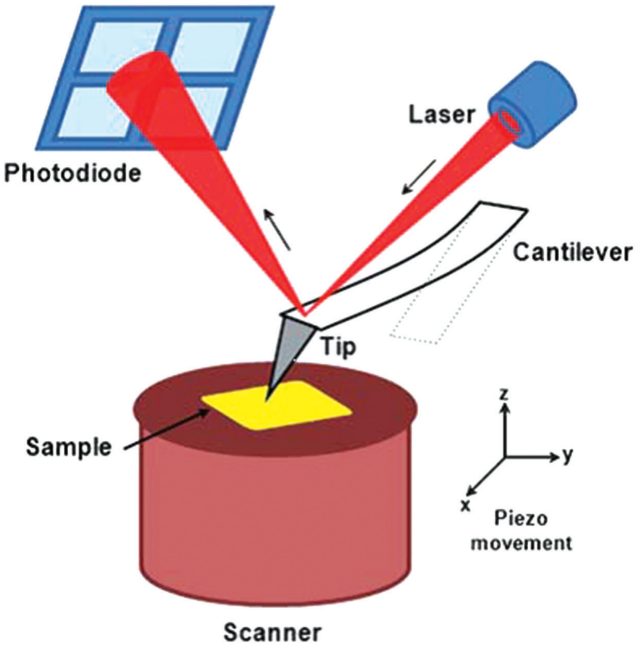

Figure 4-7. An AFM, where the main components are the cantilever, with the tip at its end, the sample mounted on top of a piezoscanner, and the optical system for the detection of cantilever deflection [29]

One of the most important parameters obtained from AFM images is the surface roughness. *Root Mean Square* (RMS) roughness can be defined by the equation:

$$R_q = \sqrt{\frac{1}{n}\sum_{i=1}^{n}\left(y_i - \bar{y}\right)^2}, \tag{4-2}$$

where n is the counts number, y_i is the height of the object, and is the average height of the objects of the scanned surface. Examples of data recorded in tapping mode are presented in Figure 4-8.

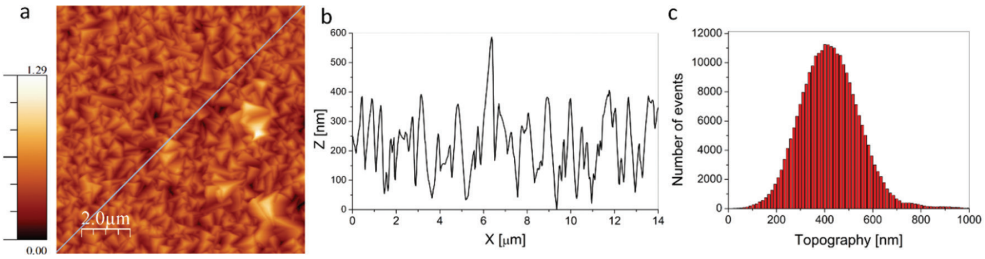

Figure 4-8. A 100-mm^2 topography AFM image obtained in tapping mode of a film of $Fe_3[Cr(CN)_6]_2 \cdot 15H_2O$ with a thickness of 1450 nm; (b) the height profiles of the $Fe_3[Cr(CN)_6]_2 \cdot 15H_2O$ thin film across the diagonal of 2D height images; and (c) the particle size distribution calculated from the 2D height images presented in (a) (own elaboration)

4.2. ELECTRON MICROSCOPY: TRANSMISSION ELECTRON MICROSCOPE (TEM) AND SCANNING ELECTRON MICROSCOPE (SEM)

The methods of creating an enlarged image in both optical and electron microscopy are based on similar principles. In the latter, visible light is replaced by a beam of electrons accelerated by an electrical field, and optical lenses by electromagnetic lenses.

The most important element of an electron microscope is the microscope column and its electron gun, which produces an electron beam. The pre-formed electron beam is accelerated between the cathode and the anode to obtain the energy:

$$E = eU, \tag{4-3}$$

where e is the charge of the electron, and U is the voltage between the cathode and the anode.

Increasing the voltage causes an increase in the electrons' momentum, which reduces the wavelength. The electron beam is manipulated by a magnetic field. The magnetic fields form a magnetic lens of variable focussing power. An important advantage of magnetic lenses is the ability to smoothly change their focal lengths by adjusting the current passing through the lens. In TEMs, electrons pass through the examined specimen, meaning the sample cannot be thicker than 0.1 μm.

In the SEMs, the electron beam is passed across the surface of the sample, and secondary and backscattered electrons are created as a result of reflection off the sample. Because the emission of electrons from a sample depends on the shape of its surface, it is possible to obtain a topographic image of the sample. Secondary electrons arise as a result of inelastic interactions with the surface. At low energies (below 50 eV), emission occurs from the near-surface area of the sample. The contrast is related to the topography of the sample due to the fact that the edges and walls emit more secondary electrons. Thus, these areas are characterised by greater clarity than others.

The most valuable effect of the electron beam's interaction with the sample is the emission of a characteristic radiation spectrum for each element. By analysing the measured radiation spectrum, one can assess the amount, type, and distribution of elements on the scanned surface of the sample. A burst of high-energy electrons hitting the surface of the sample causes the atoms to be excited and characteristic X-rays to be emitted. This radiation is collected by the detector, and the number of quanta of radiation with the same energy is recorded. The amount of a given element in the sample is proportional to the count of characteristic quanta, so it can be determined by calculating the peak area in an energy histogram. This experimental technique is called energy-dispersive X-ray spectroscopy (EDS).

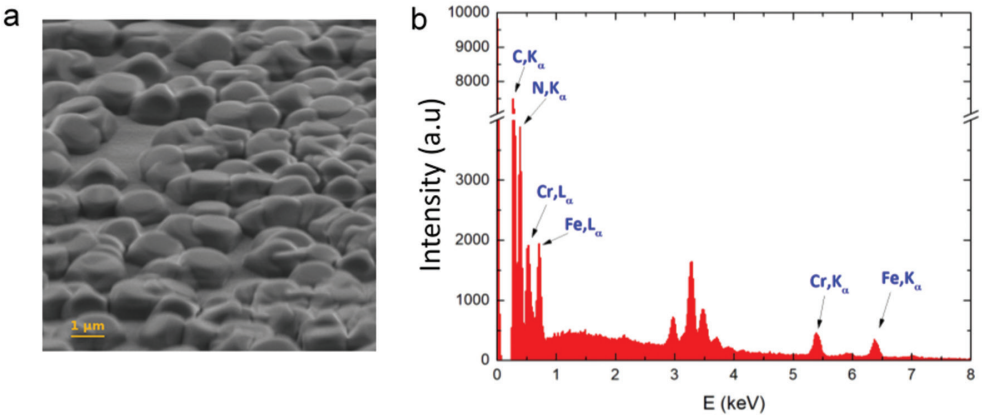

Figure 4-9. SEM image and EDS histogram of an $Fe_3[Cr(CN)_6]_2 \cdot 15H_2O$ thin film deposited onto a PET/ITO substrate (own elaboration)

4.3. MAGNETO-OPTIC KERR EFFECT (MOKE)

The magneto-optic Kerr effect (MOKE) describes the changes to light reflected from a magnetised surface. This phenomenon was observed by John Kerr in 1887 [30]. It is similar to the phenomenon observed by Faraday in 1845, wherein linearly polarised light rotates after passing through a magnetic material in the presence of an external magnetic field (Figure 4-10). The MOKE signal is proportional to the magnetisation of the examined material, so it can be used to analyse the magnetic properties of various substances. Currently, the MOKE's high sensitivity means that its largest application is in the study of multilayer systems and thin films, shown by its ability to record signals even for monolayers.

A linearly polarised laser beam reflected off a magnetic sample separates into two components. The first component is in phase with the incident beam and is responsible for rotating the plane of light polarisation (Kerr rotation). The second component of

the reflected beam is out of phase with the incident beam and is referred to as the Kerr ellipticity. The observed effect strongly depends on the polarisation of the electrons responsible for magnetism. The twisting of the polarisation plane is proportional to the magnetisation.

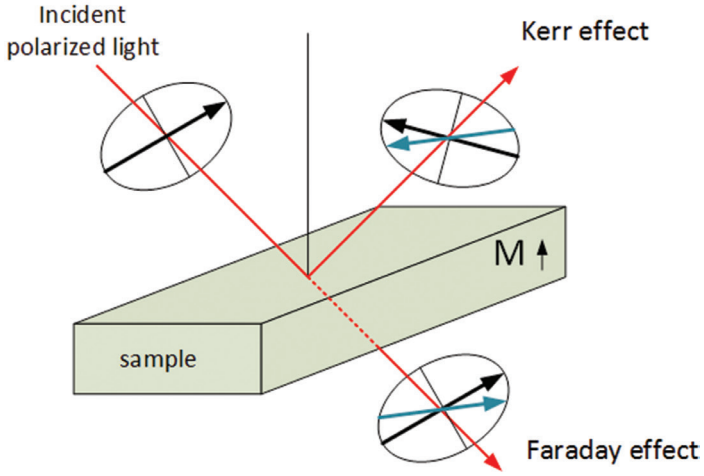

Figure 4-10. The Kerr/Faraday effect (own elaboration)

A quantum explanation of the Kerr effect was proposed in 1932 by Hulme, who showed that the dielectric constant is a consequence of the spin-orbit coupling that connects the spin of the electron to its orbital motion. The change of electron states affects the polarisation and ellipticity of the light. The optical properties of the medium are described by the dielectric tensor ε, which is determined by the electron motion of the medium. Magneto-optical effects (the Faraday effect and the Kerr effect) are related to the fact that the electron response to left and right circularly polarised light differ.

There are three configurations of the Kerr magneto-optical effect, depending on the direction of the magnetisation vector in relation to the surface of the sample and the plane of incidence of the laser beam. These configurations are illustrated in Figure 4-11.

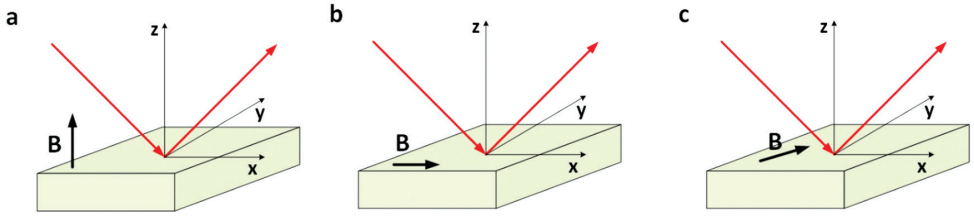

Figure 4-11. Kerr effect geometries: (a) polar, (b) longitudinal, and (c) transversal (own elaboration)

In the polar configuration, the magnetisation vector is perpendicular to the surface of the sample. This MOKE geometry allows us to study systems with perpendicular anisotropy. In the longitudinal configuration, the magnetisation vector lies in the surface plane of the sample and is parallel to the plane of the incidence of light. This geometry is most often used for systems showing in-plane magnetic anisotropy. In the case of perpendicularly magnetised systems, the longitudinal MOKE can also help determine the values of the anisotropy fields. The third geometry is the transversal, where the magnetisation vector is perpendicular to the plane of reflection of the laser beam. This configuration differs from the two presented above, in which the noticeable effect is observed only when the incident beam is polarised parallel to the direction of incidence. One application of transverse geometry may be a detailed analysis of the re-magnetisation process. A typical setup of a MOKE apparatus is shown in Figure 4-12.

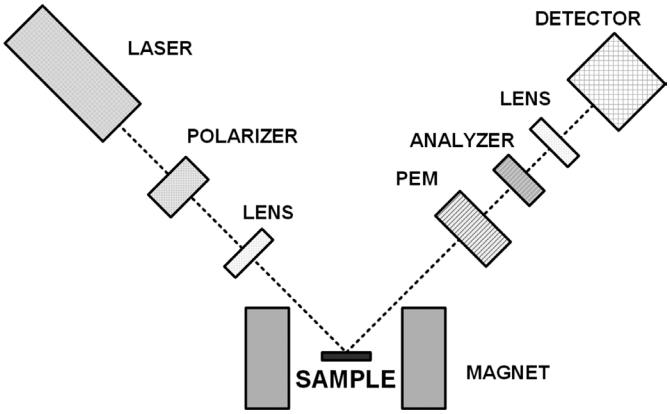

Figure 4-12. An experimental MOKE setup (own elaboration)

The light source used in a MOKE set-up is a semiconductor laser which gives off almost monochromatic light in a well-focussed beam. The monochromaticity of the light is important because the reflection coefficients depend on the wavelength λ. The laser light is polarised using a prismatic polariser. To adjust the polarisation plane, the polariser is located in the housing, and is rotated about the axis parallel to the direction of the beam propagation. After reflecting from the surface of the sample, the light goes to the analyser, a Wollaston prism. At this stage, the two orthogonal components of the light's intensity, I_1 and I_2, are separated and directed into two different photodiodes. In this step the detection system calculates the sum $(I_1 + I_2)$ and the differences $(I_1 - I_2)$ of the individual components of the light intensity vector. Since the sum $(I_1 + I_2)$ is proportional to the Kerr rotation θk, and θk is furthermore proportional to the magnetisation of the sample, the output signal is interpreted as the dependence of magnetisation (M) on the external magnetic field (H) produced by the electromagnets.

The MOKE is a simple and popular research tool which can be applied to different types of magnetic thin films. As an example, we present MOKE measurements performed for electrochemically deposited $Cr_3[Cr(CN)_6]_2$ films (Figure 4-13) [31]. Based on MOKE measurements a strong correlation between the roughness of the surface of these samples and the values of the coercive field was observed. This fact indicates a particle size effect, which has been also observed in other molecule-based materials. The increase in the coercive fields with decreasing film thickness is correlated with a simultaneous decrease in the size of the particles and the roughness of the film surface. Thinner films show more coercivity and squareness in their hysteresis. The reduction of squareness indicates that thicker films may involve a broader, less uniform size distribution of crystallites than thinner films, perhaps with a larger concentration of impurities. The light reflected from the thickest film shows a significant depolarisation due to the multiple reflections from the non-uniform layer thickness.

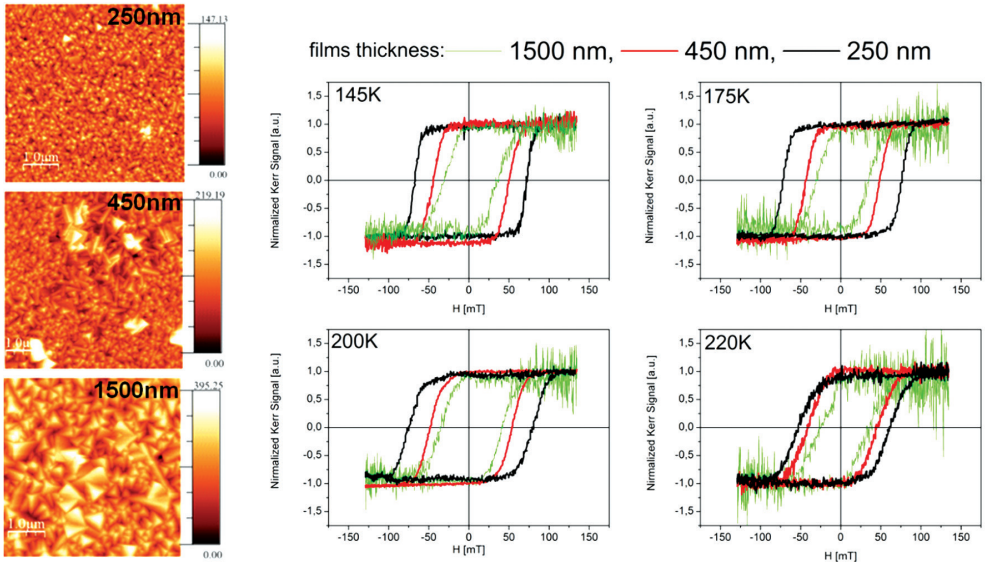

Figure 4-13. AFM topography images of the surface of $Cr_3[Cr(CN)_6]_2$ thin films of different thicknesses (left side) and normalised MOKE hysteresis loops obtained for these films in polar configuration (right side) (own elaboration)

The measurement of magnetic hysteresis was also possible for $Ni_{1.5}[Fe(CN)_6]_x[Cr(CN)_6]_{1-x}\cdot nH_2O$ (x = 1 and 0.55) thin films fabricated using 'layer by layer' deposition. The evolution of the coercive field was monitored while heating the system. For both compounds the increased temperature brings about a decrease in the coercive field (Figure 4-14). From the linear extrapolation of $H_c(T)$ dependence, the critical temperature is equal to 22 K for $Ni_{1.5}[Fe(CN)_6]\cdot nH_2O$ and 48 K for $Ni_{1.5}[Fe(CN)_6]_{0.55}[Cr(CN)_6]_{0.45}\cdot nH_2O$. These values are consistent with those obtained

from traditional magnetic measurements performed by SQUIDMPMS magnetometer. The very good agreement of critical temperatures obtained by SQUID and MOKE measurements indicates that these films are not contaminated by any magnetic species, such as oxides.

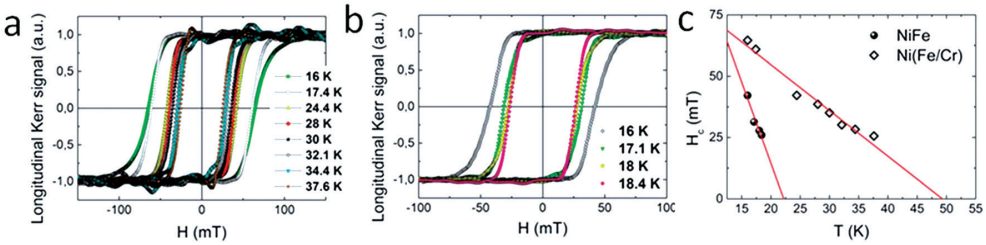

Figure 4-14. Normalised MOKE hysteresis loops obtained in the polar configuration at various temperatures for samples of (a) $Ni_{1.5}[Fe(CN)_6]$ and (b) $Ni_{1.5}[Fe(CN)_6]_{0.55}[Cr(CN)_6]_{0.45}\cdot nH_2O$; (c) a comparison of the temperature dependence of coercive fields recorded for the $Ni_{1.5}[Fe(CN)_6]$ and $Ni_{1.5}[Fe(CN)_6]_{0.55}[Cr(CN)_6]_{0.45}\cdot nH_2O$ samples [32]

A powerful tool used today to observe magnetic domains is a Kerr microscope, which relies on the MOKE. The Kerr microscope is an extension of a polarisation contrast microscope and can probe the local magnetic properties of ferromagnetic specimens. In a Kerr microscope, the incident light is first passed through a polarising filter. Then it is reflected off the sample and passed through an analyser, before going through a regular optical microscope. Similarly to a traditional MOKE setup, the reflection of polarised light from the sample surface, a change in Kerr rotation, Kerr ellipticity, or polarised amplitude occur. The analyser converts the changes in the polarisation into changes in light intensity, which are then recorded. A computer system is often used to create an image of the magnetic field on the surface from these changes in polarisation.

4.4. THICKNESS CONTROL

The thickness of the deposited films is usually controlled by quartz crystal monitors with basic resonant frequencies in the range of 1–30 MHz. Each crystal acts as an oscillator, whose resonant frequency is controlled by a frequency counter with an accuracy of 1 Hz or better. The crystals are placed in the vicinity of the substrate and during deposition the evaporated material condenses on both the sample and the crystal. This causes a change in its resonant frequency, which can be converted into deposited layer thickness by using the simplified Sauerbrey equation [33]:

$$d = C\,\Delta f, \tag{4-4}$$

where d is the film thickness, C is the sensitivity coefficient depending on the deposited element, and $\Delta f = f_s - f_e$ is the observed resonant frequency change, where f_s and f_e are the resonant frequencies of quartz crystal at the start and at the end of layer deposition, respectively.

The sensitivity coefficient for each element is determined before each series of sample deposition through a calibration procedure utilising *in situ* reflection high-energy electron diffraction (RHEED) or *ex-situ* x-ray reflectometry to determine the thickness of the film. Knowing the change in resonant frequency of the quartz crystals and the thickness of the calibration sample, the sensitivity coefficient can be determined using the above-mentioned relationship. To make sure that the sensitivity coefficient is correctly set, the entire calibration procedure can be repeated. This calibration method provides a measurement of film thickness that is accurate to approximately 1%–5%.

When the above-described calibration is not possible, the thickness of deposited films can be approximately determined using the following relationship:

$$d_f = \frac{N_q \rho_q}{\rho_f f^2}\left(f - f_q\right), \tag{4-5}$$

where N_q is the material constant for quartz ($1.668 \cdot 10^5$ Hz·cm), f is the basic resonant frequency for pure quartz, f_q is the frequency of the quartz oscillator at the end of film deposition, ρ_q is the density of quartz, ρ_f is the density of the deposited material, and d_f is the film thickness.

4.4.1. X-RAY REFLECTOMETRY (XRR)

X-ray reflectometry (XRR) is a non-destructive analytical technique used to characterise surfaces, coatings, and thin film interfaces. The method provides structural information on thin films concerning the thickness, density, and roughness of all layers in the system. It involves monitoring the intensity of x-rays reflected from the sample as a function of the incidence angle at grazing angles.

As shown in Figure 4-15, a monochromatic x-ray beam irradiates the sample at a grazing angle ω, while the reflected intensity is recorded at an angle 2θ. The entire measurement is carried out in the specular reflection regime, which fulfils the relationship $\omega = 2\theta/2$.

The beam optics in XRR measurements can be very diverse and depend on the type of diffractometer, as well as the requirements of the research. In the example shown in Figure 4-16, an X-ray tube is followed by a thin Ni filter used to cut off a Cu K_β line. Then, divergence slits and Soller parallel plate collimators reduce the divergence of the beam. The cross-section of the beam is limited by aperture slits and a mask placed at the end of the incident beam's path. After interacting with the sample, the reflected beam is formed by a Soller parallel plate collimator and collimator slits, and is then collected by a counter.

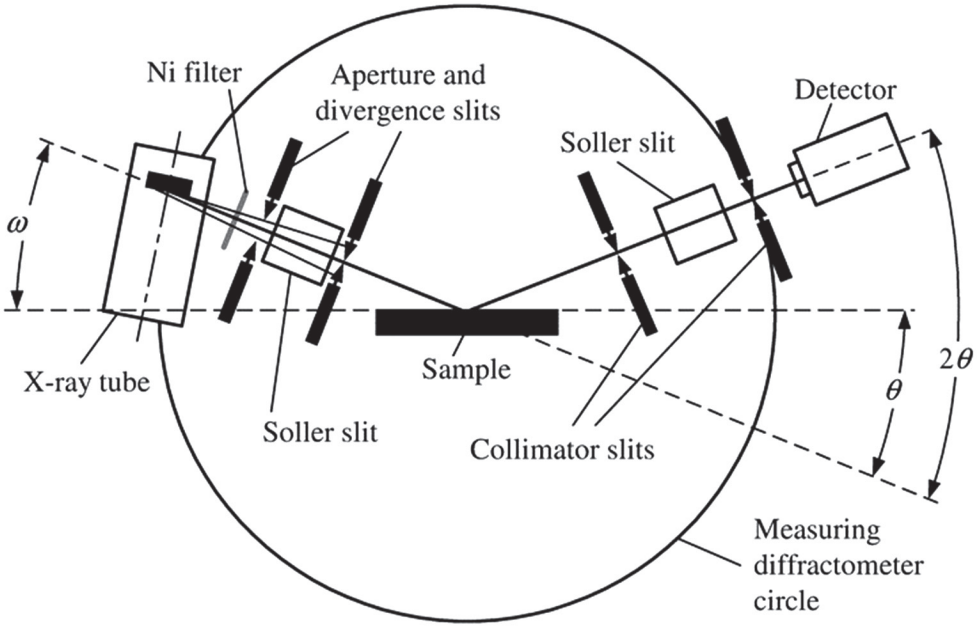

Figure 4-15. Example measurement set-up for x-ray reflectometry [34]

For incident angles θ below a critical angle θ_c, the total external reflection occurs because the value of refraction index for X-rays is slightly smaller than 1 in most materials. It is observed as a plateau in the XRR curve as presented in Figure 4-16. By applying Snell's law and the small angle approximation, the critical angle θ_c can be expressed as:

$$\theta_C = \lambda \sqrt{\frac{N_A r_0 (Z + f')}{\pi A}} \rho, \tag{4-6}$$

where λ is the X-ray beam wavelength, N_A is the Avogadro constant, r_0 is the radius of an electron, A is the atomic weight, Z is the atomic number, f' is the dispersion correction coefficient, and ρ is the density of the material. If the critical angle is known, the mean density of the material can be determined. The θ_c angle is marked in the reflectivity curve as an abrupt fall in the reflected intensity (see Figure 4-16) and can be determined experimentally from the drop in intensity down to half of the maximum value for the total external reflection [35].

For incident angles θ greater than θ_c, the X-ray beam penetrates the film. Reflection occurs at the top and at the bottom surfaces of the constituent layers due to the differences in the electron densities, which correspond to a variation in refractive indices. The interference between the beam reflected from the substrate and the outermost surface of the system results in interference fringes called Kiessig fringes, while the interference between the rays reflected from the interfaces of the

component layers forms Bragg peaks. Thus, the period of the Kiessig fringes is related to the total thickness of the system and for angles much larger than the critical angle, the thickness can be calculated as:

$$D \approx \frac{\lambda}{2\left(\theta_{m+1} - \theta_m\right)}, \tag{4-7}$$

where $\theta_{m+1} - \theta_m$ is the difference between the angular position of two neighbouring Kiessig maxima or minima and λ is the X-ray beam wavelength. For XRR curves exhibiting interference fringes in a wide angular range, the thickness can be determined with a precision exceeding 1 Å.

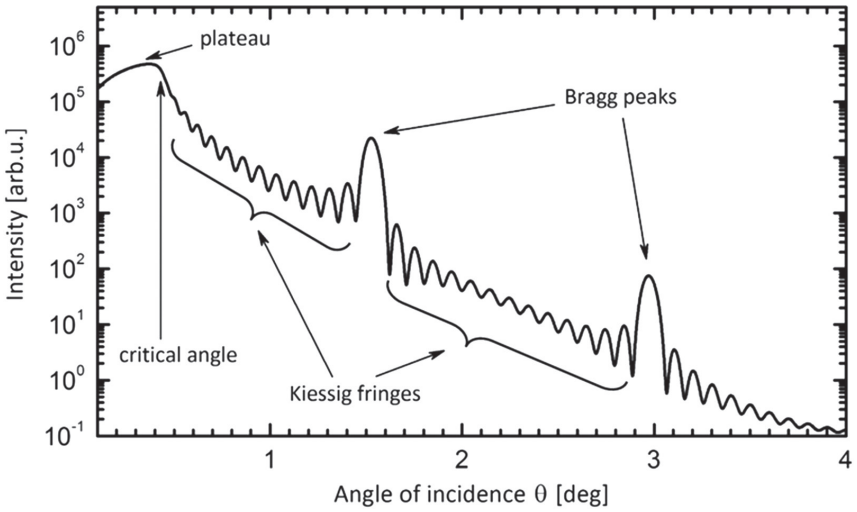

Figure 4-16. An example of the simulated reflectometry curve for a SiO_2/[Fe(1nm)/Pd(2nm)]x15 multilayer [36]

Another important quantity determined from XRR measurements is the surface and interface roughness. This gives rise to diffuse scattering, resulting in a lower intensity in the specularly reflected beam. Roughness damps the intensity of the X-rays that reach the detector, and this intensity is indirectly proportional to the value of θ. This limits the angular range of an XRR pattern.

4.5. AUGER ELECTRON SPECTROSCOPY (AES)

Auger electron spectroscopy (AES) is one of the most popular methods of chemical surface analysis. The main advantages of this technique are its high sensitivity, the ability to probe only a thin surface layer (5–20 Å), easy interpretation of the collected spectra, and the ability to analyse all elements apart from hydrogen and helium.

The technique is based on the Auger process, which is illustrated in Figure 4-17. It is initiated by an incident electron or proton with energy in the range of 1–50 keV, which removes an electron from the core state of an atom. The hole in the inner electron shell with energy E_1 is then filled by an electron from the outer shell with energy E_2. However, the difference between these energies is not emitted in the form of a photon, but is instead transmitted to another electron located at the outer shell with energy E_3. This electron, called the Auger electron, is ejected from the atom. Its energy depends on the energy levels of the atom, so it is characteristic for a given element. Therefore, chemical composition analysis can be performed by measuring the energy spectrum of electrons emitted from a sample. It is worth noting that three electrons participate in each Auger process, so it does not occur for hydrogen and helium.

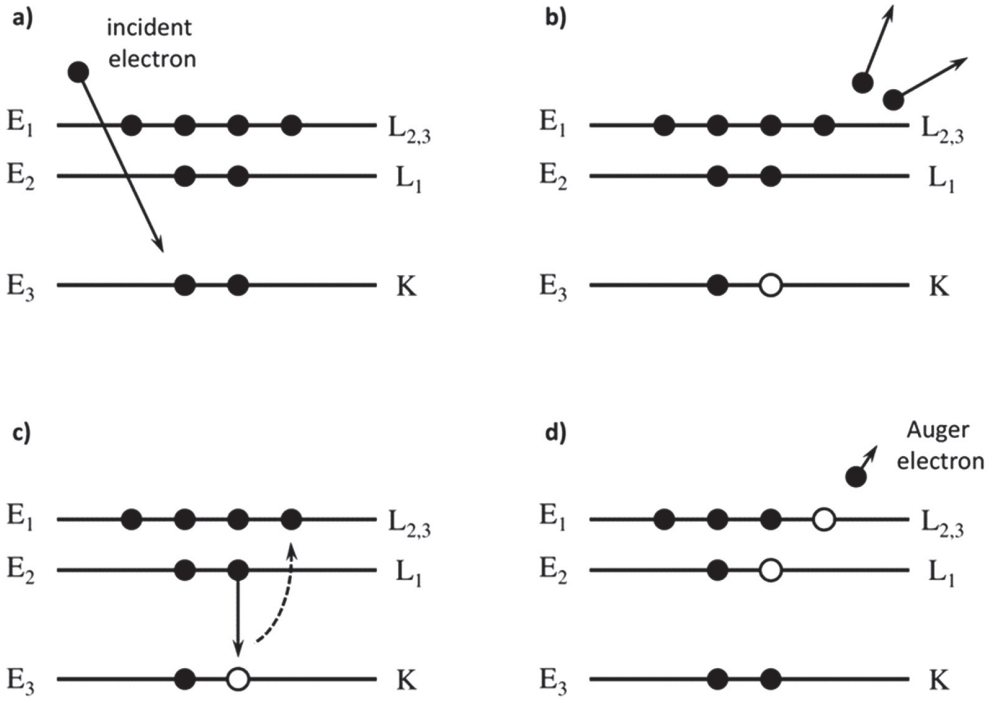

Figure 4-17. The Auger process: (a) an incident electron interacts with an atom and (b) creates a core hole in the K level; (c) an electron from the L_1 level fills in the K hole and the transition energy is transmitted to an L_2 electron; (d) an electron from the L_2 level is emitted as an Auger electron. The final atomic state has two holes, one in the L_1 level and the other in the L_2 level (own elaboration)

The kinetic energy of the Auger electron can be expressed by the simple formula:

$$E_{kin} = E_2 - E_1 + E_3 \tag{4-8}$$

The incident electron beam needed to knock the electrons from the inner shell usually carries energy in the range of 1–50 keV. The beam intensity is selected based

on the research needs and the material under study, and is typically of the order of tens of μA. Depending on the energy of the incident electrons and the material density, electrons from the primary beam penetrate into the sample to a depth of 1–2 μm. However, Auger electrons only reach the detector from a small subsurface layer, due to the large inelastic scattering.

An Auger electron spectrum can be registered using a few different types of analysers. One of the most popular is the retarding field analyser, which is schematically depicted in Figure 4-18. It consists of hemispherical conducting grids to which a voltage is applied. The grids with the smallest radius retard electrons emitted from the sample and an electron is able to pass through them only if its energy is greater than eU. If there is less energy, it will not reach the grid at all. The energy spectrum of the electrons emitted from the sample can be recorded by measuring the changes in the charge collected by the grids as a function of the voltage applied between them.

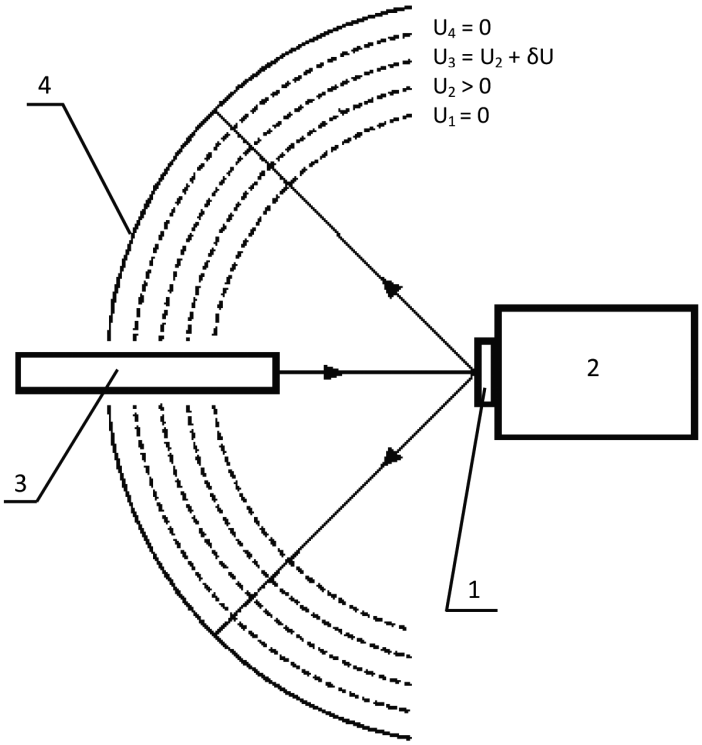

Figure 4-18. A retarding field analyser: 1 – the sample; 2 – the sample holder; 3 – the primary electron gun; and 4 – the screen. Hemispherical grids are marked as dashed lines (own elaboration)

The intensity of the peaks in an Auger spectrum is often small and the peaks are difficult to distinguish from the background, which makes them difficult to identify.

Therefore, electronic circuits are used to differentiate the spectrum in order to obtain sharper peaks. It is assumed that the location of the minimum of the derivative peak determines the energy of the Auger electrons. Exemplary derivatives of Auger spectra for the low-energy range are shown in Figure 4-19. They were collected for thin multilayers containing Co, Cu, and Pb. Details of the spectra will be discussed below, but here we would like to draw attention to the characteristic 'undulating' shape of each signal originating from Auger electrons, which is the result of a differentiation operation.

Auger spectra are usually recorded in the energy range of 10 eV to 5 keV, although from a surface physics point of view the low-energy range up to 200 eV is the most interesting. For such energies, the mean free path of the Auger electrons in the material is the shortest. The mean free path is defined as the average path of free propagation of an electron before inelastic scattering; it depends mainly on the energy of the electrons emitted from the sample. It can be estimated from the phenomenological formula

$$\lambda_e = \frac{1430}{E^2} + 0.54\sqrt{E}, \tag{4-9}$$

where energy is expressed in electronvolts. Direct measurements indicate that for a cobalt line of 57 eV and a copper line of 66 eV it is 0.44 nm and 0.56 nm, respectively. This means that Auger electrons with such low energies can only reach the detector from a thin surface layer. Taking into account that a cobalt and copper monolayer has a thickness of about 0.2 nm, an Auger spectrum provides information about only a few monolayers of the material. It is worth noting that the Auger process also takes place deeper within a larger sample volume, but only those electrons that were formed within a few angstroms of the surface can escape from the sample without energy loss.

The Auger spectrum allows the concentration of elements in the thin surface layer of the sample to be determined. However, in order to find the relationship between the intensity of the peaks and the concentration of an element, we should consider the influence of several factors on the measured signal. These factors include the energy of incident electrons, cross-section for atom ionisation process, and the probability of the Auger process for a given element. All the above factors are assembled into one parameter, called the sensitivity factor S_x. It is a dimensionless number, measured individually for each element. A list of sensitivity coefficients is available in [37]. The value of coefficients may depend slightly on the type of spectrometer, and a list of them is usually provided by the manufacturer in the technical specifications. For example, for an AES spectrometer produced by OCI Vacuum Microengineering, Inc. with an incident electron energy of 3 keV, the sensitivity factors are 0.807 for cobalt, 0.735 for copper, and 1.16 for lead.

The concentration of element x in a sample can be expressed as:

$$C_x = \frac{I_x}{S_x \cdot d_x} / \sum_{\alpha} \frac{I_\alpha}{S_\alpha \cdot d_\alpha}, \tag{4-10}$$

where I is the Auger derivative peak-to-peak amplitude, S is the sensitivity factor, and d is the relative scale factor. The summation is carried out for all α elements whose peaks are present in the Auger spectrum. The relative scale factor d is defined as:

$$d = LE_m I_p, \tag{4-11}$$

where L is the lock-in amplifier sensitivity, E_m is the modulation energy, and I_p is the current of the incident electron beam. If all these factors are constant during the measurement, the scale factor in Equation 4-10 can be omitted.

One alternative method of quantitative analysis is an approach which does not refer to sensitivity factors. It involves the use of standard samples, consisting of only one element in the form of a thick layer, so it can be treated like a bulk material. The AES spectrum is recorded for a series of standard samples and then under the same conditions for the measured sample. The concentration of a given element is finally determined from the dependence:

$$C_x = \frac{\dfrac{I_x}{I_{x,etalon}}}{\sum_{\alpha} \dfrac{I_\alpha}{I_{\alpha,etalon}}}, \tag{4-12}$$

where I_x and $I_{x,etalon}$ are peak-to-peak amplitudes of Auger peaks for the measured sample and the standard sample, respectively. The summation is carried out for all α elements whose peaks are present in the Auger spectrum. This approach is very simple, though it does require standard samples of all the elements present in the spectrum to be measured.

Figure 4-19 presents the results of an experiment using AES. The experiment was carried out for a Si/Co (1 nm)/Cu (2 nm)/Pb (0.12 nm)/[Co (1 nm)/Cu (2 nm)] ×10 multilayer system and Auger spectra were collected *in situ* just after the deposition of each constituent layer. Clear lines of cobalt (57 eV), copper (66 eV), and lead (97 eV) can be observed in the low-energy range of the spectra. At the initial stage of the experiment, nothing strange happened. The spectrum collected after the deposition of the first layer of cobalt showed only the line originating from cobalt. Similarly, after the deposition of the next layer of copper, only the copper line appeared in the spectrum. However, this simple situation changed after the lead layer was deposited. In addition to the lines originating from Cu and Co, Pb lines appeared in all spectra, despite the fact that lead was deposited only once, after the first Co/Cu bilayer. This means that lead is always present on the sample surface. No cobalt line in the

spectrum recorded on the copper surface was noted, nor was the copper line in the spectrum recorded on the cobalt surface, which confirmed that the layers of these elements were continuous and thick. However, lead atoms were always able to get to the surface, which is proof that lead atoms segregate to the surface and behave as a surfactant.

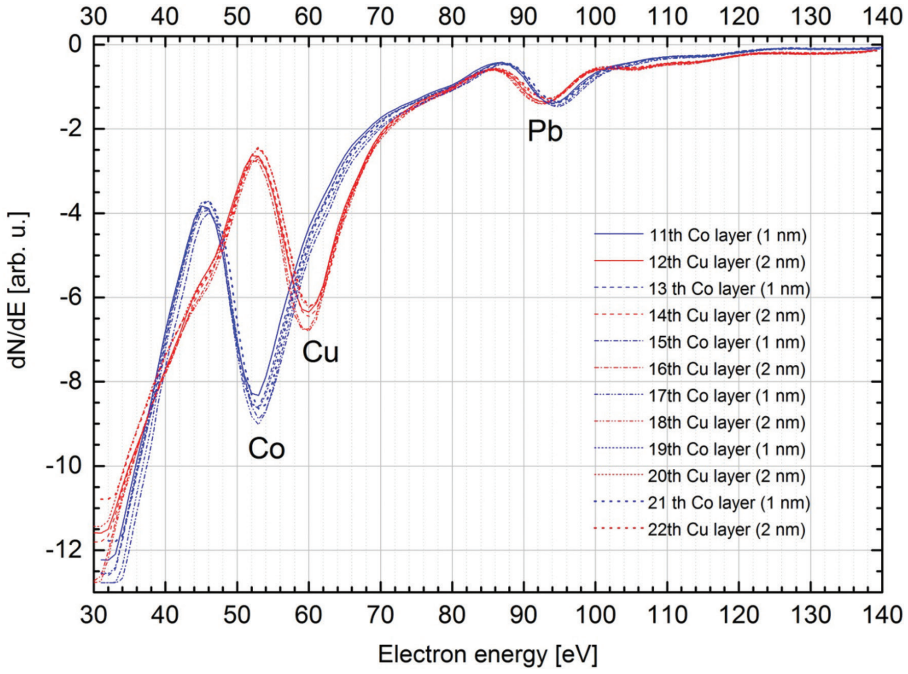

Figure 4-19. Example AES spectra collected for a Si/Co(1 nm)/Cu(2 nm)/Pb(0.12 nm)/[Co(1 nm)/Cu(2 nm)]x10 multilayer. The incident electron energy was 3 keV, the beam current 40 μA, and the beam diameter about 300 μm (own elaboration)

It is also worth paying attention to lead's peak positions. There is a slight shift of the peak position depending on whether the spectrum was recorded after the deposition of a cobalt or copper layer. This is connected with the 'chemical shift', which is a change in the energy levels of electrons in an atom depending on the elements that surround it. A small change in the energy levels of an atom results in a change in the energy of the Auger electrons, which can be observed as a shift in the peak position. Here, the average chemical shift is around 1 eV.

4.6. LOW-ENERGY ELECTRON DIFFRACTION (LEED)

Low-energy electron diffraction (LEED) is a technique for determining the surface structure of materials. It is based on the principle of irradiation with low-energy electrons (20–200 eV), followed by the observation of interference spots appearing on the screen due to the diffraction of electrons on the surface atoms. LEED experiments are performed in an ultra-high-vacuum environment (10^{-9} mbar) using the setup depicted in Figure 4-20.

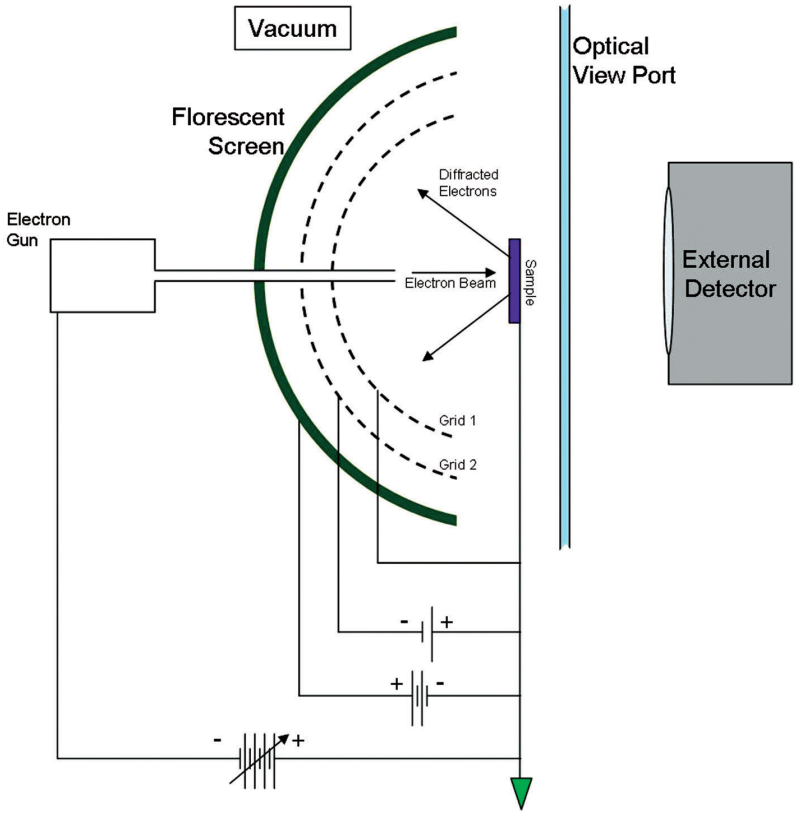

Figure 4-20. An LEED set-up (Jatosado, CC BY-SA 4.0, via Wikimedia Commons)

An LEED detector usually contains three or four concentric hemispherical grids and a phosphor screen or other position-sensitive detector. The grids are used to screen out the inelastically scattered electrons. Due this experimental set-up's similarity to the systems used for AES, the two techniques are often combined and the same system is adapted for the two types of experiments.

The low energy of the electrons reaching the sample results in the high surface sensitivity. Even for a monolayer one atom thick, an LEED diffraction image does

not contain any signal coming from the substrate. However, it is possible to design an experiment in such a way that spots in the diffraction pattern originate both from the substrate and the layer. For this purpose, a wide electron beam is used with a diameter of 1 mm or more. Such a wide electron beam is then directed to the border between the layer and the uncovered substrate, which yields a superposition of LEED images for the layer and the substrate. If the lattice constant for the substrate is known, the layer structure and its lattice parameters can be determined by analysing the diffraction spot location.

After the interference spots originating from the examined material are identified, the next step is to determine the distance between the nearest ones, which is proportional to the reciprocal lattice constants. For this purpose, the brightness profile of the LEED image is extracted along a line passing through neighbouring spots. The distance between the centres of the two closest peaks is proportional to the reciprocal lattice constant, hence inversely proportional to the real lattice constant. Therefore, by knowing the lattice parameters for a substrate, it is possible to easily recalculate the lattice constants for the layer. This method, however, only provides lattice parameters measured in the plane of the sample. In particular, it cannot measure the interplanar distance along the normal axis to the sample plane.

Figure 4-21 shows example LEED patterns for a MgO(100) single crystal and a Cr layer. In Figure 4-21a, a typical LEED pattern for a MgO(100) surface shows a low-intensity background and sharp spots. This indicates a that there are few point defects (contaminations) but large flat terraces that do not broaden the spots [38]. The LEED image shown in Figure 4-21b was recorded of the Cr layer deposited onto the MgO substrate. A four-fold symmetry pattern is visible, which confirms the epitaxial growth of Cr on MgO(100) and corresponds to the bcc structure of Cr(100) surface. However, much broader spots than in the previous case and a relatively intense background indicate surface defects [39].

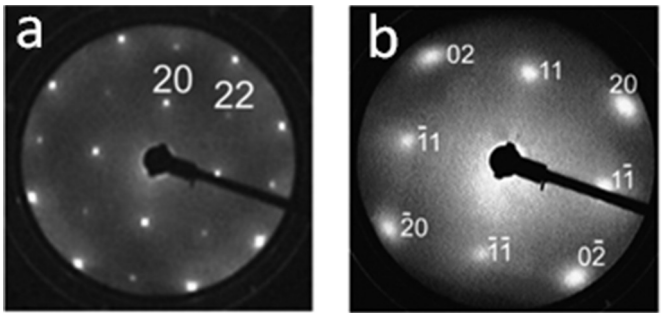

Figure 4-21. LEED patterns registered on (a) a cleaved MgO(100) substrate and on (b) a 20-nm Cr layer deposited onto the MgO(100) substrate. In both cases the incident electron beam energy was 180 eV [39] [38]

4.7. REFLECTION HIGH-ENERGY ELECTRON DIFFRACTION (RHEED)

LEED measurements are typically not carried out during the deposition of thin layers because of the unfavourable measurement geometry. In order to perform the measurement, the deposition must be interrupted and the sample must be rotated towards the detector. This disadvantage is not present in the RHEED method, which utilises the grazing incidence angle geometry and can be easily implemented in a molecular beam epitaxy chamber for *in situ* investigation of a surface structure during its growth. This technique allows the growth, reconstruction, and recrystallisation of thin films to be monitored during their deposition on a single crystalline substrate.

The principle of the RHEED method is very similar to LEED, but instead of low-energy electrons, electrons with energies of about 10 keV are used. Another difference is that the electrons do not reach the sample surface perpendicularly, but at a grazing angle (1–3°). The sample is placed in the middle of the instrument, between the electron gun and the position-sensitive detector, as shown in Figure 4-22. Due to the small incident angle of the incoming beam, the sample surface has to be flat enough to avoid casting any shadows. The penetration depth of the electron beam into the sample is defined by the incidence angle and the beam's energy. For low incidence angles, the energy of the wave propagating along the axis normal to the sample's surface is less than 1 keV. Such low energy in the transverse direction limits the penetration depth. As a result, only the topmost few atomic layers are affected. This allows the sample to be approximated as a two-dimensional layer [40].

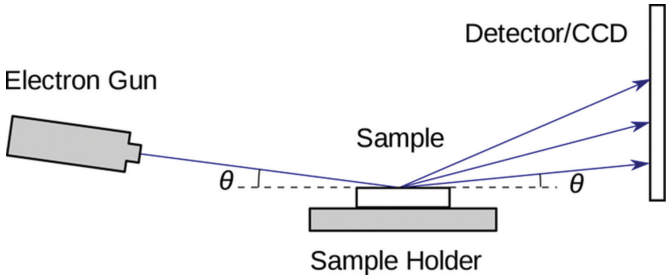

Figure 4-22. The general scheme of an RHEED setup [41]

An example of an RHEED pattern of a Pt thin film grown on freshly cleaved single crystalline $WSe_2(0001)$ surface is shown in Figure 4-23. The image presented in Figure 4-23a corresponds to the case of a low coverage (<0.5 Å), when it is possible to see both the streaks from the $WSe_2(0001)$ substrate and the weak spots from single-crystal Pt islands. Further Pt deposition leads to the substrate streaks vanishing and well-pronounced spots from Pt islands dominating in the diffraction pattern—see Figure 4-23b. This property of RHEED can be exploited to study the growth modes of thin films during deposition, surface reconstruction, and corrugation [40].

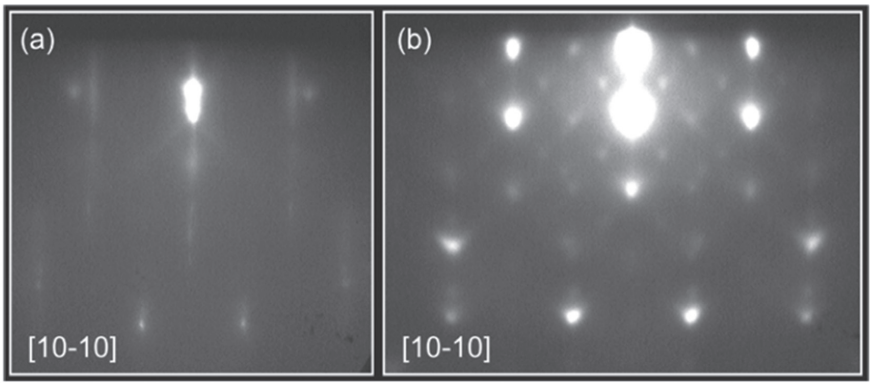

Figure 4-23. RHEED images taken after the deposition of (a) <0.5 Å and (b) 5 Å of Pt on WSe2(0001) at 450 °C [40]

4.8. MOLECULAR SPECTROSCOPY

Spectroscopy is a research area that deals with the interaction between electromagnetic radiation and matter. This interaction consists of absorbing part of the energy (absorption) through matter, or giving the matter some of the energy in the form of radiation (emission). One of the basic criteria for choosing a spectroscopic method for testing substances is the range of electromagnetic radiation. Table 2 shows the boundaries of individual ranges of electromagnetic radiation. Infrared (IR) spectra are most often presented in wavenumber units.

Table 2

The ranges of electromagnetic radiation

Far-UV	10–180 nm
Near-UV	180–400 nm
VIS	400–780 nm
IR	780 nm–1 mm (12,500–10 cm^{-1})

The molecular spectra contain information on the molecular structure and the bond strength. In the Born–Oppenheimer approximation, the energy of a molecule can be presented as:

$$E = E_{el} + E_{vib} + E_{rot}, \tag{4-13}$$

where E_{el} is electronic energy, E_{vib} is vibrational energy, and E_{rot} is rotational energy.

The electron energy in a molecule significantly exceeds the oscillating energy, which in turn is higher than the rotational energy ($E_{el} >> E_{vib} >> E_{rot}$).

Significant differences in the value of particular types of energy cause the appropriate spectra to appear in different spectral ranges. The absorption of far infrared radiation results in changes only in the rotational energy, while absorption of the radiation from the near-infrared range causes transitions between the oscillatory levels. The spectra obtained in the IR radiation range are used to identify the type of chemical bonds in the examined material.

Changes in the electron energy can only be caused by the absorption of the visible and ultraviolet radiation. The radiation in this range is absorbed due to the excitation of vibrations of larger fragments of molecules, such as phenyl groups. This spectroscopy does not provide very much information about the structure of molecules, but is useful for analysing their potential electro-optic properties. One piece of information that springs from electron spectra is the interband charge transfer, which may provide information on the potential photomagnetic properties of some samples.

4.8.1. UV–VIS SPECTROSCOPY

Traditionally, UV–Vis spectroscopy is used for samples prepared in the form of a solution. The absorbance measurement is then performed in relation to a reference solution, whose composition is similar and which is placed in an identical cuvette as the studied sample. According to the Lambert–Beer law, the absorbance is given by:

$$A = log \frac{I_0}{I_t}, \tag{4-14}$$

where I_0 is the incident light intensity and I_t is the transmitted light intensity.

UV–Vis spectroscopy can also be applied to samples prepared in the form of thin films, under the condition that the substrate on which the sample is deposited must be transparent to ultraviolet and visible radiation, for example, quartz. The principle of measuring electron spectra is very simple. The light source emits continuous electromagnetic radiation, which passes through the clear substrate, and the reference spectra are recorded. Afterwards, the measurement is repeated for a film deposited onto the substrate. Based on the difference between the light intensity passing through the clean substrate (I_0) and through the film deposited onto this substrate, the electron spectra are calculated and plotted as a function: $A = f(\lambda)$.

A very important aspect of measurements using UV–Vis radiation is spectroelectrochemistry. This is a set of techniques that enables the observation of *in situ* changes taking place in the recorded spectrum during the electrochemical reaction. In the case of spectroelectrochemical measurements, a set of three electrodes (the reference, counter, and working electrodes) is immersed in an electrochemically reactive solution. The voltage supplied to the electrodes by a potentiostat brings about the electrochemical reactions in the solution and

the UV–Vis spectrum is collected simultaneously. An increase or decrease in the measured absorbance observed as a result of the changes in the solution is attributed to the process of oxidation/reduction.

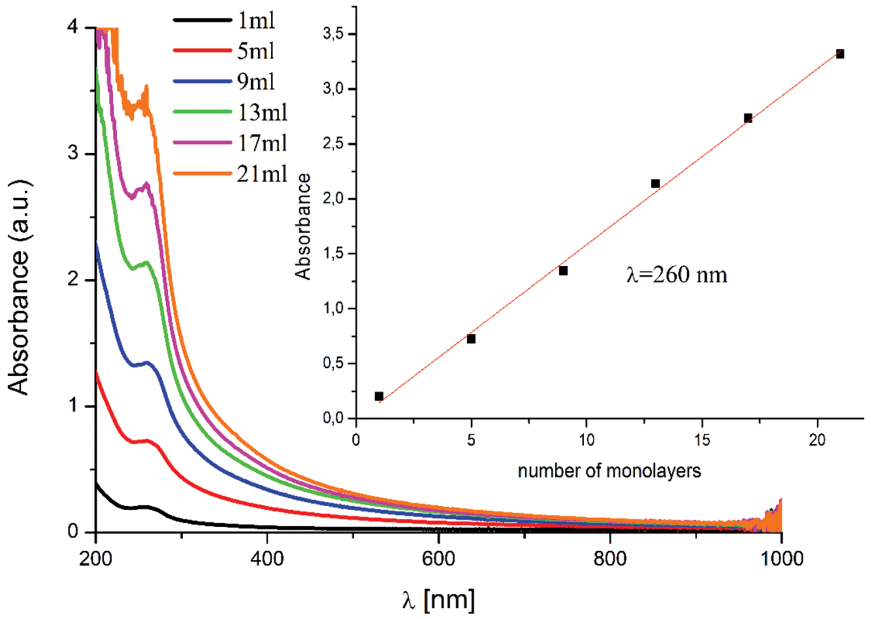

Figure 4-24. UV–Vis spectra obtained for a Langmuir–Blodgett thin film of DODA+$Ni_3[Cr(CN)_6]_2$ deposited onto a quartz substrate with varying numbers of monolayers. The inset presents the dependence of absorbance measured for the wavelength of 260 nm on the number of monolayers (own elaboration)

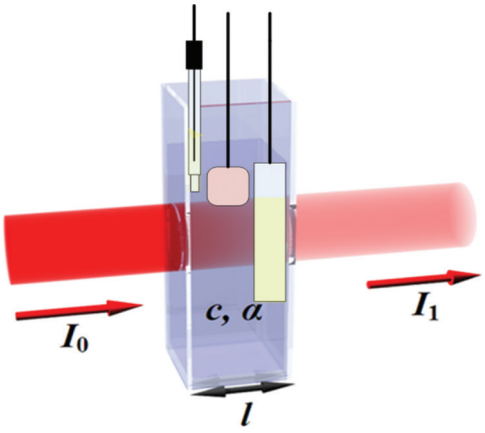

Figure 4-25. A UV–Vis spectroelectrochemical cell containing a set of electrodes (reference, working, and counter) immersed in an electroactive solution. I_0 and I_1 are the incident and transmitted light intensities, respectively, c is the solution's concentration, and α is the absorption coefficient of the solution [42]

Spectroelectrochemistry is also widely used to control the process of thin film formation with the electrochemical method (e.g. thin layers of conductive polymers or Prussian blue analogues). A transparent glass electrode covered with ITO should be used as a working electrode. The application of a constant potential to the system during a chronoculometry experiment causes reduction/oxidation of the solution in the vicinity of the electrode and finally the deposition of the material onto the surface of the working electrode. An increase in the intensity of absorbance is confirmation that a film is growing on the surface of the electrode. This is a very useful tool in both in the characterisation and quality assessment of a material [31].

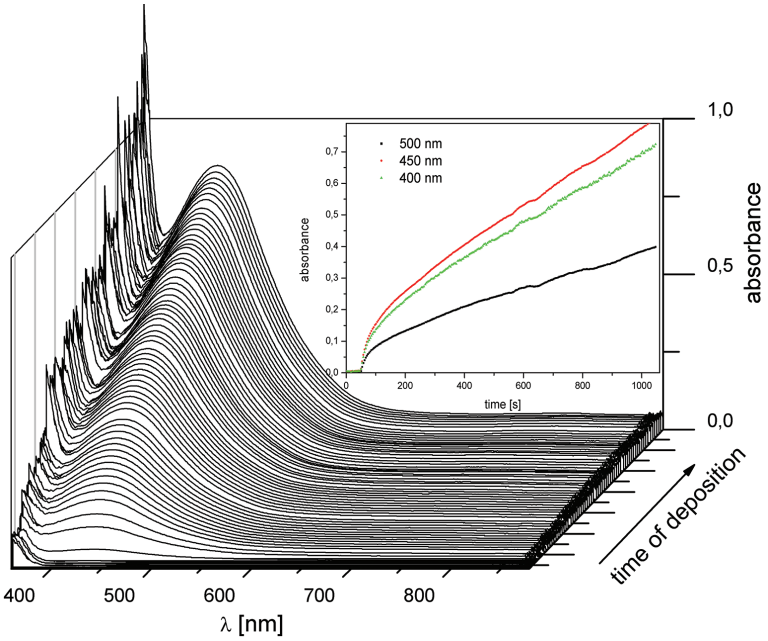

Figure 4-26. UV–Vis spectra obtained during the electrodeposition of a $Fe_3[Cr(CN)_6]_2 \cdot 15H_2O$ thin film. The inset shows the time dependence of the absorbance of the film at different wavelengths [31]

4.8.2. IR SPECTROSCOPY IN THE STUDY OF THIN FILMS: ATTENUATED TOTAL REFLECTANCE (ATR)

In the case of powder samples, the IR spectrum is measured using Fourier Transform Infrared (FTIR) spectrometers. In FTIR spectrometers, IR light from the light source passes through a Michelson interferometer along the optical path. A moving mirror inside the apparatus alters the distribution of infrared light passing through the interferometer. The signal which is directly recorded, called an 'interferogram', represents light output as a function of mirror position. The spectrum is obtained by applying a Fourier transform to the resulting interferogram.

In the case of samples obtained in the form of thin films, the transmission method cannot be used due to the substrate on which the sample is to be deposited. In order to measure the IR spectrum of samples deposited onto a solid substrate, either specular reflectance or the ATR technique is used. In both cases, an additional adapter must be installed inside the IR spectrometer. The most important element of this equipment is its system of mirrors, which allows the beam of IR radiation to be directed onto the surface of the sample, from which the beam is reflected into the detector. This is a technique that allows one to measure samples in the form of thin layers deposited on an opaque substrate or thin metallic foils.

In cases where the sample contains a very small amount of material and it is impossible to obtain a signal with the specular reflectance technique, the ATR technique is used instead. The main element of ATR is a prism with a high refractive index, on which the sample is placed. The beam of IR radiation is directed to one of the walls of the prism and comes out the other side after being totally reflected from its inner side. A diagram of the construction of an ATR system is shown in Figure 4-27.

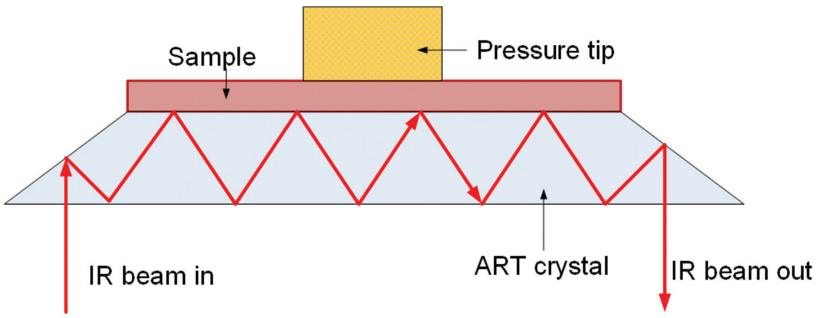

Figure 4-27. An ATR-FTIR device used to obtain infrared spectra for samples prepared in the form of thin films (own elaboration)

Total internal reflectance occurs when the angle of the incident radiation θ exceeds the critical angle θ_c. The critical angle is a function of the refractive indices of the sample and the ATR crystal, defined as:

$$\theta_c = arcsin\left(\frac{n_2}{n_1}\right), \tag{4-15}$$

where n_1 is the refractive index of the ATR crystal and n_2 is the refractive index of the sample.

The most commonly used ATR crystal is ZnSe, with a refractive index of $n = 2.89$. A system of movable mirrors allows one to set an appropriate angle of incidence of the IR radiation. The condition for obtaining a quality spectrum is having good optical contact between the sample and the prism. For this purpose, a clamp is

attached to a movable screw. The thickness of the sample does not affect the quality of the spectrum, unlike in the case of transmission spectra. An additional advantage is also the ability to use a smooth or flexible substrate. This method allows one to perform measurements even for single monolayers, such as those obtained by the self-organisation method.

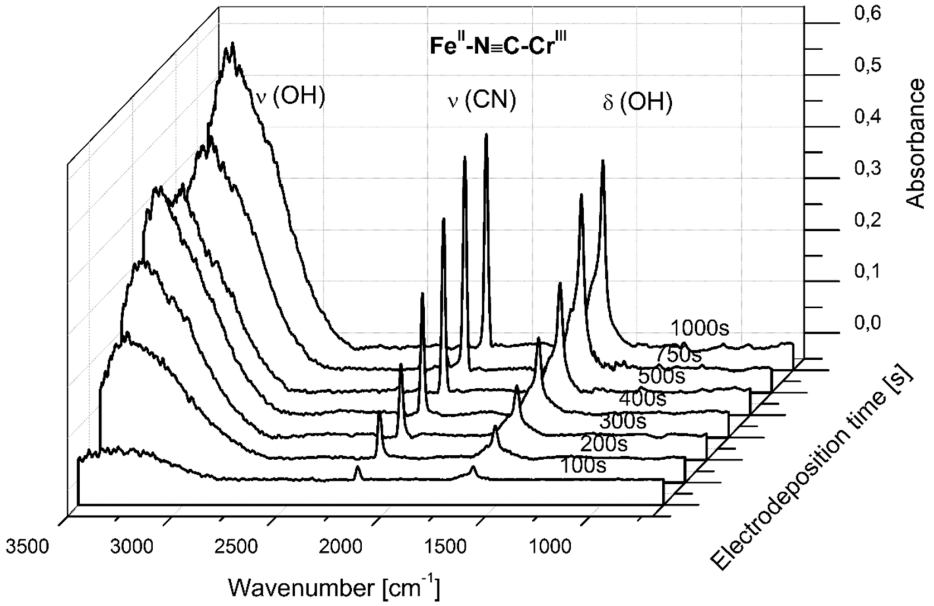

Figure 4-28. ATR-IR spectrum of an $Fe_3[Cr(CN)_6]_2 \cdot 15H_2O$ thin film fabricated with various deposition times: increasing the deposition time results in thicker films; therefore, increased absorbance is observed [42]

5. APPLIED NANOSCIENCE: READ HEADS AND MAGNETIC MEMORY

5.1. APPLICATION OF MTJS IN HDD READ HEADS

A hard disk drive (HDD) is an electro-mechanical data storage device. A photo depicting the main components of an HDD is presented in Figure 5-1.

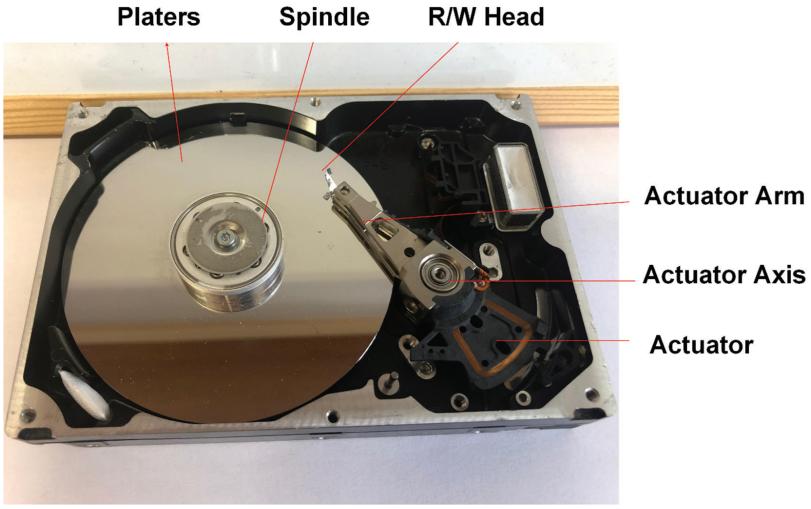

Figure 5-1. Hard disk drive components (own photo)

The basic component of HDD is the rapidly rotating disks (platters) coated with a magnetic material. A typical HDD has two electric motors: a spindle motor that spins the disks and an actuator which positions the read/write head assembly across the spinning disks. The platters rotate at a constant speed of 3600–7200 rpm. Above the surface of the platters, the read-write head is placed at the end of the actuator arm. The distance between the head and the carrier is about $5 \cdot 10^{-6}$ cm.

One of the most important commercial applications of magnetic tunnel junctions is in HDD read heads. The detailed structure of an MTJ read head in an HDD is shown in Figure 5-2. The MTJ is composed of three magnetic electrodes. The first

one is called the free layer—its magnetic moment can move freely during the change of an external magnetic field. The next electrode is the ferromagnetic reference layer, whose magnetic moments are fixed in the vertical direction to the disk surface because it is covered by the pinned layer. The magnetic moment orientation of the pinned layer is enforced by an exchange bias field, occurring at the interface between the pinned and antiferromagnetic layers. The pinned layer is part of this system to compensate the stray field from the reference layer, and its magnetisation orientation is always opposite to that of the reference layer. In the read head, the MTJ element is sandwiched between two permanent magnets (for clarity, only one of them is shown in Figure 5-2). The role of these magnets is to maintain the single domain state of the free layer in the junction.

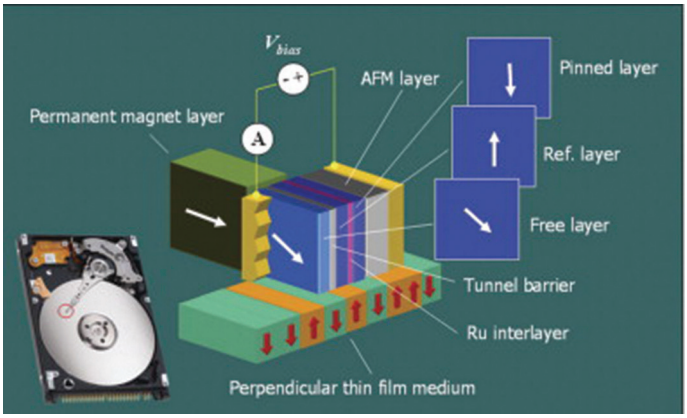

Figure 5-2. A schematic representation of the MTJ read head in an HDD [43]

One of the most important requirements for materials used in the construction of an MTJ is an appropriate resistance-area (RA) product. The miniaturisation of devices makes it necessary to reduce the size of the MTJ elements, which results in increased resistance. The consequences of higher head resistance are more noise and a limited data transfer rate.

Nowadays, HDD read heads are constructed from MgO-based MTJs [44], [45] the microfabricated MTJs manifest a very large tunnel magnetoresistance (TMR. The most important features of MgO are its extremely high TMR ratio and ultra-low *RA* product.

5.2. APPLICATION OF MTJS IN MRAM

One of the basic applications of MTJs is in magnetic random-access memory (MRAM). The development of MRAM mostly took place in the past decade.

The simplest possible memory element has the following components:

- the free layer, also called the storage layer—a ferromagnetic thin film often made of CoFeB
- the tunnel barrier—a thin film and nonmagnetic insulator usually made of MgO, AlOx, or TiO
- the reference layer—designed to have much higher magnetic anisotropy than the storage layer, so its magnetic moments never switch during memory operations

The shape of a memory element is elliptical, which provides the shape anisotropy with an easy axis along the long axis. As shown in Figure 5-3, with uniaxial magnetic anisotropy, the magnetisation orientation of the storage layer becomes binary:

– a '0' state is achieved for parallel configuration of magnetic moments of the magnetic layers separated by a tunnel barrier
– a '1' state is obtained for antiparallel configuration of magnetic moments of the magnetic layers separated by a tunnel barrier

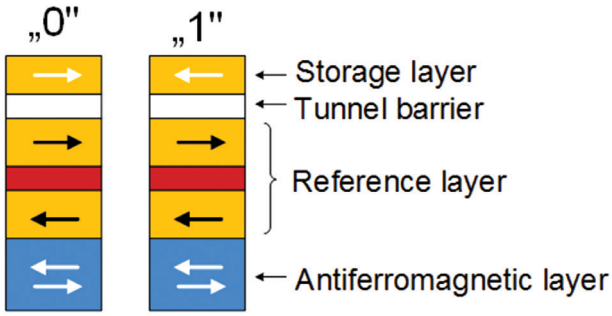

Figure 5-3. A conventional memory element design with a single storage layer (own elaboration)

The MRAM architecture consists of a bit line and a word line (Figure 5-4). The switching between the '1' and '0' states of a selected element is based on the application of a magnetic field, generated by current-carrying wires. The current passing through the bit line and word line corresponding to a particular MRAM element provokes the generation of two magnetic fields orthogonal to each other. The current in the bit line generates a magnetic field in the transverse direction to the easy axis, while the current in the word line generates a magnetic field along the easy axis. In this MRAM architecture, there is a certain drawback: half-addressed junctions.

The relatively new and rapidly developing non-volatile memory is spin-transfer torque magnetic random-access memory (STT-MRAM). Spin-transfer torque (STT) is an effect in which the spin-polarised current is used to control the magnetisation orientation of a magnetic layer in an MTJ or spin valve. In general, an electric current is unpolarised: it consists of 50% spin-up and 50% spin-down electrons. In the situation where the current contains a majority of one type of electrons (spin-up or spin-down), the current is spin-polarised. A spin-polarised current can be

produced by passing this current through a thick magnetic layer (Figure 5-5). If this spin-polarised current is then steered into a thinner magnetic layer, the angular momentum can be transferred to this layer, changing its orientation.

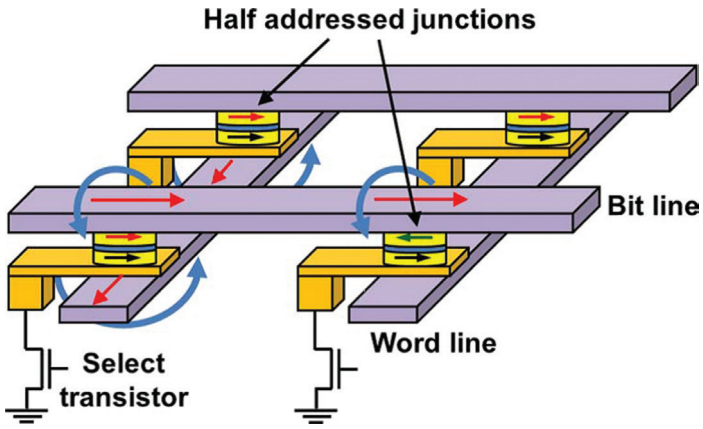

Figure 5-4. An MRAM memory element array [53]

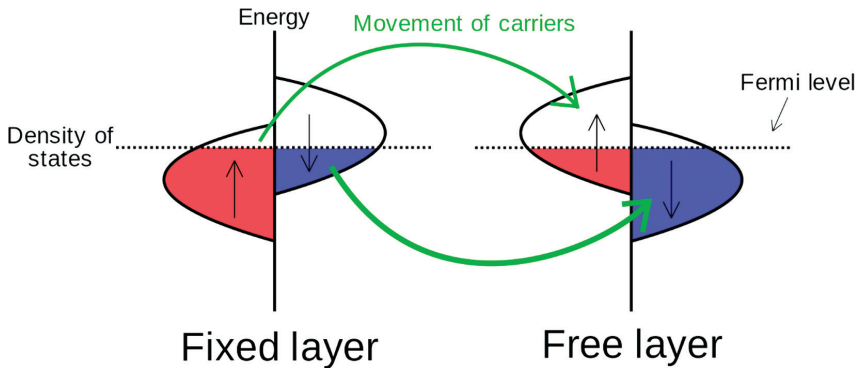

Figure 5-5. A model of spin-transfer torque for two anti-aligned layers. The current passing through the fixed layer is spin-polarised. When it reaches the free layer the majority spins relax into lower-energy states of opposite spin, applying torque to the free layer in the process [46]

The STT switching in magnetic nanostructures was first experimentally observed in 2000, while the first few proposals on STT-MRAM appeared in 2006. The advantage of STT-MRAM is the fact that no external magnetic field is necessary to switch the state of magnetisation. In the STT method, the magnetisation is switched by sending a current through the device. If the magnetisation direction in the STT switching process needs to be changed from antiparallel to parallel orientation, the electrons are directed from the pinned layer to the free layer. When the electrons are passed through the pinned layer, the minority electrons are scattered and in the end only the

majority electrons reach the free layer giving the spin-polarised current. When this polarised current reaches the free layer, the spin angular momentum exerts a torque on the magnetisation of the layer that is orientated antiparallel to the pinned layer. As a result of this torque generated by several electrons, the magnetisation changes direction from antiparallel to parallel. A comparison of the architecture of MRAMs with field-induced STT switching is presented in Figure 5-6.

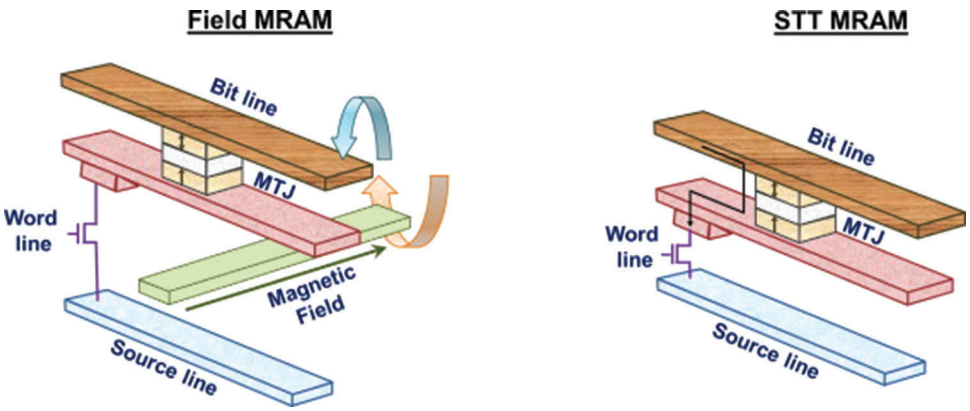

Figure 5-6. A comparison of the architecture of MRAMs with (a) field-induced switching and (b) spin transfer torque (STT) switching, in which the current is sent through the MTJ and the resultant structure is much less complex than that of field MRAM [2]

6. APPENDIX 1: CALCULATION OF THE DENSITY OF 3D, 2D, 1D, AND 0D STATES

3D Density of states

The density of states describes the number of electron (or hole) states allowed per volume at a given energy. It can be derived from basic quantum mechanics.

When we consider the electrons in a solid as a free electron gas, that is, the electrons are free to move around the crystal without being influenced by the potential of the atomic nuclei, a free electron has a velocity V and a momentum $p = mV$. Its energy can be described by the formula:

$$E = \frac{1}{2}mV^2 = \frac{|p|^2}{2m} = \frac{\hbar^2 k^2}{2m}. \tag{6-1}$$

The electrons' position is described by wave function Ψ (x, y, z). This wave function for the electron must satisfy the Schrödinger equation, subject to boundary conditions. The electrons approximately behave as free particles trapped in a box of rectangular volume $L_x \times L_y \times L_z$. The solution of the Schrödinger equation leads to wave functions of the form:

$$\Psi(x,y,z) = \sin(k_x x)\sin(k_y y)\sin(k_z z), \tag{6-2}$$

where k_x, k_y, and k_z are wave vectors for an electron in the x, y, and z directions. Taking into account the boundary conditions (at x, y, and $z = 0$, the sine functions goes to zero, whilst at the opposite boundaries of the rectangular region $\sin(k_x L_x) = 0$, $\sin(k_y L_y) = 0$, and $\sin(k_z L_z) = 0$, for x, y, and z directions), the solution for wave vectors is given by:

$$k_x L_x = \pi n_x, k_y L_y = \pi n_y, k_z L_z = \pi n_z, \tag{6-3}$$

where n_x, n_y, and n_z are integers.

With this restriction in k-space, only certain values of k-space lead to acceptable electron wave function solutions. k-space would be filled if each position was filled with a cubic unit cell of volume. Explicitly, the k-space volume of a single-state cube in k-space is equal to

$$V_{3D} = \left(\frac{\pi}{L}\right)^3, \tag{6-4}$$

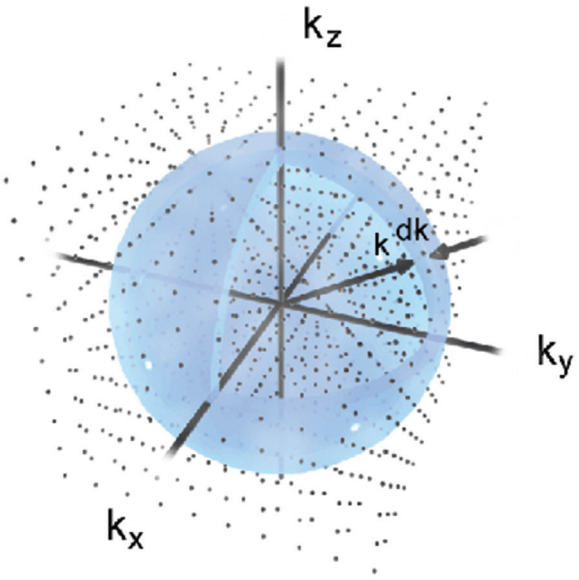

Figure 6-1. A visualisation of *k*-space showing values of k as points. The number of allowed states is the number of such points contained in the shell of radius *k* and thickness *dk* [53]

The diagram presented in Figure 6-1 shows the spherical shells. The problem of finding the number of allowed states amounts to finding the number of these allowed states between spheres of radius *k* and *k* + *dk*.

Taking into account the fact that the *k*-space volume of a sphere is equal to

$$V_{sphere} = \frac{4\pi \boldsymbol{k}^3}{3}, \tag{6-5}$$

the volume between the two shells is given by:

$$dV_{sphere} = 4\pi k^2 dk. \tag{6-6}$$

The number of *k* states within the spherical shell, $g(k)dk$, is obtained by dividing the volume dV_{sphere} by the volume of a single energy state. Each k state can hold two electrons, so an additional factor of two must be introduced to the formula:

$$g(k)dk = 2 \cdot \frac{dV_{sphere}}{V_{3D}} = 8\frac{L^3 k^2 dk}{\pi^2}. \tag{6-7}$$

It is not possible to distinguish a wave function that differs only in the sign. Equation 6-7 must be divided by 8 to avoid multiple counting of the same quantum state:

$$g(k)dk = \frac{1}{8} \cdot 8 \frac{L^3 k^2 dk}{\pi^2} = \frac{L^3 k^2 dk}{\pi^2}. \tag{6-8}$$

Rewriting Equation 6-1, one obtains:

$$k^2 = \frac{2mE}{\hbar^2}. \tag{6-9}$$

After differentiating it becomes:

$$2kdk = \frac{2mdE}{\hbar^2}. \tag{6-10}$$

Combining Equations 6-9 and 6-10 yields:

$$dk = \frac{2mdE}{2k\hbar^2} = \frac{mdE}{k\hbar^2} = \frac{mdE}{\hbar^2\sqrt{\frac{2mE}{\hbar^2}}} = \left(\frac{2mE}{\hbar^2}\right)^{-1/2} \frac{m}{\hbar^2} dE. \tag{6-11}$$

Plugging Equations 6-9 and 6-11 into Equation 6-8, we obtain:

$$g(k)dk = \frac{L^3 k^2}{\pi^2} \left(\frac{2mE}{\hbar^2}\right)^{-1/2} \frac{m}{\hbar^2} dE = \frac{L^3 m[2mE]^{1/2}}{\pi^2 \hbar^3} dE. \tag{6-12}$$

Taking the bulk case as an example, the density of states in terms of energy is then:

$$g(E)_{3D}\, dE = \frac{k^2 dk}{\pi^2} = \frac{2mE}{\pi^2\hbar^2}\left(\frac{2mE}{\hbar^2}\right)^{-1/2} \frac{m}{\hbar^2} dE = \frac{1}{2\pi^2}\left(\frac{2m}{\hbar^2}\right)^{3/2} E^{1/2}\, dE. \tag{6-13}$$

2D Density of states

In two-dimensional structures, such as a quantum well, the procedure is much the same, but this time one of the *k*-space components is fixed. Instead of a finding the number of *k*-states enclosed within a sphere, the problem becomes calculating the number of *k*-states lying in an annulus of radius *k* to *k* + *dk* (Figure 6-2). *k*-space would be completely filled if each state occupied an area of

$$V_{2D} = \left(\frac{\pi}{L}\right)^2. \tag{6-14}$$

Taking into account the fact that the k-space area of a circle is equal to:

$$V_{circle} = \pi k^2. \tag{6-15}$$

The 'volume' of the annulus is given by:

$$dV_{circle} = 2\pi k dk. \tag{6-16}$$

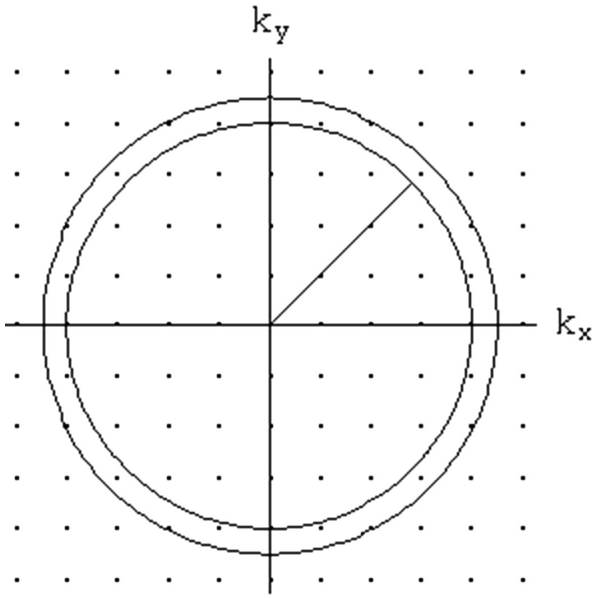

Figure 6-2. *k*-space in 2D: The density of states at an energy *E* is the number of *k*-states per unit volume contained with the annulus of radius *k* and thickness *dk* [53]

The number of *k* states in 2D, , is obtained by dividing the 'volume' dV_{circle} of the *k*-state by the area of the annulus (remembering to multiply by 2 to account for the electron spin states and to divide by 4 due to equivalent nature of the +/- states):

$$g(k)dk = 2 \cdot \frac{1}{4} \cdot \frac{dV_{circle}}{V_{2D}} = \frac{L^2 kdk}{\pi}. \tag{6-17}$$

In terms of energy per unit volume, the 2D density of state is described by the formula:

$$g(E)_{2D}\, dE = \frac{kdk}{\pi} = \frac{1}{\pi}\left(\frac{2mE}{\hbar^2}\right)^{\frac{1}{2}} (2mE)^{-\frac{1}{2}} \frac{m}{\hbar} dE = \frac{m}{\pi\hbar^2} dE. \tag{6-18}$$

Unlike the 3D case, this expression does not depend on energy, which means that if the top of the energy gap is reached, there is a significant number of available states.

1D Density of states

A similar approach is taken for calculating the density of states for a 1D structure. In one dimension, two of the *k*-components are fixed, so the area of *k*-space becomes a length and the area of the annulus becomes a line.

$$V_{1D} = \frac{\pi}{L}. \tag{6-19}$$

$$V_{line} = k. \tag{6-20}$$

$$dV_{line} = dk. \tag{6-21}$$

Therefore, the density of states per unit length in 1D and multiplying by 2 for spin degeneracy can be expressed as:

$$g(k)dk = 2 \cdot \frac{1}{2} \cdot \frac{dV_{line}}{V_{1D}} = \frac{Ldk}{\pi}. \tag{6-22}$$

For one dimension, the density of states per unit volume at energy E is given by:

$$g(E)_{1D}\, dE = \frac{1}{\pi}\left(\frac{2mE}{\hbar^2}\right)^{-1/2} \frac{m}{\hbar^2} dE = \frac{1}{\pi\hbar}\sqrt{\frac{m}{2E}}\, dE. \tag{6-23}$$

0D Density of states

In a 0D structure, such as quantum dot, no free motion of electrons is possible. There is no k-space to be filled with electrons and available states exist only at discrete energies. The density of state for 0D is described by the delta function:

$$g(E)_{0D} = 2\delta(E). \tag{6-24}$$

7. APPENDIX 2: UNITS USED IN MAGNETIC MEASUREMENTS

UNITS FOR MAGNETIC PROPERTIES

Quantity	Symbol	Gaussian & cgs emu [a]	Conversion factor, C [b]	SI & rationalized mks [c]
Magnetic flux density, magnetic induction	B	gauss (G) [d]	10^{-4}	tesla (T), Wb/m^2
Magnetic flux	Φ	maxwell (Mx), $G \cdot cm^2$	10^{-8}	weber (Wb), volt second (V·s)
Magnetic potential difference, magnetomotive force	U, F	gilbert (Gb)	$10/4\pi$	ampere (A)
Magnetic field strength, magnetizing force	H	oersted (Oe),[e] Gb/cm	$10^3/4\pi$	A/m [f]
(Volume) magnetization [g]	M	emu/cm^3 [h]	10^3	A/m
(Volume) magnetization	$4\pi M$	G	$10^3/4\pi$	A/m
Magnetic polarization, intensity of magnetization	J, I	emu/cm^3	$4\pi \times 10^{-4}$	T, Wb/m^2 [i]
(Mass) magnetization	σ, M	emu/g	1 $4\pi \times 10^{-7}$	$A \cdot m^2/kg$ $Wb \cdot m/kg$
Magnetic moment	m	emu, erg/G	10^{-3}	$A \cdot m^2$, joule per tesla (J/T)
Magnetic dipole moment	j	emu, erg/G	$4\pi \times 10^{-10}$	$Wb \cdot m$ [i]
(Volume) susceptibility	χ, κ	dimensionless, emu/cm^3	4π $(4\pi)^2 \times 10^{-7}$	dimensionless henry per meter (H/m), $Wb/(A \cdot m)$
(Mass) susceptibility	χ_ρ, κ_ρ	cm^3/g, emu/g	$4\pi \times 10^{-3}$ $(4\pi)^2 \times 10^{-10}$	m^3/kg $H \cdot m^2/kg$
(Molar) susceptibility	χ_{mol}, κ_{mol}	cm^3/mol, emu/mol	$4\pi \times 10^{-6}$ $(4\pi)^2 \times 10^{-13}$	m^3/mol $H \cdot m^2/mol$
Permeability	μ	dimensionless	$4\pi \times 10^{-7}$	H/m, $Wb/(A \cdot m)$
Relative permeability [j]	μ_r	not defined		dimensionless
(Volume) energy density, energy product [k]	W	erg/cm^3	10^{-1}	J/m^3
Demagnetization factor	D, N	dimensionless	$1/4\pi$	dimensionless

a. Gaussian units and cgs emu are the same for magnetic properties. The defining relation is $B = H + 4\pi M$.
b. Multiply a number in Gaussian units by C to convert it to SI (e.g., $1\ G \times 10^{-4}\ T/G = 10^{-4}\ T$).
c. SI (*Système International d'Unités*) has been adopted by the National Bureau of Standards. Where two conversion factors are given, the upper one is recognized under, or consistent with, SI and is based on the definition $B = \mu_0(H + M)$, where $\mu_0 = 4\pi \times 10^{-7}$ H/m. The lower one is not recognized under SI and is based on the definition $B = \mu_0 H + J$, where the symbol I is often used in place of J.
d. 1 gauss $= 10^5$ gamma (γ).
e. Both oersted and gauss are expressed as $cm^{-1/2} \cdot g^{1/2} \cdot s^{-1}$ in terms of base units.
f. A/m was often expressed as "ampere-turn per meter" when used for magnetic field strength.
g. Magnetic moment per unit volume.
h. The designation "emu" is not a unit.
i. Recognized under SI, even though based on the definition $B = \mu_0 H + J$. See footnote *c*.
j. $\mu_r = \mu/\mu_0 = 1 + \chi$, all in SI. μ_r is equal to Gaussian μ.
k. $B \cdot H$ and $\mu_0 M \cdot H$ have SI units J/m^3; $M \cdot H$ and $B \cdot H/4\pi$ have Gaussian units erg/cm^3.

R. B. Goldfarb and F. R. Fickett, U.S. Department of Commerce, National Bureau of Standards, Boulder, Colorado 80303, March 1985
NBS Special Publication 696 For sale by the Superintendent of Documents, U.S. Government Printing Office, Washington, DC 20402

REFERENCES

[1] K. E. Drexler, "The Coming Era of Nanotechnology," *The Materials Revolution: Superconductors, New Materials, and the Japanese Challenge*, 1988.

[2] S. Bhatti, R. Sbiaa, A. Hirohata, H. Ohno, S. Fukami, and S. N. Piramanayagam, "Spintronics based random access memory: a review," *Materials Today*, 2017.

[3] P. Colson, C. Henrist, and R. Cloots, "Nanosphere Lithography: A Powerful Method for the Controlled Manufacturing of Nanomaterials," *J. Nanomater.*, 2013.

[4] R. Micheletto, H. Fukuda, and M. Ohtsu, "A Simple Method for the Production of a Two-Dimensional, Ordered Array of Small Latex Particles," *Langmuir*, 1995.

[5] W. Lee and S.-J. Park, "Porous Anodic Aluminium Oxide: Anodization and Templated Synthesis of Functional Nanostructures," *Chem. Rev.*, 2014.

[6] H. Masuda and M. Satoh, "Fabrication of gold nanodot array using anodic porous alumina as an evaporation mask," *Japanese J. Appl. Physics, Part 2 Lett.*, 1996.

[7] S. I. Ohkoshi, Y. Einaga, A. Fujishima, and K. Hashimoto, "Magnetic properties and optical control of electrochemically prepared iron-chromium polycyanides," *J. Electroanal. Chem.*, 1999.

[8] S. ichi Ohkoshi, M. Mizuno, G. jye Hung, and K. Hashimoto, "Magnetooptical effects of room temperature molecular-based magnetic films composed of vanadium hexacyanochromates," *J. Phys. Chem. B*, 2000.

[9] W. Chen and T. J. McCarthy, "Layer-by-layer deposition: A tool for polymer surface modification," *Macromolecules*, 1997.

[10] J. J. Richardson, J. Cui, M. Björnmalm, J. A. Braunger, H. Ejima, and F. Caruso, "Innovation in Layer-by-Layer Assembly," *Chemical Reviews*, 2016.

[11] G. Decher, "Fuzzy nanoassemblies: Toward layered polymeric multicomposites," *Science (80-.)*, 1997.

[12] S. Kaya, "On the magnetisation of single crystals of nickel," *Sci. Rep. Tohoku Imp. Univ*. 17, 639, 1928

[13] F. J. A. den Broeder, W. Hoving, and P. J. H. Bloemen, "Magnetic anisotropy of multilayers," *J. Magn. Magn. Mater.*, 1991.

[14] W. H. Meiklejohn and C. P. Bean, "New magnetic anisotropy," *Phys. Rev.*, 1957.

[15] M. Perzanowski, M. Marszalek, A. Zarzycki, M. Krupinski, A. Dziedzic, and Y. Zabila, "Influence of Superparamagnetism on Exchange Anisotropy at CoO/[Co/Pd] Interfaces," *ACS Appl. Mater. Interfaces*, 2016.

[16] S. S. P. Parkin and D. Mauri, "Spin engineering: Direct determination of the Ruderman-Kittel-Kasuya-Yosida far-field range function in ruthenium," *Phys. Rev. B*, 1991.

[17] M. N. Baibich *et al.*, "Giant magnetoresistance of (001)Fe/(001)Cr magnetic superlattices," *Phys. Rev. Lett.*, 1988.
[18] M. Julliere, "Tunnelling between ferromagnetic films," *Phys. Lett. A*, 1975.
[19] V. A. Dediu, "Organic spintronics: Inside the interface," *Nature Physics*, 2013.
[20] V. A. Dediu, L. E. Hueso, I. Bergenti, and C. Taliani, "Spin routes in organic semiconductors," *Nat. Mater.*, 2009.
[21] L. Guo, X. Gu, X. Zhu, and X. Sun, "Recent Advances in Molecular Spintronics: Multifunctional Spintronic Devices," *Adv. Mater.*, 2019.
[22] A. Caneschi, D. Gatteschi, R. Sessoli, A. L. Barra, L. C. Brunei, and M. Guillot, "Alternating Current Susceptibility, High Field Magnetisation, and Millimeter Band EPR Evidence for a Ground S = 10 State in [Mn12O12(CH3COO)16(H2O)4].2CH3COOH.4H2O," *J. Am. Chem. Soc.*, 1991.
[23] L. Bogani and W. Wernsdorfer, "Molecular spintronics using single-molecule magnets," *Nat. Mater.*, 2008.
[24] C. Castelnovo, R. Moessner, and S. L. Sondhi, "Magnetic monopoles in spin ice," *Nature*, 2008.
[25] R. F. Wang *et al.*, "Artificial 'spin ice' in a geometrically frustrated lattice of nanoscale ferromagnetic islands," *Nature*, 2006.
[26] M. Schmid and G. Pietrzak, "Schematic diagram of a scanning tunnelling microscope," 2005. [Online]. Available: https://commons.wikimedia.org/wiki/File:Rastertunnelmikroskop-schema.svg (access: 1/03/2023).
[27] P. Erler *et al.*, "Highly Ordered Surface Self-Assembly of Fe<inf>4</inf> Single Molecule Magnets," *Nano Lett.*, 2015.
[28] R. Wiesendanger, "Nano-scale studies of quantum phenomena by scanning probe spectroscopy," *Ann. der Phys.*, 2000.
[29] E. Casero, L. Vázquez, A. M. Parra-Alfambra, and E. Lorenzo, "AFM, SECM and QCM as useful analytical tools in the characterization of enzyme-based bioanalytical platforms," *Analyst*, 2010.
[30] G.F. Fitzgerald, "I. On the rotation of the plane of polarization of light by reflection from the pole of a magnet" Proc. R. Soc. 25, 1877.
[31] E. Coronado, M. Makarewicz, J. P. Prieto-Ruiz, H. Prima-García, and F. M. Romero, "Magneto-optical properties of electrodeposited thin films of the molecule-based magnet Cr 5.5 (CN) 12 ·11.5H 2 O," *Adv. Mater.*, 2011.
[32] M. Fitta *et al.*, "Magnetic and magneto-optical properties of nickel hexacyanoferrate/chromate thin films," *RSC Adv.*, vol. 7, no. 3, 2017.
[33] A. A. Vives, *Piezoelectric transducers and applications*, 2008.
[34] Y. Zabila, "Direct laser interference patterning of FePt and FePd alloys," PhD Thesis, Instytut Fizyki Jądrowej Polskiej Akademii Nauk, 2011.
[35] K. Wetzig and C. M. Schneider, "Introduction," in *Metal Based Thin Films for Electronics*, 2005.

[36] M. Krupiński, "Magnetic properties and structure of patterned FePd thin films improved by alloy admixtures," PhD Thesis, Instytut Fizyki Jądrowej Polskiej Akademii Nauk, 2013.
[37] K. D. Childs *et al.*, *Handbook of Auger Electron Spectroscopy, Appendix C. Auger Sensitivity Factors*, Physical Electronics Publishing, 1995.
[38] M. Kąc, J. Morgiel, A. Polit, Y. Zabila, and M. Marszałek, "Atomic scale structure investigations of epitaxial Fe/Cr multilayers," *Appl. Surf. Sci.*, 2014.
[39] M. Kąc, A. Polit, A. Dobrowolska, Y. Zabila, M. Krupiński, and M. Marszałek, "Surfactant influence on interface roughness and magnetoresistance value in Fe/Cr multilayers," *Thin Solid Films*, 2013.
[40] D. Makarov, "CoPt and FePt magnetic alloys grown on van der Waals WSe2(0001) surfaces and on arrays of SiO2 spherical particles," Universität Konstanz, 2008.
[41] Atenrok, "Reflection high-energy electron diffraction," 2013. [Online]. Available: https://commons.wikimedia.org/wiki/File:RHEED.svg (access: 1/03/2023).
[42] M. Makarewicz, "Okta- i heksacyjanki metali przejściowych jako baza dla molekularnych materiałów funkcjonalnych" (Octa- and hexacyanometalates as a base for novel functional materials), PhD Thesis, Instytut Fizyki Jądrowej Polskiej Akademii Nauk, 2011.
[43] J.-G. Zhu and C. Park, "Magnetic tunnel junctions Tunnel junctions and magnetic tunnel junctions," *Mater. Today*, 2006.
[44] S. Yuasa, T. Nagahama, A. Fukushima, Y. Suzuki, and K. Ando, "Giant room--temperature magnetoresistance in single-crystal Fe/MgO/Fe magnetic tunnel junctions," *Nat. Mater.*, 2004.
[45] W. Wang *et al.*, "Coherent tunnelling and giant tunnelling magnetoresistance in Co2 FeAl/MgO/CoFe magnetic tunnelling junctions," *Phys. Rev. B - Condens. Matter Mater. Phys.*, 2010.
[46] A13ean, "A simplified explanation of spin-transfer torque using the Stoner model of ferromagnetism," 2011. [Online]. Available: https://commons.wikimedia.org/wiki/File:Spin_Transfer_Torque_with_Stoner_model.svg (access: 1/03/2023).
[47] US Department of Energy. [Online]. Available: http://www.nano.gov/html/facts/nanoscale.html (access: 1/03/2020)
[48] M. Krupinski, R. Bali, D. Mitin, P. Sobieszczyk, J. Gregor-Pawlowski, A. Zarzycki, R. Böttger, M. Albrecht, K. Potzger and M. Marszałek, "Ion induced ferromagnetism combined with self-assembly for large area magnetic modulation of thin films," *Nanoscale* 11, 8930, 2019.
[49] M. Krupinski, D. Mitin, A. Zarzycki, A. Szkudlarek, M. Giersig, M. Albrecht and M. Marszałek, "Magnetic transition from dot to antidot regime in large area Co/Pd nanopatterned arrays with perpendicular magnetization," *Nanotechnology* 28, 085302, 2017.

[50] M. Krupinski, M. Perzanowski, A. Zarzycki, Y. Zabila and M. Marszałek, "Ordered FePdCu nanoisland arrays made by templated solid-state dewetting," *Nanotechnology* 26, 425301, 2015.
[51] M. Krupinski, M. Perzanowski, A. Maximenko, Y. Zabila and M. Marszałek, "Fabrication of flexible highly ordered porous alumina templates by combined nanosphere lithography and anodization," *Nanotechnology* 28, 194003, 2017.
[52] [M.C. Desjonqueres, D. Spanjaard: *Concepts in Surface Physics*, Springer-Verlag, Berlin 1993.
[53] D. Apalkov, B. Dieny, J. M. Slaughter, „Magnetoresistive Random Access Memory," Proceedings of the IEEE, 2016, 104, pp. 1796-1830.
[54] S. Kaya, "On the magnetisation of single crystals of cobalt," *Sci. Rep. Tohoku Imp. Univ*. 17, 1157, 1928.

eISBN 978-83-67188-44-9

Cracow University
of Technology